SHAPE AND TOPOLOGY OPTIMIZATION FOR ELECTRO-MECHANICAL ENERGY CONVERTERS

Erin Kuci

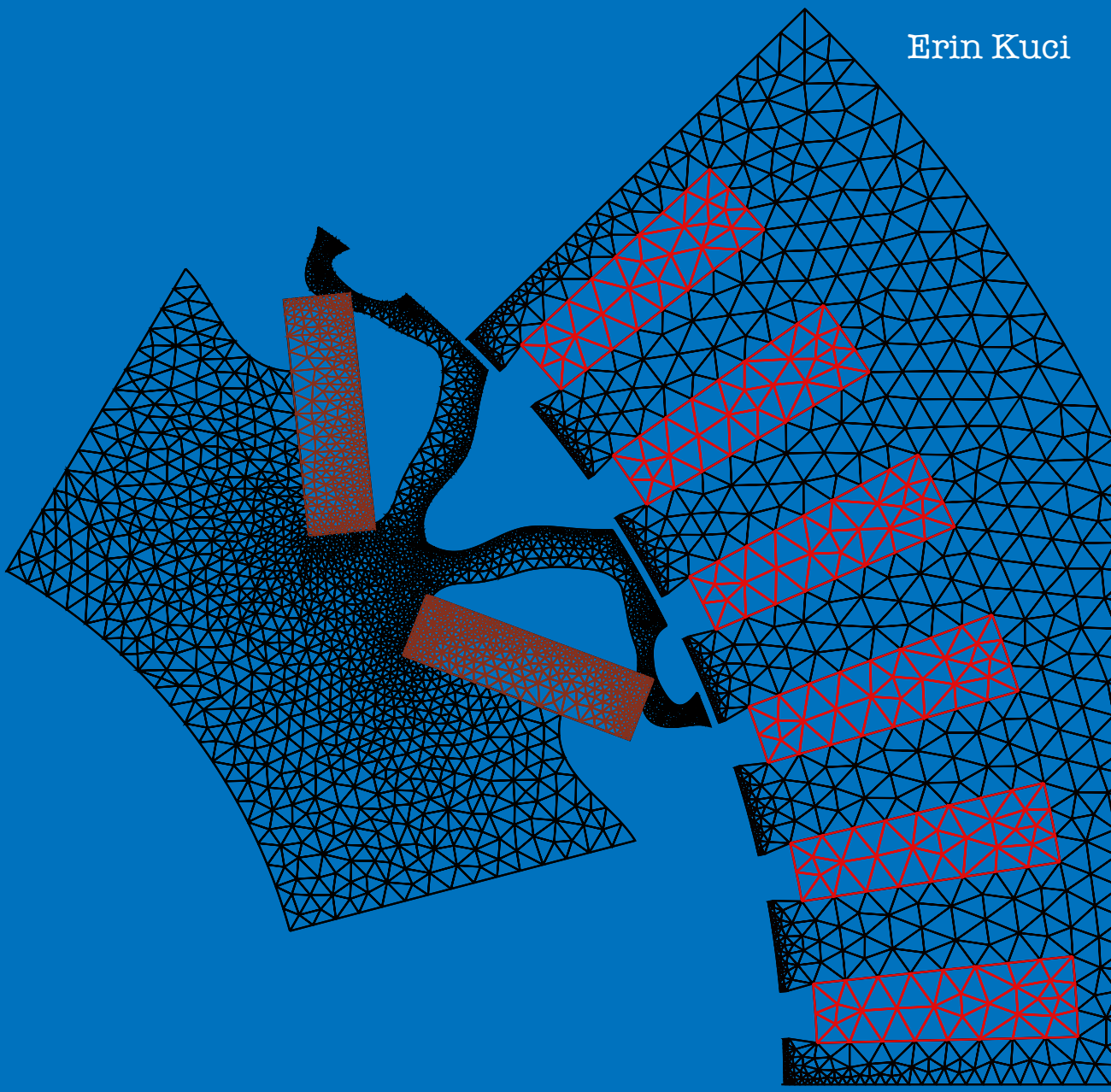

Doctoral thesis
University of Liège, Liège, Belgium, 2018

Shape and Topology Optimization for electro-mechanical energy converters

Shape and Topology Optimization for electro-mechanical energy converters

Doctoral Dissertation presented by

Erin Kuci

in partial fulfillment of the requirements for the degree of
Doctor of Philosophy in Engineering Sciences

Aerospace and Mechanical Engineering Department
University of Liège, Liège, Belgium

February 2018

Thesis committee:

Prof. Olivier Bruls (Committee president)	University of Liège, Belgium
Prof. Pierre Duysinx (Advisor)	University of Liège, Belgium
Prof. Christophe Geuzaine (Co-advisor)	University of Liège, Belgium
Prof. Michael Bruyneel	University of Liège, Belgium Scientific director, GDTech SA
Prof. Bruno Dehez	UC Louvain, Belgium
Prof. Johan Gyselinck	UL Bruxelles, Belgium
Prof. Guillaume Parent	Université d'Artois, France
Prof. Krister Svanberg	Royal Institute of Technology, Sweden
Prof. Martin Philip Bendsoe	Danish Technical University, Denmark

Author contact information:

Erin Kuci
Automotive Engineering Research Group
Aerospace and Mechanical Engineering Department
University of Liège

Quartier Polytech 1,
Avenue de la Découverte, 13A, B52,
4000 Liège, Belgium

Email: Erin.Kuci@uliege.be
Phone: +32 4 3664638

Funding:

This work was supported in part by the Walloon Region of Belgium under grant RW-1217703 (WBGreen FEDO), the Belgian Science Policy under grant IAP P7/02 and grant PIT7508 (ATAC-HP).

Abstract

The sustained growth of the industrial sector requires high-efficiency electro-mechanical energy converters, in particular electrical rotating machines, at the lowest possible cost. The use of modern power electronics converters at all levels of electrical power applications, involves, on the other hand, switching components with very low switching times and always increasing current levels. Passive components in these devices (busbars, inductors, transformers) must be designed to be compact without compromising their performance (e.g. power losses, electromagnetic interference/compatibility). Automated design optimization methods, in particular shape and topology optimization, used so far mostly in the field of structural engineering, offer a major step evolution in the design of such electro-mechanical and electric energy converters. The objective of this thesis is to provide engineers and practitioners of the field with appropriate methods which allow to carry out such design tasks by numerical optimization in an efficient way, and to extend the design capabilities to electro-mechanical converters.

This thesis exploits a computer aided design (CAD) representation of industrial systems and the finite element method (FEM) to solve the partial differential equations (PDEs) that govern their behavior under certain physical conditions. This thesis addresses three main subjects. First, the sensitivity analysis of electromagnetic PDEs solution is revisited in view of being used with gradient-based methods. Classical scalar formulations are extended to a general rigorous framework, and expressed analytically prior to discretization, to treat the vector case. Secondly, an iterative solver is designed so as to solve efficiently the large-scale linear systems arising from the design problem. Third, the design improvement capabilities are extended by developing an integrated and unified formalism for simultaneous shape and topology optimization of a system.

Résumé

La croissance soutenue du secteur industriel exige des convertisseurs d'énergie électromécaniques à haut rendement, en particulier des machines électriques tournantes, au coût le plus bas possible. L'utilisation de convertisseurs d'électronique de puissance modernes à tous les niveaux d'applications de conversion de puissance électrique implique d'autre part des composants de commutation avec des temps de commutation très courts et des niveaux de courant toujours plus élevés. Les composants passifs de ces dispositifs (busbars, bobines, transformateurs) doivent être conçus pour être compacts sans compromettre leurs performances (telles que les pertes de puissance, interférences/compatibilité électromagnétiques). Les méthodes automatisées de conception optimale, en particulier l'optimisation de forme et l'optimisation de la topologie, utilisées jusqu'à présent principalement dans le domaine de l'ingénierie structurelle, offrent une évolution majeure dans la conception de tels convertisseurs d'énergie électromécanique et électrique. L'objectif de cette thèse est de fournir aux ingénieurs et aux praticiens du domaine des méthodes appropriées qui permettent d'effectuer de telles tâches de conception par optimisation numérique de manière efficace, et d'étendre les capacités de conception aux convertisseurs électromécaniques.

Cette thèse exploite une représentation assistée par ordinateur (CAO) de systèmes industriels et la méthode des éléments finis (FEM) pour résoudre les équations aux dérivées partielles (EDP) qui régissent leur comportement dans certaines conditions physiques. Cette thèse aborde trois sujets principaux. Dans un premier temps, l'analyse de sensibilité de la solution d'EDP électromagnétique est revue de manière à être utilisée avec des méthodes basées sur le gradient. Les formulations scalaires classiques sont étendues à un cadre général rigoureux, et exprimées analytiquement avant la discrétisation, pour traiter le cas vectoriel. Deuxièmement, un solveur itératif est conçu de manière à résoudre efficacement les systèmes linéaires de grande taille résultant du problème de conception. Troisièmement, les capacités de la conception sont étendues en développant un formalisme intégré et unifié pour l'optimisation simultanée de la forme et de la topologie d'un système.

Acknowledgements

First of all, I wish to thank both Professor P. Duysinx and Professor C. Geuzaine for the opportunity they gave me to do research in excellent conditions and with great freedom in the Department of Aerospace and Mechanical Engineering as well as in the Department of Electrical Engineering of the University of Liège. I am very grateful to you for introducing me to the world of scientific research, each with your personal approach, and for your guidance, your support as well as your advice.

I thank Professors O. Bruls, M. Bruyneel, B. Dehez, J. Gyselinck, G. Parent, K. Svanberg and M.P. Bendsøe for their participation in the examination committee and for the review of this manuscript.

In addition I want to warmly thank all the present and former colleagues of both the Department of Aerospace and Mechanical Engineering as well as the Department of Electrical Engineering I worked with for the last four years for their valuable friendship and for excellent working atmosphere. In particular, I want to thank Patrick Dular as well as François Henrotte for their help at any time. I learned so much from your experience and your advice. In the same way, I also sincerely thank professor Krister Svanberg for welcoming me to KTH and for the fruitful discussions that were the starting point of my research.

I gratefully acknowledge the Walloon Region of Belgium under grant RW-1217703 (WBGreen FEDO), the Belgian Science Policy under grant IAP P7/02 and grant PIT7508 (ATAC-HP) which all supported parts of the thesis.

Finally, I want to thank my sister and parents who shared my daily life during the realization of this thesis and who are the most affective and enriching family one could hope for.

Erin Kuci,
April 2018.

Overview

Industrial design issues can in general be formulated mathematically as optimization problems aiming at achieving specific performance criteria while handling a number of technical design constraints within predefined limits. Therefore, automated design optimization methods have been developed since the early 1970's mainly in the field of structural engineering. They provide engineers with adapted procedures in which computers greatly help in the search for the optimal design of systems.

With the development of computers, numerical models have expanded along the years in a quasi exponential fashion. In particular, the one and two-dimensional models of the first ages of CAD have now been massively replaced by three-dimensional models which offer a much better representation of reality in many cases. Numerical models of industrial devices nowadays may have typically several millions of discretized state variables and a computation time of several hours or even days. Optimization based on such models requires solving them repeatedly (several tens or hundreds of times), which is not practicable at this time. Two paths must therefore be followed to make optimization available to industrial design: (1) direct models can be made faster; (2) the number of model evaluations needed by optimization algorithms can be reduced. Both paths correspond to very active research fields in engineering and applied mathematics. This work focuses on the latter and is organized along a number of complementary axes:

1. We focus on two particular optimization problems: shape optimization and topology optimization. The former uses selected geometrical parameters of the CAD description as optimization design variables, whereas with the latter, the design variables, which are called densities, represent the presence or absence of material at each point of the region where it is applied. However, there is nowadays an increasing interest in combining both methods, so as to determine the CAD configuration while optimizing, at the same time, the material usage of the system. We have therefore developed a tool which

handles appropriately the two representations, and allows hence to carry out an optimization in an extended design space involving shape and topology design variables.

2. The physical behavior of the optimized system is governed by a PDE model, possibly nonlinear, discretized by means of, e.g., the finite element method (FEM). The performance functions of the optimization problem are therefore a function of the physical problem solution and their evaluation is hence time consuming since it requires solving repeatedly the PDEs for a sequence of geometries of the system. The solution of such complex optimization problems is obtained with methods developed in the field of nonlinear mathematical programming since the early 1960's. In structural optimization the state-of-the-art solvers are the so called sequential convex programming approach with the two famous methods: the method of moving asymptotes (MMA) by Svanberg [1987] and the convex linearization (CONLIN) method by Fleury [1989]. Industrial design issues are formulated however as optimization problems which involve, in realistic cases, a high dimensional design space with often a number of constraints of same order of magnitude as the number of design variables. The computational effort involved in solving such problems becomes comparable to the effort involved in solving the PDEs, hence making the method prohibitively expensive for handling the largest industrial design problems. This work aims at revisiting the classical solvers so as to obtain the optimal solution in an affordable time.

3. In the context of the gradient-based optimization method, the concept of sensitivity is pivotal and must account for the implicit variation of performance functions, as well as the solution of the PDEs with respect to the design variables. However, its calculation can be time consuming, especially if a naive approach based on finite differences is implemented, since it requires solving the time-consuming and possibly nonlinear PDEs anew for each slightly modified geometry as the design variables are perturbed. Much effort has been devoted over the years to the derivation of efficient methods for sensitivity calculation, mostly in the area of structural mechanics, which take benefit, in their most successful approaches, from the structure of the optimization problem. The calculation of sensitivity becomes however rather complex for other disciplines, such as electromagnetic applications, which involve an unknown vector field. We have therefore developed systematic tools to handle the unknown vector field, and recover, in addition, the previously obtained sensitivity by other authors as particular cases. We have also extended the sensitivity calculation of problems with time-harmonic PDEs.

We have integrated the corresponding gradient-based automated optimization tool to the open-source software GetDP (Dular et al. [1998]), and Gmsh (Geuzaine and Remacle [2009]) through the ONELAB interface which can be downloaded from the following website: `http://onelab.info`. The proposed framework allows for an optimization in an extended shape and topology design space, with

an efficient gradient-based optimization algorithm. The tool has been devoted to successfully determine the geometry of electro-mechanical energy converters of great industrial relevance: electrical rotating machines, Fig. O1, and multiplanar busbars, Fig. O2, so as to minimize the torque ripple of the former while ensuring the mechanical resistance of the rotor submitted to centrifugal forces, and to minimize the mismatch of impedances which occurs in the latter.

Figure O1: *Top: A prototype of a fractional 12-slot and permanent-magnet (PM) assisted synchronous reluctance machine is considered, left, as well as its rotor, right, with laminations in which are inserted the PMs. This type of machine exhibits high torque ripple(Pictures from Boglietti et al. [2014]) Bottom: Several pragmatic approaches have been implemented to reduce cogging torque, right, as well as the torque ripple, left, by means of laminations with small PMs added so as to saturate the steel bridge and to increase the power factor of the considered electrical machine are considered. However these designs lead in general to a decrease of the average torque and do not take into account the strength of the structure. Both aspects can be combined in an automated design. (Pictures from Bianchi et al. [2009], left, and Bianchi and Bolognani [2002], right.)*

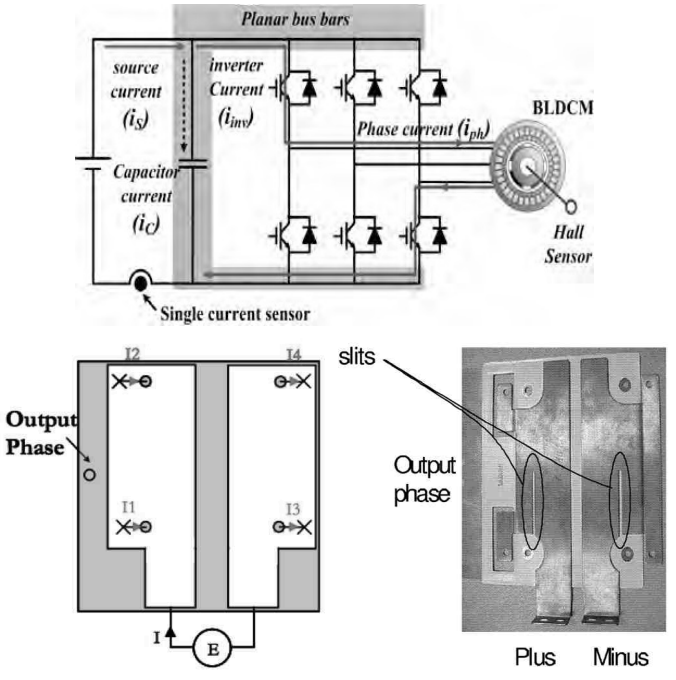

Figure O2: *A classical connection of a power converter with an electrical motor, left, is considered. The power converter involves switching components, e.g. IGBT and a multi-layer busbar, right, to replace the cable wiring. The design of the busbar can greatly benefit from automated design techniques so as to determine a geometry of the plates that exhibits a low stray inductance, e.g. by widening conductive sections, in a shape optimization approach, or alternatively by filling at most a given volume fraction of the available domain, in a topology optimization approach, e.g. for minimizing the mismatch of currents that goes through the power switches. (Pictures from Guichon et al. [2006])*

Outline

The manuscript is organized as follows. In Chapter 1, we review state-of-the-art techniques for the subjects that are the foundation of our research: (1) shape, topology and combined shape and topology optimizations; (2) the sensitivity analysis of performance functions in the context of such constrained optimization problems which involve PDEs; and (3) the numerical techniques used to solve the optimization problem. In Chapter 2, we detail our contributions. They have been the topics of several publications which are appended in their original published form at the end of the thesis:

1. A framework to express analytically sensitivity analysis of systems governed by PDEs with respect to design variables which control the shape of the systems, based on the Lie derivative (Appendix A);

2. A suitably preconditioned iterative solver to handle the large-scale problems which involve at least as many design variables as constraints (Appendix C)

3. A strategy to perform simultaneous shape and density based topology optimization following the previously developed sensitivity as well as an adequate mapping for handling the complex interactions between the material distribution of topology and the geometry modifications of shape optimization (Appendix D);

4. The extension of the Lie derivative in the time-harmonic domain in order to tackle more involved applications, such as eddy-current problems (Appendix B).

In Chapter 3, we provide numerical applications representative of industrial practice. The first showcase deals with the simultaneous shape and topology optimization of the rotor layout of an interior permanent-magnet machine in order to smooth the torque profile with respect to the angular positions of the rotor, while ensuring its mechanical strength. The second showcase considers the optimal design of a three dimensional multiplanar busbar so as to minimize the impedance mismatch. Finally, conclusions as well as our perspectives are presented in the last Chapter.

Contents

Chapter

1 State-of-the-Art

1.1. Shape optimization

Shape optimization has been an active research area that one often traces back to the seminal work of Zienkiewicz and Campbell [1973]. In early works of shape optimization, as summarized in Bletzinger et al. [2010], the design variables were selected among the nodal coordinates of the finite element mesh. However, the quality of the mesh of the structure undergoing shape optimization was deteriorated throughout the optimization process, resulting in a dramatic loss of accuracy of the numerical method, as reported in Haftka and Grandhi [1986], see Fig 1.1.

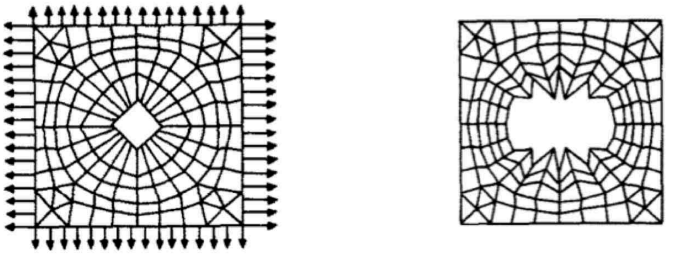

Figure 1.1: *The structural shape optimization of a plate with a hole is considered. The design variables are set as the nodal coordinates of the finite element mesh in order to maximize the maximum Von-Mises stress which appears in the vicinity of the hole. Their variation brings distortion throughout the successive boundary updates. (Pictures from Haftka and Grandhi [1986])*

As summarized in Olhoff et al. [1991], an efficient representation of shape optimization avoids the one-to-one dependence between the design variables and the finite element mesh by using a CAD model description of the geometry. Polynomial or rational representations of the boundaries have been used early on, e.g.

Bezier or B-spline in Braibant and Fleury [1984], or NURBS in Beckers [1991]. The design variables were selected among the geometrical parameters of the model such as the control points that govern the shape of the geometric entities of the structural boundaries. This approach naturally provided a consistency between the design and CAD models, see Fig. 1.2.

The latter parameterization has been followed in the context of the optimization of electrical rotating machines, in which design variables are set classically as the thickness of permanent magnets (PMs) of a permanent-magnet synchronous machine (PMSM), their position, the slot opening, the width of rotor yoke, the angle of one pole magnet, see for instance Kim et al. [2008], or Kioumarsi et al. [2006]. Shape optimization has also been successfully applied to determine either the stator shoes that minimize cogging torque, e.g. Choi et al. [2011], or the rotor pole designs in interior permanent-magnet (IPM) motors to obtain a sinusoidal flux density distribution in the air-gap, as in Choi et al. [2012]. In this context, a multi-phase level-set model represents the various material properties of the objects in the rotor, e.g. Lim et al. [2012]. A classical level set based shape optimization that determines the radial component of the air gap flux density waveform has also been used, as in De La Ree and Boules [1992], Borghi et al. [1999] and more recently by Dajaku and Gerling [2012], or Oh et al. [2013].

The geometry of a multi-layer busbar has also been determined by a shape optimization, generally coupled with a circuit-based model of the busbar. The method aims at minimizing the inductance of the busbar by reducing the commutation loop size, e.g. by rearranging the layers disposition as in Buschendorf et al. [2013], Chen et al. [2012] or Chen et al. [2014], widening conductive sections as in Wen and Xiao [2012], or Khan et al. [2014], using symmetrical busbars, as in Burtovoy and Galkin [2012], or Caponet et al. [2002], and the output current can be balanced, as in Pasterczyk et al. [2005].

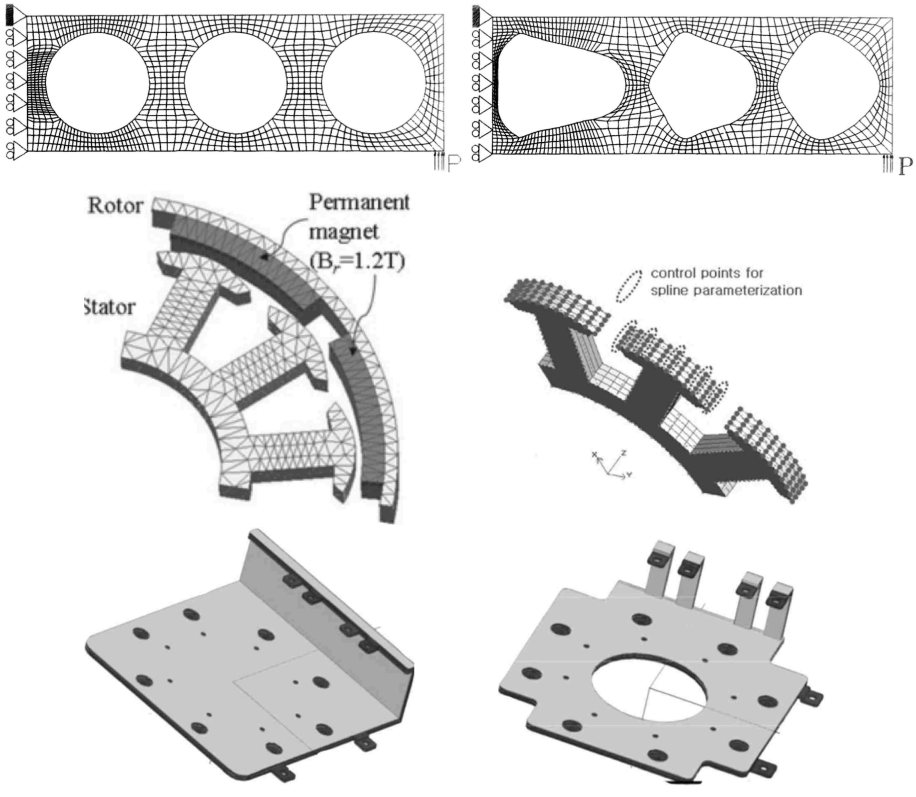

Figure 1.2: *Top: The structural shape optimization of support beam which carries the floor in the fuselage of a civil aircraft is considered. The design variables are set as the control points of the splines that represent the holes, and determined so as to minimize the volume of the structure under a prescribed maximum deflection and maximum Von-Mises stress. (Pictures from Olhoff et al. [1991]) Middle: A synchronous permanent-magnet electric machine is considered. The design variables are selected as the control points of splines are determined so as to make the induction field in the airgap sinusoidal. (Pictures from Kim et al. [2007a]). Bottom: A multi-layer busbar is considered. A circular hole is introduced in the CAD and its radius is determined so as to minimize the inductance of the busbar. (Pictures from Khan et al. [2014])*

Shape optimization often implies drastic changes of the structural geometry as the design variables change and one requires hence mesh adaptations so as to maintain a certain level of FEM solution accuracy, which in turn affects the convergence of the optimization algorithm. As reported in Zhang et al. [1995], the mesh topology is slightly modified as an a-priori refinement indicator is validated. In the early days, when automatic mesh generators were not available, a Laplacian smoothing was classically used to determine the location of inner nodes from one optimization iteration to the next. In a more general setting, shape modifications are reflected by means of a velocity field, for which various automatic generation methods have been proposed in the literature, using either a geometrical constructive approach such as the isoparametric mapping by Botkin [1982], Imam [1982], Braibant and Fleury [1984], Yang and Botkin [1987], or an auxiliary structure, such as the boundary displacement method by Choi [1987], Choi and Yao [1987], Yao and Choi [1989] or the fictitious load method by Belegundu and Rajan [1988], or Zhang and Belegundu [1992], or more recently a method based on NURBS with distortion control by Silva and Bittencourt [2007].

Alternatively, some researches have tried to formulate shape optimization by introducing different numerical methods and parameterizations so as to circumvent the technical difficulties linked to the variation of the spatial discretization. Approaches based on a fixed mesh, such as the fictitious domain method of Daňková and Haslinger [1996] or the projection methods by Norato et al. [2004] and more recently the Eulerian shape optimization of Kim and Chang [2005] are among successful approaches. Non-conventional mesh-free methods have also been applied to shape optimization in 2D and 3D geometries, e.g. Kim et al. [2002], and a T-Spline finite element method by Ha et al. [2010] is based on the isogeometric analysis developed by Hughes et al. [2005].

1.2. Topology optimization

Topology optimization was first successfully solved in structural mechanics in the late 1980's by Bendsøe and Kikuchi [1988] who proposed to formulate the problem as the presence or not of a specific anisotropic porous material at each point of the region where it is applied. The method was therefore able to introduce, or remove, holes and blocks of material, changing the shape topology and exploring new, and oftentimes unexpected, possibilities to the design of the systems under consideration. The material properties of the early approach resulted from homogenization theory. The Simplified Isotropic Material with Penalization (SIMP) model was proposed later on by Bendsøe [1989] in order to overcome some of the weak points of the design method based on homogenization. Instead of considering each element of a discretized design space as a region of material composed by a microstructure, the SIMP approach considers the design variables as a *density* field, defined on the fixed region. The computation mesh is hence kept constant throughout the optimization and identical to the finite element discretization of the design domain for both state variables and the density field, thus avoiding any mesh distortion and/or the use of mesh adaptation techniques.

While the development of topology optimization is outstanding in the field of structural engineering, which has historically pioneered its development, with many industrial applications, as summarized in Rozvany [2001], Eschenauer and Olhoff [2001] or Sigmund and Maute [2013], it is also sensible in the field of electromagnetic design. As discussed in Bendsøe and Sigmund [1999], many interpolation schemes relating the density design variables to the material properties have been proposed for structural density based methods. The electromagnetic domain received at first attention from Dyck and Lowther [1996], and the saturation of ferromagnetic materials were also taken into account in Dyck and Lowther [1997]. The authors present a *geometric mapping* between the steel proportion and the magnetic permeability.

The SIMP based topology optimization, in particular, has been successfully applied to the design of electrical machines, e.g. by Wang et al. [2004], Choi et al. [2011], Im et al. [2003], or Lee and Wang [2012], while the general homogenization approach seems to have been almost exclusive to Yoo et al. [2001]. The design of busbars, e.g. including the temperature effects, has been investigated by Puigdellivol et al. [2017], while the interactions with fluids is studied by Iga et al. [2009] or Matsumori et al. [2013] and the electromagnetic behavior by Puigdellivol et al. [2016], see Fig. 1.3. More focused applications have also been treated in a number of studies: the design of piezoelectric transducers by Silva et al. [1997], perpendicular magnetic recording head by Okamoto et al. [2005], dielectric waveguide filters by Byun and Park [2007], ultrasonic wave transducers by Kim et al. [2007b], micro fluid mixers by Aage et al. [2008], acoustic devices by Dühring et al. [2008], photonic bandgap fibers by Dühring et al. [2010] and photonic crystals by Borel et al. [2005].

In any optimized system it is crucial to control the structural stress state so as to ensure the mechanical robustness of the optimized structure. However such problems are challenging from a computational point of view, since local criteria like stresses are in general considered in each finite element of the mesh, and hence lead to large-scale problems with possibly as many design constraints as finite elements in the mesh. The solution of such problems can therefore require a computational effort comparable to the effort spent on the solution of the physical problem itself. Furthermore, in the context of a density based topology optimization, the solution of the optimization problem with stress constraints comes to some degenerated subdomains, as discussed in Cheng and Jiang [1992]. These are hardly reached by mathematical programming algorithms based on KKT which are not applicable in that case. The latter problem is addressed as the singularity problem and can be alleviated by introducing a relaxation of the stress constraints, such as the ϵ-relaxation proposed by Cheng and Guo [1997].

The stress constraints have been included in the density based topology optimization problems mainly after the seminal work by Duysinx and Bendsøe [1998]. Based on the study of rank-2 microstructures, they suggested a macroscopic failure model for porous materials. The computational effort of the former approach has been reduced by Duysinx and Sigmund [1998] who proposed to account for

the local stress state by using an aggregated and integrated constraint approximating the maximum stress through the p-norm or p-mean for instance. An effective algorithm has also been proposed by Le et al. [2010] to handle the stress constraints. An alternative technique to the ϵ-relaxation, the qp-relaxation, has also been proposed by Bruggi [2008].

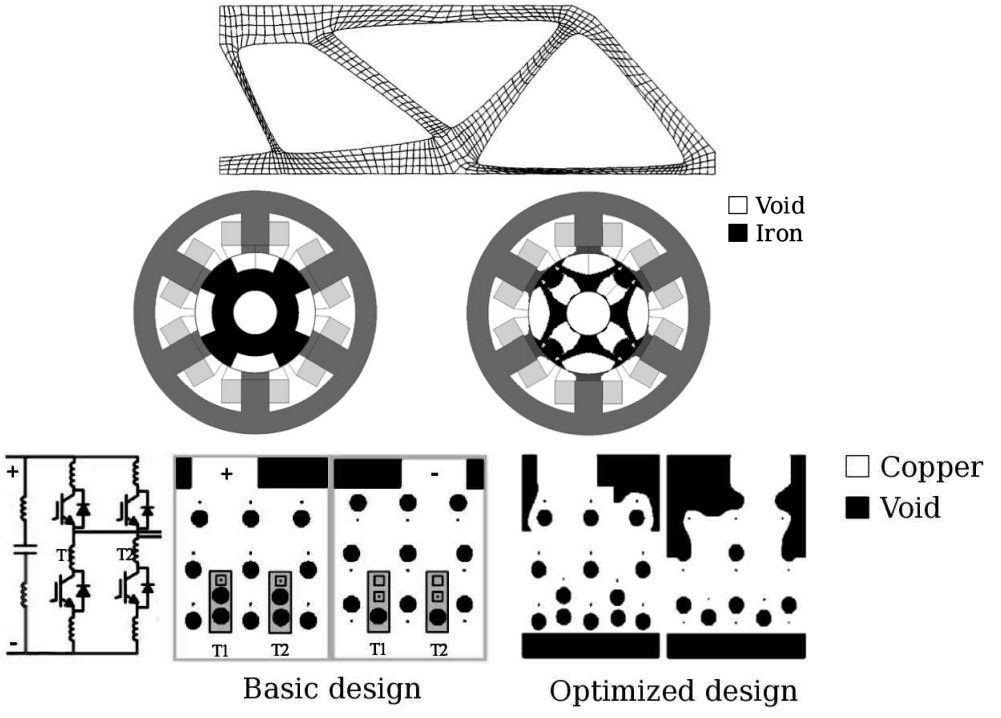

Figure 1.3: *Top: The support beam presented in Fig. 1.2 is redesigned so as to maximize the stiffness of the beam while filling at most a given volume fraction of the available domain. The optimal design is determined without requiring any a-priori guess. Middle: The design of the rotor of a switched reluctance machine (SRM), initially completely filled with steel, left, is determined by a density based topology optimization to lower the torque ripples of the machine. The resulting design, right, results in a lighter rotor and exhibits a low torque ripple. (Pictures from Lee et al. [2010]). Bottom: A busbar, i.e. a thick strip of copper which interconnects the power switching devices, T1 and T2 to other electronic components, is considered. The copper distribution is determined in both plates so as to minimize the overall inductance. (Pictures from Puigdellivol et al. [2016]).*

1.3. Sensitivity analysis of problems governed by PDEs

Both shape and topology optimization approaches can be formulated mathematically as an optimization problem which aims at determining a set of design variables. These describe the geometry using either existing boundaries or alternatively a material distribution. The problem minimizes a cost function, subjected to inequalities, ensuring the manufacturability or the feasibility of the design. The PDEs that govern the physical behavior of the system are included as constraints in a standard statement of the optimization problem. For a given geometrical configuration (i.e. design variables), their solution is obtained in general by means of FEM discretization. This is used to evaluate the performance functions. There is therefore an implicit and nonlinear dependence of both the performance functions and the solution of the PDEs in the design variables. Furthermore, the repetition of these evaluations for successive configurations of the design variables is, in general, expensive from a computational point of view, especially for large-scale applications.

The sensitivity of the optimization problem, i.e. the derivative of each performance function with respect to each design variable, is therefore calculated so as to make use of gradient-based optimization algorithms. The solution to the design optimization problem is generally solved through a recursive approach in which a sequence of explicit subproblems are solved efficiently through tailored *mathematical programming* algorithms, such as dual or primal-dual solvers. This leads to fewer function evaluations, and hence, in our case, limits the required number of solutions of the finite element physical problem. The main difficulty in the calculation of sensitivity lies in the differentiation of the PDEs with respect to design variables which modify the boundaries of the system.

Two approaches have emerged over the years for the calculation of this sensitivity, called *shape sensitivity*. The first one acts as an analytical differentiation at the level of the variational formulation of the problem, as summarized in Arora and Haug [1979], whereas the second approach differentiates the discretized algebraic system, as in Adelman and Haftka [1986]. An approach that works at the software level and consists in direct differentiations of the computer code itself, as in Griewank et al. [1996], or Bischof et al. [1996], and more recently Farrell et al. [2013] may be attempted for explicit geometrical representation. However, they cannot be extended to systems described by a CAD model with spatial discretizations that are modified as the optimization unfolds.

In the continuous context, prior to discretization, the variation of the integral quantity, such as the residual related to the physics of the problem, with respect to a design variable that controls the material density distribution can be expressed explicitly, in general, by means of the total derivative, as suggested by e.g. Kyung K. Choi [2005]. However, the variation of the integral quantity with respect to a design variable that brings modifications in the boundaries of the system is more delicate to express, and requires extra terms to account for the implicit dependency of the integral quantity in the continuous flow of geometrical modification.

The shape sensitivity problem has been treated through the velocity method, as introduced in Sokolowski and Zolesio [1992], and more recently in Delfour and Zolésio [2011]. This approach uses the variation of the shape design variable as the parameter of a family of mappings describing a smooth geometrical transformation of the domain, with no tearing nor overlapping, that brings the boundaries of the domain from their unperturbed position to their perturbed position. The mapping with the scalar parameter taking values in a neighborhood of zero and playing the role of a pseudo time variable, determines therefore a flow on the Euclidian space characterized by a velocity field.

The velocity method has been applied successively to elasticity problems where the solution of the physical problem is a scalar field, e.g. Allaire et al. [2004], Dems and Mroz [1984], or Haug and Arora [1979]. Following this approach, analytical formulas have also been proposed in other disciplines such as electromagnetics, based on classical vector analysis, as in Biedinger and Lemoine [1997], Koh et al. [1993], or Park et al. [1993]. However, these works have been exclusively devoted to problems expressed in terms of a scalar unknown field, leaving aside the problem of handling the complex behavior of a vector field under the transformation that brings a modification of the system boundaries.

There exist several geometrical objects that have three components in an Euclidean space, but behaving differently under the one parameter family of mappings. We have to deal with circulation densities, (e.g. the magnetic vector potential or the magnetic field), and flux densities (e.g. the flux density and the current density). Although genuine vector fields, circulation densities and flux densities can be indiscriminately regarded as vector fields in an Euclidean space, their shape derivative are different under the geometrical transformation and they must therefore be carefully distinguished when evaluating the shape derivative of an expression involving such objets.

To handle the shape derivative of vector fields, one can refer to a more general theoretical framework based on the exterior calculus, e.g. as in Frankel [2011], well established so far in mathematical modeling and analysis of PDEs, e.g. Hermann et al. [1964], Henrotte [2004], borrowed from differential geometry, and in particular the concept of Lie derivative. These material derivatives have been used more recently by Hiptmair and Li [2013] in order to overcome the limitations and the tedious calculations of the vector analysis approach, classically used for the scalar field. Hiptmair and Li [2017] have applied this approach to the sensitivity calculation of a linear acoustic problem and also an electromagnetic scattering boundary integral equation.

Similarly to the physical problem, the sensitivity analysis can be time-consuming, since it involves, in conventional approaches, the solution of either one linear system obtained by differentiating the PDEs of the physical problem for each of the design variables (the so-called *direct approach*), or for each performance function (the *adjoint approach*). However, only the right-hand side of the additional linear systems needs be evaluated (the system matrix being already known) and

a substantial gain in computation time is obtained compared to a finite difference evaluation of sensitivity, which requires solving from scratch a second, possibly time-consuming, system for each design variable.

1.4. Gradient-based optimization methods

In this context, optimization algorithms relying on sensitivity of the optimization problem, often referred to as gradient-based algorithms, necessitate a small number of function evaluations, and hence, limit the required number of solutions of the physical problem compared to heuristic approaches, such as genetic algorithms. It should be noted that the latter have been used to estimate an optimized design in either shape or topology optimization problems, e.g. Balamurugan et al. [2008] or Wang et al. [2006], and also in Canyurt and Hajela [2007], without any information about the sensitivity of the problem. They can naturally handle discrete problems, and are therefore particularly well suited for topology optimization problems with design variables, allowed to be either 0 or 1. However, as reported in Rozvany [2009], the solution of the discrete problem quickly turns out to be intractable for large-scale problems. In particular, a large number of function evaluations, and hence a large number of PDE solutions are required to reach the solution.

Optimality criteria (OC) methods were proposed early on by Prager and Taylor [1968] to determine the optimal solution of the design problem. In this approach, the design space includes both the design variables and the Lagrange multipliers handling the constraints. Starting from the Karush-Kuhn-Tucker (KKT) optimality conditions, iterative update relations are derived for the variables. The optimality conditions are treated as additional constraints and are satisfied at the stationary point, as in NS Khot and Venkayya [1979]. This approach has been essentially applied for the solution of topology optimization problems based on a global design criterion, such as the compliance or maximization of fundamental eigenfrequencies, as in Olhoff [1970], Bendsøe and Kikuchi [1988], or Rozvany and Zhou [1991]. Their application to larger problems becomes numerically inefficient.

Among general nonlinear problems based on gradient methods, interior point (IP) methods together with sequential quadratic programming (SQP), e.g. Gill et al. [2015], are considered nowadays as the most powerful solvers, as it has been studied in Dolan and Moré [2002] or Benson et al. [2003]. They have been successfully applied to solve the design problem in Orozco and Ghattas [1997], Stolpe and Svanberg [2003], Dreyer et al. [2000] and Maar and Schulz [2000].

However, both interior point and SQP methods require the computation of the Hessian, which is time consuming for realistic industrial problems. In addition, they have difficulties to deal with nonlinear problems which are non-convex. Many different ways of handling the lack of convexity of the problems have been proposed, through the modification of the KKT system, in order to ensure the existence of a solution. Among them, the diagonal shift can be applied to the Ja-

cobian of the KKT system to make the resulting system positive definite. A more reliable technique consists in using a quasi-Newton method to approximate the Hessian of the system, as in Nocedal [1980]. Inertia controlling methods based on a modified LDL decomposition method have also been introduced, e.g. in Forsgren [2002].

Sequential approximation schemes combined with mathematical programming exploit gradient-based algorithms to reach the optimal solution of the design problem with multiple constrained problems. It has been shown by Schmit [1960] that it is better to approximate the original problem by a sequence of convex optimization subproblems. Their evaluation, and hence the evaluation of sensitivity and second order derivative, is then very efficient compared to the original model as they do not require any FEM solution.

The approximations have a large influence on the efficiency of the solution of the optimization problem. These are in general convex to have a unique solution for the subproblem and to ensure a conservative behavior so as to guarantee a steadily feasible and monotonous sequence of minimizers. Moreover, they are separable and lead to an advantageous solution through the dual maximization method. Various approximations relying on different intermediate linearization variables are available in the literature. Efficient optimization algorithms were proposed in combination with particular approximations: the Convex Linearization (CONLIN) algorithm by Fleury [1989], the Method of Moving Asymptotes (MMA) by Svanberg [1987], the Globally Convergent Method of Moving Asymptotes (GCMMA) by Svanberg [1995], Sequential Quadratic Programming (SQP) algorithms by Schittkowski [1986].

To solve the subproblems, Fleury [1993] proposed to use a dual formulation. Exploiting the Lagrange maximization, the primal constrained minimization problem, associated to a large number of variables, is replaced by a dual quasi-unconstrained maximization problem with a limited number of variables, the nonzero Lagrange multiplier associated to the active constraints.

Second-order methods such as SQP, or interior point methods, can advantageously be used to solve the approximation subproblem, without having to handle the issues that naturally arise from the lack of convexity for general nonlinear problems.

1.5. Combined shape and topology optimization

The design variables upon which density based topology optimization acts, which are called densities, represent the presence or absence of material at each point of the region where it is applied, whereas the design variables of a state-of-the-art shape optimization are the geometrical parameters of a CAD description. These densities are substantial quantities. This means that they are attached to matter while, on the other hand, shape optimization implies ongoing changes of the model geometry.

Although the implementation of the topology approach with a fixed spatial discretization is simple and numerically stable, it leads to layouts with jagged boundaries which have to be smoothed in an extra postprocessing procedure, as in Bletzinger and Maute [1997]. Moreover, in many practical design problems, the explicit representation of the boundaries of the system undergoing optimization is necessary to be able to model the problem with localized boundary effects. In all cases the explicit interface is necessary when interpreting the final design.

Several strategies intended to handle the complex interactions between shape and topology optimizations, have been developed so far, each with their own parameterizations, and also to overcome the shortcomings of standard density based topology optimization.

Among existing methods, adaptive topology optimization has been performed by Bletzinger and Maute [1997] to form an explicit interface between the solid and void regions which arise throughout a structural density based topology optimization, see Fig. 1.4. More recently, a similar paradigm has been followed by Christiansen et al. [2014], who has adapted to topology optimization, the deformable simplicial complex (DSC) method, introduced by Misztal et al. [2014] to simulate fluids accurately. Here, both the design and the analysis models rely on the same spatial discretization. The DSC deformation is therefore used to adapt the mesh after the movement of the interface, such that it is well formed, and involves a series of mesh operations, e.g. Laplacian smoothing, edge flip, vertex insertion and vertex removal, which are quite artificial.

In addition, topological derivatives, as in Eschenauer et al. [1994], are used to change the topology of the domain by creating new holes. The interface between void and solid regions is represented explicitly as one or more closed piecewise linear curves and is smoothed by determining the positions of the nodes belonging only to that interface, e.g. by means of a simple shape optimization with a prescribed maximum variations between the optimized and the current configurations.

Level Set methods, which were originally proposed by Osher and Sethian [1988] for numerically tracking free boundaries, are among alternative approaches to density based topology optimization. In this context, the geometry is represented as the zero Level Set of functions and are propagated through the solution of Hamilton-Jacobi type equations. This approach, which allows to easily handle large shape modifications without requiring a CAD representation, has been first applied to structural optimization by Allaire et al. [2002] and Wang et al. [2003], but also in electromagnetic design of electrical rotating machines, see Fig. 2.1. The review of various applications tackled by the level set method is provided in van Dijk et al. [2013]. The method can advantageously be carried out in a fixed mesh. Furthermore, the topological complexity of classical CAD based shape optimization is reduced since geometric entities, such as holes, can be merged or removed without degenerating the model, but unfortunately cannot be created, except if the method is combined with a topological derivative (see for instance Novotny

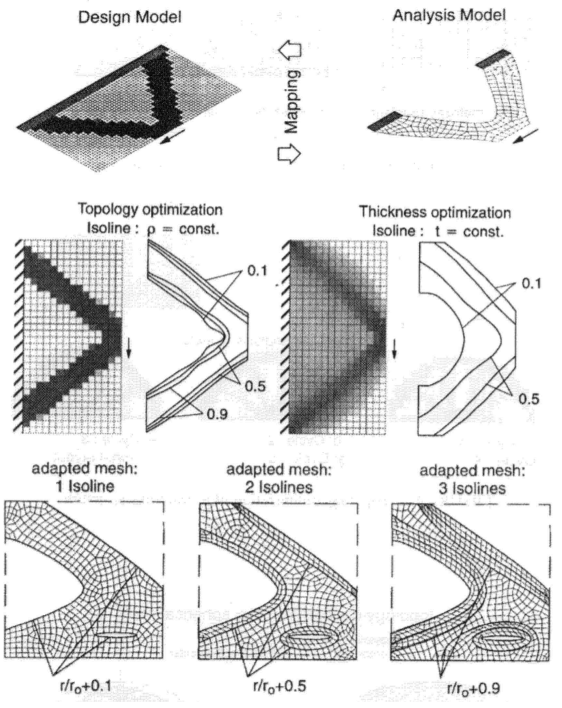

Figure 1.4: *An adaptive successive structural topology and thickness optimization of a cantilever beam is considered. Top: The analysis model uses the density distribution from the density model. The structure with boundaries defined by one (or even more) isolines between the void and solid regions of the density model are discretized with a finer mesh in the analysis model while a separate regular constant grid is used to discretize the density model. Middle: A simple sizing optimization is used to further smooth the thickness of the isolines, with a prescribed small variation between the optimized and the initial configurations. Bottom: The mesh of the analysis model is adapted in order to reduce the finite element error on the system response. (Pictures from Bletzinger and Maute [1997])*

et al. [2003]). The use of a Level Set representation of the geometry makes it difficult to take into account geometries with sharp angles (see for instance Kalameh et al. [2016] or Duboeuf and Béchet [2017]). It limits hence the range of systems that can be optimized.

The Level Set method is able to perform topology optimization if the number of holes of the initial design is sufficiently large and converges to configurations which strongly depend on the initial level sets distribution. It should be noted that using the level set method, a stress criterion can be integrated into the design of industrial systems. Stress constraints were treated in this context, allowing hence to get rid of the singularity problem involved when resorting to the density based

optimization, and therefore do not require any relaxation strategy. This problem has been analyzed, e.g. in Van Miegroet and Duysinx [2007], Allaire and Jouve [2008] and more recently James et al. [2012], who performed the minimization of the stress state in solid-void structures.

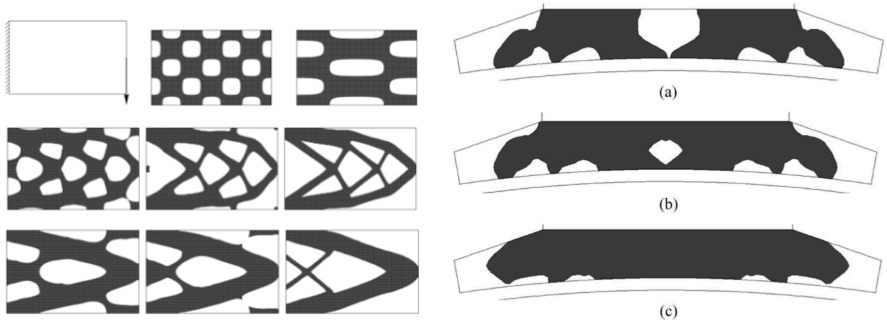

Figure 1.5: *Left: The structural topology optimization of a cantilever beam is carried out with a Level Set method so as to have an explicit description of the geometry. The optimization history, however, strongly depends on the initial number of Level Sets. (Figures from Allaire et al. [2002]) Right: The approach has also been applied to the electromagnetic design of e.g. the stator of an interior permanent-magnet rotating motor, so as to minimize the torque ripple. (Figures from Kwack et al. [2010]).*

Topology and shape optimizations have also been coupled in the context of packaging, see Fig. 1.6. The non-overlapping constraints between two different packaged items is a key issue and it has been expressed in the early work of Qian and Ananthasuresh [2004], as the distance between two circles approximating the components. However, the rough approximation of an item by a circle is not sufficient anymore when the item has a complex shape, especially concave. The Finite Circle Method (FCM) has been proposed by Zhang and Zhang [2009] to circumvent the limitations and it has been further used by Zhu et al. [2009]. In Zhu et al. [2009], the interactions between the movement of the components and the material density of the support have been synchronized through the combination of predefined density points in the support followed by a series of boolean mesh operations in order to maintain a mesh of good quality as optimization unfolds. However, the mesh manipulations are the center of the method while they should be just a mean to an end. Alternatively, Qian and Ananthasuresh [2004] used a material interpolation model which handles the movement as a physical variation of the material properties. The integration of this approach remains however quite cumbersome in industrial systems. In both approaches, a fixed mesh with predefined density points is used throughout the optimization. In Zhu et al. [2009], the distances between the element centroid and the density points controls the distribution of material density, and the method is made mesh independent by limiting the modification of the material density only inside predefined mesh patches.

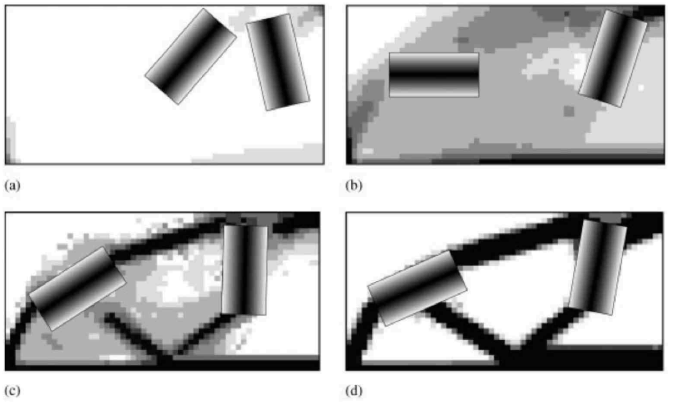

Figure 1.6: *The integrated layout approach aims at determining the optimal position of the rectangular shape components through the solution of a shape optimization while a density based topology optimization is carried out to optimize the material usage of the support. (Pictures from Zhu et al. [2009])*

Chapter

2 Personal contributions

Our contributions to advance the state-of-the-art overviewed in Chapter 1 deal with (1) the generalization of the calculation of shape sensitivities, to the nonlinear electro-mechanical case, in 2D and 3D, by means of an explicit Lie derivation of the variational formulations for both static and time-harmonic problems; (2) the adaptation of the interior point method for the solution of the large-scale convex approximations sequences obtained when solving the topology optimization problems with local restrictions; (3) the appropriate combination of the representation of a CAD-based shape optimization with a density based topology optimization to perform a joint shape-topology optimization. The corresponding algorithms are integrated to the open-source software GetDP (Dular et al. [1998]), and Gmsh (Geuzaine and Remacle [2009]) through the ONELAB interface which can be downloaded from the following website: `http://onelab.info`. The next three sections present a summary of our main contributions to these three areas.

2.1. General formulae for sensitivity in electro-mechanical problems

Our first contribution provides engineers with a general and a comprehensive theoretical framework to perform the shape optimization of systems governed by PDEs,

$$\begin{aligned} \min_{\boldsymbol{\tau}} \quad & f_0(\boldsymbol{\tau}, \boldsymbol{z}^\dagger) \\ s.t. \quad & f_j(\boldsymbol{\tau}, \boldsymbol{z}^\dagger) \leq 0,\ j = 1, \dots, m \\ & \tau_i^{min} \leq \tau_i \leq \tau_i^{max},\ i = 1, \dots, n \\ & r(\boldsymbol{\tau}, \boldsymbol{z}^\dagger, \boldsymbol{z}') = 0,\ \forall \boldsymbol{z}' \in Z_z^0, \end{aligned} \tag{2.1}$$

which aims at determining the design variable set $\boldsymbol{\tau}$, whose variation brings a geometrical modification of the optimized system boundaries. It is stated as the optimization of the objective function f_0 while ensuring some design constraints $f_j \leq 0$. The PDEs are here expressed in terms of a state variable $\boldsymbol{z}$ and the design

variable set $\boldsymbol{\tau}$. They are stated in a weak formulation, obtained by, e.g., a Galerkin linearization approach and they are written in a generic form through a residual $r(\boldsymbol{\tau}, \boldsymbol{z}^\dagger, \boldsymbol{z}')$, where $\boldsymbol{z}^\dagger$ is the physical solution.

Our contribution, in particular, extends the calculation of sensitivity, so far mostly derived for equilibrium equations arising in structural mechanics, to other disciplines such as electromagnetics. Thus, following the approach of Zolesio's velocity method, we express in a unified framework the sensitivity of any performance function (i.e. any function f_j of the solution of the PDE problem). One can further express the derivative of the state variables of the PDEs that involve either scalar or vector unknown fields. To this end we rely to the Lie derivative, i.e. the derivative of that performance function along the flow representing the continuous shape modification of the geometrical model induced by the variation of the considered design variable.

Contrary to previous work in the field, the purpose of our work is however, not to give a complete mathematical derivation of differential geometry concepts, but rather to provide engineers and practitioners in the field of optimization with a useful formula sheet, so as to derive formulas for new problems more easily. We introduce therefore a hybrid formalism which sticks with standard vector and tensor analysis notations, to express the sensitivity of the physical problem, with vector calculus like notations, in both a direct and an adjoint approach.

Following our formalism, we generalize equivalently in 2D and 3D the methods proposed so far in electromagnetics, e.g. in Park et al. [1993], that were limited to scalar unknown fields, i.e. to scalar potential 3D formulations or 2D electromagnetic problems. In addition, we offer the possibility to treat linear elasticity in this same context and recover the state-of-the-art results. We have validated all the analytical formulas derived in nonlinear magnetostatics and in linear elasticity with the finite difference approach and we conducted a deep investigation of the convergence of the computed sensitivity with mesh refinement using first and second order finite elements. The theoretical results pave the way towards real-life applications, typically industrial perspectives, such as eddy-current problems, and multi-physics problems.

Let us consider, for demonstration purposes, the magnetic vector potential $\boldsymbol{A}$ formulation of a magnetostatics problem excited by a current density $\boldsymbol{J}$ with a nonlinear material law $\boldsymbol{H}(\boldsymbol{B})$, on a bounded domain Ω, with boundaries controlled by a design variable τ. The problem is written in a variational form through a residual,

$$r(\tau, \boldsymbol{A}^\dagger, \boldsymbol{A}') \equiv \int_{\Omega(\tau)} \left(\boldsymbol{H}(\boldsymbol{B}^\dagger) \cdot \boldsymbol{B}' - \boldsymbol{J} \cdot \boldsymbol{A}' \right) \mathrm{d}\Omega = 0, \quad \forall \boldsymbol{A}' \in Z_A^0, \tag{2.2}$$

where $\boldsymbol{A}^\dagger$ is the solution of the nonlinear magnetostatic problem, $\boldsymbol{B}^\dagger = \mathbf{curl}\, \boldsymbol{A}^\dagger$ and $\boldsymbol{B}' = \mathbf{curl}\, \boldsymbol{A}'$.

In (2.2), there are several geometrical objects, that have three components in

an Euclidean space, but which behave differently under the geometrical transformation of the domain. Such objects are the circulation densities (also called 1-forms), e.g. $\boldsymbol{A}$ or $\boldsymbol{H}$. These quantities make sense when integrated over a curve. Flux densities (2-forms), e.g. $\boldsymbol{B}$ or $\boldsymbol{J}$, are quantities that make sense when integrated over a surface. Furthermore, a material law like $\boldsymbol{H}(\boldsymbol{B})$ converts a field quantity, $\boldsymbol{B}$, into another field quantity, $\boldsymbol{H}$, and contains therefore a geometrical conversion operator, called Hodge operator, that depends on the metric which has a non-vanishing Lie derivative when the system deforms. The implicit Hodge operator must be accounted for when evaluating the Lie derivative of a material law. Although genuine vector fields, classically adopted in state-of-the-art methods of sensitivity calculation, these objects are indiscriminately regarded as vector fields in an Euclidean space. So their Lie derivatives are different under the geometrical transformation of the domain and they must therefore be carefully distinguished when evaluating the Lie derivative of an expression involving such objets.

It follows from above that the derivative of the residual at equilibrium, with respect to the design variable τ, is obtained by applying the Lie derivative, and yields the linear system to be solved to obtain the Lie derivative of $\boldsymbol{A}^\dagger$ along the velocity field $\mathbf{v}$, i.e. $L_{\mathbf{v}}\boldsymbol{A}^\dagger$. It comes

$$\int_{\Omega(\tau)} \nu^\partial \, \mathbf{curl}\, L_{\mathbf{v}}\boldsymbol{A}^\dagger \cdot \mathbf{curl}\, \boldsymbol{A}' \, \mathrm{d}\Omega + \Big[\int_{\Omega(\tau)} \Big(\nu^\partial \big((\nabla \mathbf{v})^T \boldsymbol{B}^\dagger - \boldsymbol{B}^\dagger \operatorname{div} \mathbf{v} \big) \cdot \boldsymbol{B}' \quad (2.3)$$
$$+ (\nabla \mathbf{v})\, \nu \boldsymbol{B}^\dagger \cdot \boldsymbol{B}' - (\boldsymbol{J} \operatorname{div} \mathbf{v} - (\nabla \mathbf{v})^T \boldsymbol{J}) \cdot \boldsymbol{A}' \Big) \, \mathrm{d}\Omega \Big] = 0, \quad \forall \boldsymbol{A}' \in Z_A^0.$$

The obtained formula has a rather large number of terms, which can however be reused from the finite element solution. The first term in (2.3) involves the tangent stiffness matrix, ν^∂, which is already known from the computation of $\boldsymbol{A}^\dagger$. The bracketed terms, on the other hand, make up the partial derivative term that accounts for the explicit dependency (i.e. holding the field argument, $\boldsymbol{A}^\dagger$, constant) of the residual on the variation of τ.

The velocity field, $\mathbf{v}$, that represents the shape modification, must be determined for the computation of $L_{\mathbf{v}}\boldsymbol{A}^\dagger$ in (2.3). We have therefore proposed a practical and efficient method for the numerical generation of the velocity field based on the parametrization of the geometric model of the domain, and integrated into a finite element code, see Geuzaine and Remacle [2009] and Dular et al. [1999]. On a practical level, our approach makes use of the freedom in the definition of the velocity field to derive a method to limit the support of the volume integrals, as in (2.3), to a one layer thick layer of finite elements on both sides of the surfaces involved in the shape variation.

We start with a mesh of the initial CAD model for which each boundary node is represented by its parametric coordinates on the underlying curves or surfaces. After (small) perturbation of the CAD model, assuming that the perturbation of the parametric representation of the boundaries is also small, we relocate the initial mesh on the new CAD representation by freezing the node parameters. This

approach is very efficient when the mesh generation algorithms are based on the parametric representation of CAD entities, as is the case for Gmsh Geuzaine and Remacle [2009].

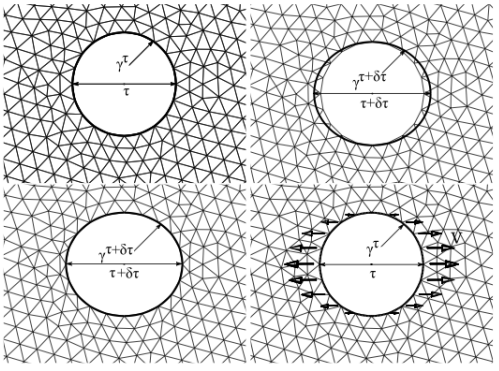

Figure 2.1: *A plate with an elliptic hole γ^τ is considered. The design variable τ is the major axis of the ellipse. After a finite perturbation $\delta\tau$, the mesh nodes lying on the surface γ^τ are relocalized on $\gamma^{\tau+\delta\tau}$ thanks to the CAD parametrization of the ellipse. The velocity field is approximated by finite difference of the node positions before and after the perturbation. (Figures from Kuci et al. [2017]).*

This first contribution has been published in *Computer Methods in Applied Mechanics and Engineering*, Kuci et al. [2017], and is reproduced in Appendix A. The extension to time-harmonic variational formulations governing the behavior of dynamic linear electromagnetic systems is presented in Appendix B and it has been submitted for publication in the journal *Structural and Multidisciplinary Optimization*.

In that article we apply the derived sensitivity formulas to the optimal design of a three-dimensional planar multi-layer busbar through a density based topology optimization. This paper proposes an approach to minimize the mismatch between the complex currents that go through the electronic power switching components of the busbar, while filling at most a given volume fraction of the available domain.

2.2. An efficient iterative linear solver for MMA subproblems in a high dimensional design space

Our second contribution aims at offering a tailored iterative solver which finds efficiently the solution of a sequence of convex and separable large-scale optimization problems submitted to local restrictions. These are associated to each point of the region where topology optimization is applied, involving thus at least as many constraints as design variables.

As we have seen in Section 1.4, either dual maximization solvers or interior

point solvers are classically used to determine the solution of such problems. However, the dimensionality of the dual space tends to grow drastically, while the interior point method involves the assembly and the solution of a sequence of dense and large-scale linearized KKT systems. In each case, the computational effort involved in their repeated solutions becomes comparable to the effort involved in repeated solutions of the PDEs, thus dominating the computational cost of the whole optimization iterative process. Both approaches require hence some adaptations.

We first realize the replacement of the direct linear solver of the interior point method with an iterative method, e.g. preconditioned conjugate gradient (PCG), so as to solve the optimization problem in a CPU time comparable to the global design criterion problem, the so-called *compliance problem*. We design the preconditionner as an approximated Cholesky factorization of only a few KKT matrix columns, rather than the whole matrix, selected so as to exhibit good spectral properties. Furthermore, our preconditioner requires memory bounded by the size of the problem rather then the number of nonzero entries of the system matrix, as it is the case of classical incomplete Cholesky factorizations or approximate inverse preconditioners. The preconditioner avoids any excessive storage as the system matrix is only used to perform multiplication with a vector.

We further improve the effectiveness of the approach, on a second hand, by advantageously reducing the density of the system matrix through the truncation of the smallest entries of the sensitivity matrix. The truncation can be motivated by the St Venant principle and leads thus to a sparse preconditioner.

We applied successfully the interior point method based on both preconditioners to two of the most classical topology optimization benchmarks with stress constraints: the two bar truss as well as the L-shape. The computational cost of the overall solver tends to grow as $O(N^2)$ instead of $O(N^3)$, with N the number of finite elements.

This second contribution has been submitted for publication in *International Journal for Numerical Methods in Engineering* and is reproduced in Appendix C.

2.3. Optimization in mixed shape and topology design spaces

Our third set of contributions aims at presenting a unified framework for the simultaneous application of shape and topology optimization in industrial design problems, based on the sensitivity analysis presented in Kuci et al. [2017]. The topology optimization design variables, which are called *densities*, are by essence substantial quantities. This means that they are attached to matter while, on the other hand, shape optimization implies ongoing changes of the model geometry. We have therefore combined appropriately the two representations to ensure a consistent parameter space as the joint shape-topology optimization process un-

folds.

As we have summarized in Section 1.5, only little work about joint shape-topology optimization has been reported so far in the literature. In the context of packaging, for instance, the position (see Zhu et al. [2009]) and shape, (see Zhang et al. [2012]) of the packaged items are determined by a shape optimization process while, at the same time, the protective material usage is minimized by means of a density based topology optimization, see for instance Qian and Ananthasuresh [2004], or Zhang et al. [2011], so as to, e.g., minimize the overall volume of the package. An alternative approach with a fixed mesh is also possible. A level set representation of the component boundaries is used, instead of a CAD representation as in Osher and Sethian [1988], and the model is solved with an extended finite element method (XFEM), see Zhang et al. [2012].

We obtain the solution of the joint optimization problem by a gradient-based sequential convex programming approach, called Method of the Moving Asymptotes (MMA). Analytical sensitivities have been used in the past for analysis based on XFEM, see for instance Zhang et al. [2012], but, as far as FEM based analysis are concerned, a semi-analytic approach is used in general and it is reported for linear elasticity problems only. Building on the same methodology as in Kuci et al. [2017], we derive the sensitivity with respect to densities in a unified fashion, with the velocity method, by means of an explicit Lie differentiation of the FEM terms.

The method is applied to the torque ripple minimization in an interior permanent-magnet machine, with a limiting constraint on the weight of the optimal design.

This third contribution is still a draft paper and is reproduced in Appendix D.

Chapter

3 Application examples – towards industrial designs

Torque ripple in electrical rotating machines comes along with mechanical vibrations and acoustic noise, see for instance Tang et al. [2005]. Noise generation is generally important to minimize in all environments, while vibrations can mechanically damage the electrical machine itself (especially bearings), and can adversely influence on the driven machinery, reducing its life-time and reliability. It is therefore desired to reduce torque ripple as much as possible.

The use of modern power electronics converters at all levels of electrical power applications involves switching components with very low switching times and always increasing current levels, which bring parasite stray inductances and capacitances. Thus, laminated busbars, i.e. a thick strip of copper or aluminum, interconnect the power switching devices to other electronic components in power converters. Impedance asymmetry can appear and hence lead to current imbalance between the outputs of the busbar, especially during transients of the switching power devices, see for instance Ohi et al. [1999]. So, the main challenge lies in defining the appropriate topology of the device to make them compact, light or inexpensive without compromising their performances (e.g. power losses, electromagnetic compatibility and interference).

To tackle these issues, we use here the complete automated framework developed for shape and topology optimization. At the end of this project, we are able to determine optimal designs of an interior permanent-magnet (IPM) machine (see Appendix D) as well as a planar multi-layer busbar (see Appendix B). In addition, a smooth CAD model of the optimized systems is obtained from the finite element representation of the density field. The geometrical model can hence be used in later design stages. We provide here qualitative results rather than quantitative results, leaving aside the mathematics since they are included in the articles.

All the numerical simulations have been performed using the open-source software GetDP (Dular et al. [1998]), Gmsh (Geuzaine and Remacle [2009]) and our Python-based implementation of MMA (Svanberg [1987]).

3.1. Torque ripple minimization of a PMSM

A 3-phase interior permanent-magnet synchronous machine (PMSM) fed by a sinusoidal current is considered. We describe the geometry of the PMSM by a two dimensional CAD model. The PMSM behavior is modeled as a nonlinear magnetostatic formulation written in terms of the magnetic vector potential, see Fig. 3.1. These kinds of machines exhibit magnetic saturation (which occur in steel parts) and suffer from a high level of torque ripple which should be reduced as much as possible, while keeping the average torque above or equal to the nominal torque of the machine.

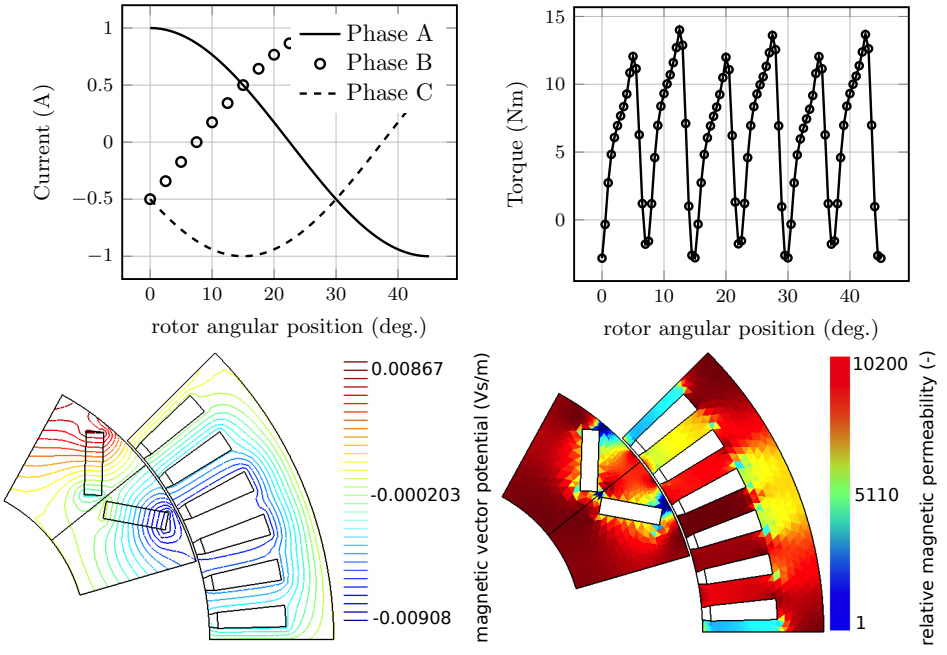

Figure 3.1: *A 3-phase interior permanent-magnet (IPM) machine fed by a sinusoidal current, top left, and modeled by a nonlinear magnetostatic formulation in terms of the magnetic vector potential* $\boldsymbol{A}$*, isovalues shown in bottom left, is considered. The magnetic permeability map at a given rotor position, bottom right, indicates a magnetic saturation (blue) in many regions of the steel parts where the induction flux is high. The torque ripple, top right, is particularly high for this type of machines. It should be reduced as much as possible.*

We perform a combined shape and topology optimization to determine simultaneously (1) the distance of the PMs from the air gap, the angle between the PMs, both set as shape design variables, and also (2) the steel fraction field which represents the density distribution in the rest of the rotor. The entire analysis domain and design domain are discretized using an average of 38,000 nodes and 65,000 triangular elements. The density design variables are used to interpolate the magnetic reluctivity through a classical SIMP with a penalization parameter fixed to 3. We want to smooth the torque with respect to the movement of the rotor, minimizing hence the torque ripple, while preserving an average torque to match the nominal torque of the machine. In addition, we considered a resource constraint defined as a given volume fraction of the available domain. In practice, we consider the torque variance instead of the torque ripple.

The evaluation of the performance functions, i.e. the torque variance as well as the average torque, for a given geometrical configuration of the PMs and a given steel distribution in the rotor, requires the knowledge of the torque at several angular positions of the rotor. Thus one has to solve nonlinear magnetostatic problems for these particular values of the design variables. This implies solving anew the nonlinear magnetostatic problem for the N_p angular positions. The repetition of these evaluations is time-consuming and the number of iteration steps should be kept as small as possible.

The results of the optimization problem are summarized in Fig. 3.2. The optimization process results, after roughly 260 iterations, in PMs with increased angular openings compared to the original design. The topology optimization allows, in this particular case, major improvements of torque profile of the electrical rotating machine. The torque ripple is reduced by a factor of 30 while the average torque is set to the nominal torque of the machine.

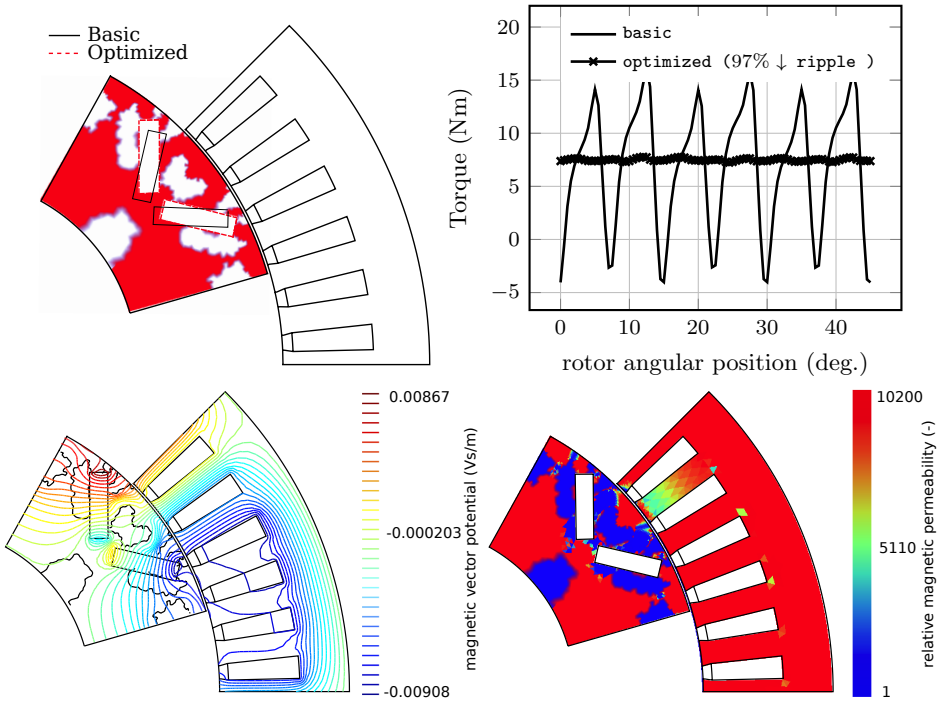

Figure 3.2: *A range of $N_p = 16$ rotor angular positions which covers an angular torque period, from 0 to 16 degrees has been considered and the geometrical configuration of the PMs as well as the steel distribution in the rotor, with a volume fraction of 70%, have been determined simultaneously with a simultaneous shape and topology optimization. This approach leads to a drastic reduction of torque ripple while keeping the average torque to the desired nominal torque, set as $7(Nm)$. The distribution of magnetic vector potential field, iso-values in bottom left, provides a relative magnetic permeability, bottom right, where the magnetic saturations have been greatly reduced compared to the initial design, Fig. 3.1.*

3.2. Simultaneous shape and topology optimization for torque performance and centrifugal resistance in electrical rotating machine

The optimization problem of the previous section was mainly based on the magnetic performance of the machine. The optimized geometrical configuration results in a rotor with thin parts, for which the structural strength is not necessarily guaranteed, see Fig. 3.3. The optimized rotor which meets the torque requirements exhibits a larger displacement and the gap between rotor and stator might be modified. To express the mechanical resistance in the rotor, we consider a linear elastic model of the rotor subjected to the centrifugal body load, with a rotating speed of 6000 r.p.m.

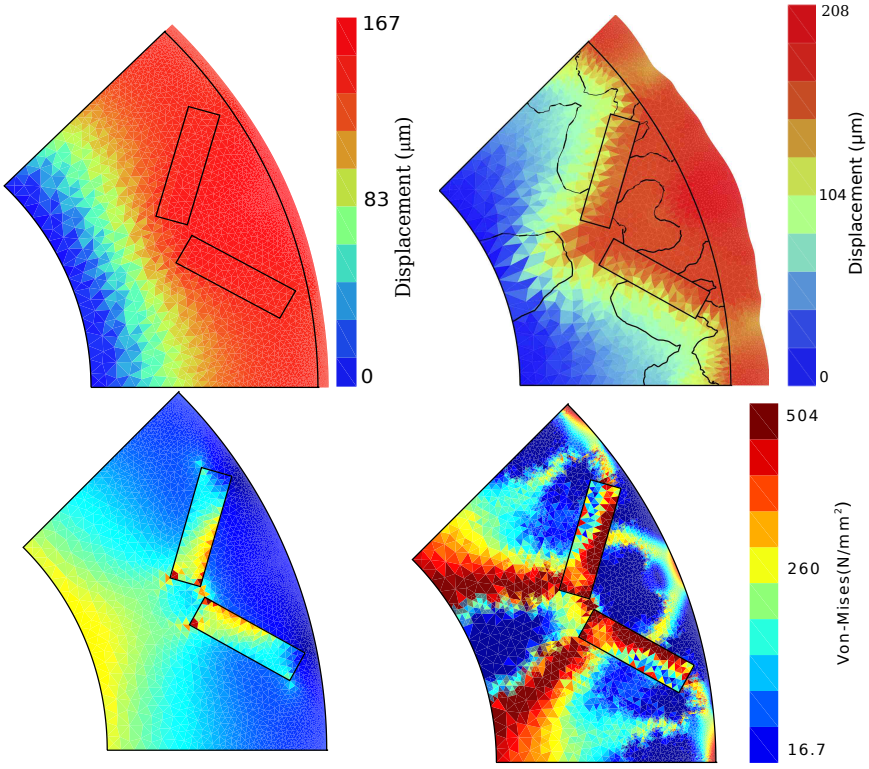

Figure 3.3: *A linear elastic model of the clamped rotor excited by a centrifugal force is considered. The optimized rotor which meets the torque requirements exhibits a larger displacement (magnified with a factor 20), top, and a higher level of Von-Mises stress criterion, bottom, than the basic design, showing hence that structural design criterion should be included in the optimization problem.*

We consider the compliance of the rotor steel parts, and the compliance of the PMs. We can then account for the structural design criterion so as to limit the displacement of the steel parts as well as the PMs. In addition, we should also take into account the local resistance of the material. Thus we will consider the p-norm of the ϵ-relaxed Von-Mises stresses, as proposed by Duysinx and Sigmund [1998], in the steel parts, as well as in the PMs. Thus, we will keep the stress level under a provided yield stress, σ_l, and thus ensure the mechanical strength of the design of the electrical rotating machine.

A combined shape and topology optimization is still carried out here to determine the design variables defined in the design of previous section, so as to meet the torque requirements while constraining the compliance and the Von-Mises stress criterion, both in the steel parts of the rotor and in the PMs.

For a given geometrical configuration of the PMs and a given steel distribution in the rotor, the displacement field is determined by solving the linear elastic problem and also the compliance and the Von-Mises stresses, in addition to the evaluation of the performance functions involving the torque requirements. It should be noticed that magnetic problem still requires several nonlinear magnetostatic resolutions for the whole range of angular positions of the rotor, while linear elasticity can be solved in one step.

The results of the optimization problem which includes the structural design constraint and the torque ripple minimization are summarized in Fig. 3.4. The optimization process results in PMs with an increased angular opening compared to the original design. In addition to removing material from all the regions where saturation occurs, and where the magnetic flux density is very low, topology optimization solution suggests to surround the permanent magnets with steel so as to reduce their displacement as well as the limiting Von-Mises stress. The torque ripple is still greatly reduced by 90% while the average torque is set to the nominal torque of the machine.

The solution of the density based topology optimization is often considered as conceptual. A post-processing stage is hence needed to obtain a manufacturable design, see for instance Hsu and Hsu [2005] or more recently Zegard and Paulino [2016]. Computer vision technologies to represent the boundary of the void-solid finite element topology optimization result have first been performed in Bendsøe and Rodrigues [1991], or Lin and Chao [2000]. A density contour approach has also been used in Kumar and Gossard [1996], or Hsu et al. [2001] as well as a geometric reconstruction approach, see for instance Tang and Chang [2001].

Here we performed a spline-based interpolation of the density isovalues. This then leads to a CAD model which may be used for latter design stages as well as e.g. for additive manufacturing purposes, see Fig. 3.5. However, a drawback inherent to such procedures, is that post-processed results are no longer optimal and may also not comply with the given design criteria, thus slightly deteriorating the topology optimization solutions. In this particular case, the torque ripple is

increased by 10% from the one computed with the density field.

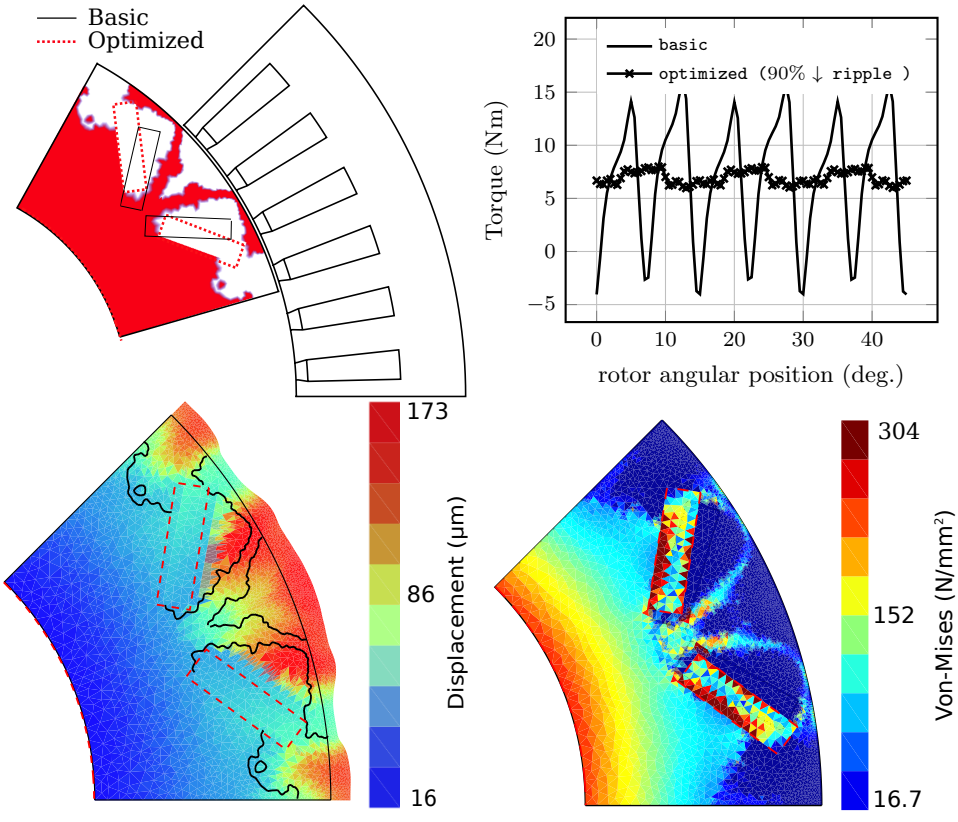

Figure 3.4: *The optimization problem that includes the mechanical design restrictions, by means of the constraints on the compliance and on the p-norm of the Von-Mises stresses, is considered. This formulation aims at determining simultaneously the geometrical configuration of the PMs as well as the steel distribution in the rotor. A volume fraction of 70% is considered. A nonlinear magnetostatic problem is solved for each angular position of the rotor whereas a linear elastic problem excited by a centrifugal force is solved for only a single rotor position. A drastic reduction of torque ripple is obtained while keeping the average torque to the desired nominal torque, set as 7(Nm). The optimized structure exhibits a displacement level (magnified with a factor 20) and Von-Mises stress distribution that are feasible from a mechanical point of view.*

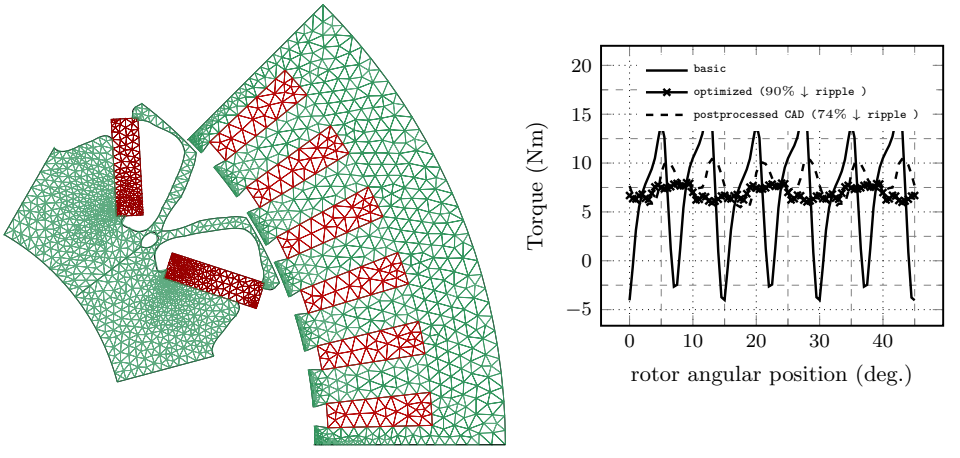

Figure 3.5: *A smooth CAD model of the optimized rotor is obtained manually from the finite element representation of Fig. 3.4 by making use of spline curves. The geometrical model can hence be used in later design stages.*

3.3. Impedance mismatch reduction in 3D multi-layer high voltage busbars

In this application we consider a multi-layer and high-voltage busbar based on the basic operation of a power electronic inverter. A representative laminated busbar is made up of tightly pressed conducting plates separated by a thin dielectric material for insulation. Due to the relevance of the input impedance in terms of design and optimization, the model is simplified, shorting one phase at the time, calculating the impedance at different frequencies. The DC source of the inverter is replaced by a sinusoidal current source which splits into two separate currents in the vertical bars, I_{Σ_1} and I_{Σ_2}, that reunite and leave the system through the output boundary. The geometry of the representative busbar is described by a 3D CAD model, while the system is modeled in terms of a volumetric time-harmonic magnetodynamic $\boldsymbol{A} - v$ formulation, with $\boldsymbol{A}$ the magnetic vector potential, and v the electric potential on the conducting regions of the busbar, Fig. 3.6.

However, the original model is computationally costly, since at higher frequencies the mesh needs to be refined to match at least two layers of finite elements per skin depth, which increases the size of the problem as the frequency increases. It should be noted that an equivalent model in which the conducting domains can be simplified to surfaces and lines can be implemented (shell model). This can be done applying geometry transformations and including explicitly the skin effect term in the formulation, see Geuzaine [2001].

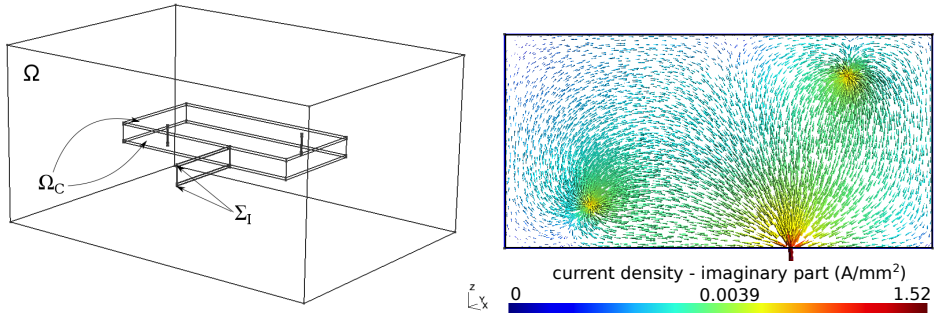

Figure 3.6: *Considered three-dimensional busbar fed by a sinusoidal current and modeled in terms of a volumetric and linear time-harmonic magnetodynamic $\boldsymbol{A} - v$ formulation (scaling factor of 10 in the z direction for better visibility). The current injected in the horizontal bar splits into two separate currents in the vertical bars, bottom, that reunite and leave the system through the output boundary.*

We want to minimize the current imbalance between the outputs of the busbar and hence reduce the impedance asymmetry, while preserving the impedance from the initial design. To this end, we consider the L2-norm of the current mismatch between the complex valued currents, $\|I_{\Sigma_1} - I_{\Sigma_2}\|$. In addition, we considered a resource constraint defined as a given volume fraction of the available domain.

The busbar is optimized for two frequencies: 500 Hz and 50 kHz, corresponding respectively to a mostly resistive and to an inductive behavior. The mesh is refined as the frequency increases so as to have about two elements in the skin depth, leading to a mesh with 112 794 tetrahedral finite elements at 500 Hz and a mesh with 360 962 tetrahedral finite elements at 50 kHz. In this context, a density design variable, is defined in each finite element of the mesh and is allowed to vary between a lower bound that represents air, and an upper bound that represents copper.

A density based topology optimization problem is used and aims et determining the optimal distribution of copper in both plates so as to minimize the squared L2-norm of the current mismatch between the outputs (vertical vias) of the busbar, especially for an high frequency input current. A logarithmic interpolation scheme assigns conductivity to points of intermediate density. Special care has been taken in the selection of the interpolation scheme as the magnitude of the conductivity at the upper bound of density strongly affects the solution of the physical problem, and thus the span of several order of magnitudes of the conductivity, typically 10^7, in the design domain is crucial.

The results of the optimization problem are summarized in Fig. 3.7. The optimization process results, after a 100 iterations (at 500 Hz) and 350 iterations (at 50 kHz), in a copper distribution different in each plate which brings current paths that allow a drastic reduction of the IGBTs currents mismatch. The copper paths are thinner compared to the original design. The optimized design enables to reduce the current mismatch in the two vertical branches from 36% to 0.2% at 500 Hz and from 42% to 0.1% at 50 kHz. A smooth CAD model of the optimized rotor is obtained manually from the finite element representation of Fig. 3.7 by making use of spline curves, see Fig. 3.8.

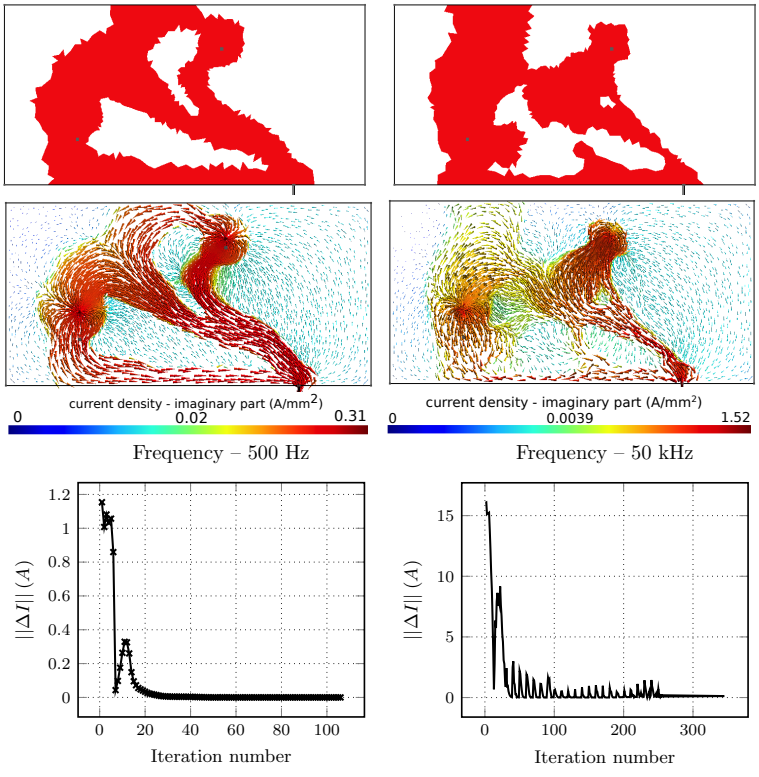

Figure 3.7: *The busbar is fed with a current of* 500 *Hz (left column), as well as a current of* 50 *kHz and the optimal copper distribution, top, of its plates is obtained for both frequencies, as well as the current density, middle, for a volume constraint set as* 50% *of the available volume. In all cases the current sharing between the vertical vias is greatly reduced compared to the initial design.*

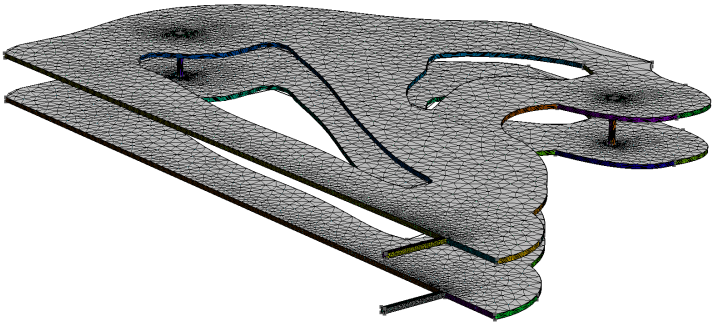

Figure 3.8: *A smooth CAD model of the optimized busbar plates is obtained manually from the finite element representation of Fig. 3.7 by making use of spline curves.*

Conclusions and Outlook

The objective of this thesis was threefold: (1) develop the rigorous and general formulation of the sensitivity of constrained optimization problems based on PDEs solution which arise from electromagnetics, in view of handling industrial design of electromagnetic systems through either a shape optimization or a topology optimization; (2) develop an efficient iterative solver for the solution of the very large-scale problem when one has to cope with a huge number of local constraints, for the method of moving asymptotes subproblems; and (3) develop the optimal design capabilities by performing a simultaneous shape and topology optimization of the system through this framework.

As was reviewed in Chapter 1, numerous techniques have been proposed over the years to differentiate either the discretized algebraic system of the PDEs that govern the physical problem, or on the other hand, their variational form, mostly arising in the area of structural mechanics. Applications in other disciplines such as electromagnetics have also been proposed, but have been limited to problems expressed in terms of a scalar potential, leaving aside the problem of handling vector unknown fields. We have therefore derived a general framework for analysis which extends the calculation of sensitivity to the vector field case, for both static and time-harmonic PDEs, in a unified and elegant fashion. In addition we are able to recover a number of results, previously obtained by other authors as particular cases. The proposed framework, which is based on the general differential geometry framework, expresses the sensitivity at a continuous level, prior to discretization, as a Lie derivative. Theoretical formulas for shape sensitivity are derived and described in detail, following both the direct and the adjoint approach. They are reformulated with conventional tensor and vector analysis notations. We have also derived an efficient method for the construction of the velocity field of the auxiliary flow that represents the shape modification of the system. Thus one can express the sensitivity locally as a volume integral over a single layer of finite elements connected to both sides of the surfaces undergoing shape modification. The complete and general automatic sensitivity computation tool has been val-

idated with the finite difference approach and the convergence of the computed sensitivity with mesh refinement has been investigated.

For the second problem that we have investigated, we have redesigned the linear algebra kernel of the interior point method used to solve the mathematical programming problem, in the context of an MMA approximation of the original problem. A key point of our work is to avoid the storage of matrices which are often too large to be stored in computer memory. Such large-scale problems arise, in general, in structural topology optimization with local stresses associated to each finite element of a mesh, and involve both a large number of design variables and a large number of constraints. The iterative solver of the KKT solution requires the use of suitably preconditioned iterative method. In our approach, we resort to successive modified partial Cholesky factorizations of system matrix blocks, with an advantageously reduced density obtained with the truncation of the smallest entries of the sensitivity matrix. The feasibility of the sparse preconditioned iterative method has been showcased with the classical benchmark problems of stress constrained topology optimization.

For the third investigated problem we have developed a unified tool for handling simultaneously the complex interactions between the material distribution model of topology optimization and the geometrical modifications which occur throughout a shape optimization. Following the general framework of sensitivity analysis derived so far, shape sensitivity is computed efficiently. We can obtain simultaneously the sensitivity with respect to shape design variables as well as material densities.

The theoretical results gathered in the thesis have been implemented within ONELAB and have been successfully applied to electro-mechanical optimization of the shape and topology of energy conversion systems which are of a great importance in industry. The design of an electrical rotating machine with permanent magnets, modeled by means of a two-dimensional CAD model coupled to a nonlinear magnetostatic formulation, and aiming to minimize the torque ripple has been first considered. In addition mechanical design requirements such as stress and displacement constraints have been included in the design formulation so as to ensure the mechanical feasibility of the rotor submitted to centrifugal forces. Finally, a three-dimensional planar multi-layer busbar modeled in terms of a time-harmonic magnetodynamic problem has been considered so as to minimize the impedance mismatch.

Perspectives

Many short and medium term perspectives for future works exist:

1. The losses which occur in the steel parts, e.g. stator, as well as in the permanent magnets of electrical rotating machines, see for instance Gyselinck et al. [1999], should be included in the formulation of the problem of optimization.

Such a problem involves performance functions expressed as time integrals, over the period of the losses variations, and evaluated hence through the solutions of the time-domain PDEs at each time step of that period. An adaptation of the sensitivity analysis obtained so far in this work must be carried out, so as to take into account the history of the time solutions of the physical problem.

2. In the context of a multidisciplinary design optimization, there could be various strategies to formulate the design problem of electrical machines in order to deal with multiphysical couplings, such as mechanical vibrations and heating. Since high current can damage electronic components, cause high energy loss and consequently increase thermal stress, one can for instance determine the optimal current density of windings, in addition to the geometrical parameters or the material densities of the rotor.

3. The magnetic force can be included in the design in addition to the centrifugal force, so as to account for low-speed electrical rotating machines. They can also account for radial forces acting on stator casing, which give rise to excitation of the stator and noise and vibration generation, see for instance Hor et al. [1998].

4. An alternative formulation, called simultaneous analysis and design (SAND), as it has been discussed since the 1960s in the seminal work of Schmit and Fox [1965], or more recently in Rojas-Labanda and Stolpe [2015], can be performed instead of the classical optimization problem formulation. In this approach, the design variables and the solution field of the PDEs are considered simultaneously as independent optimization variables, while the PDEs are considered as equality constraints and hence need not be fully satisfied at every iteration. This can be advantageous for nonlinear problems. Although this alternative formulation leads to much larger algebraic problem sizes compared to the classical approach because of the increase of variables in a single optimization process, the Jacobian of the constraints becomes more sparse, which makes the SAND approach quite competitive compared to the conventional nested approach, and even more efficient for large-scale problems. It has been shown so far that the nested formulation of the optimal design problem brings considerable complexity in the calculation of the sensitivity analysis, in particular in shape optimization where there is an implicit dependency between the variation of the geometry and the variation of the state variable, which can be avoided advantageously in a SAND approach of the design problem, since there is no more coupling between the solution of the physical PDEs and the design variables, and hence the sensitivity analysis is greatly simplified.

Many long-term perspectives also exist:

1. A possible extension may be initiated for handling multi-material optimizations, i.e., finding an optimal configuration consisting of three or more differ-

ent materials, as in Bendsøe and Sigmund [1999] or more recently in Labbé [2011]. In addition, one would like to consider discrete properties such as the number of poles of an electrical rotating machine, or the number of power switches in a busbar. In this approach, the design variables can either be continuous as in a SIMP-like approach, or take a given number of values indicating the material that is used.

2. The free-form nature of topology optimization, and its ability to discover novel geometries, makes it a natural design tool for integration with *additive manufacturing* (AM) processes. Manufacturing limitations however still remain, see for instance Gao et al. [2015], and ultimately must be tightly integrated within the topology optimization methodology to fully extend the capabilities and freedom provided by AM processes. The design space should hence be restricted so that the features (members) in the final topology are prescribed to satisfy a minimum length scale by imposing e.g. the local slope constraints that limit the variation in between adjacent elements, as in Petersson and Sigmund [1998] or following the more recent approach by Guest et al. [2004].

3. The constraints on the slope occurring in an AM process are one example among others that involve local constraints and therefore lead to a very large-scale optimization problem. The development of the sequential convex programming algorithm should combine the massively distributed modern computer resources with physics-based simplifications of the problem. The hierarchical matrices and their algebra, see for instance Börm et al. [2003], also belong to a promising research field which may lead to efficient KKT solvers. Another interesting perspective is to have a look at other physical engineering problems such as the design of electromagnetic systems, and adapt the successive approximations to the sought system. It is also an interesting question to adapt the sequential convex programming algorithm to work with both discrete and continuous design variables, following for instance Beckers [1999], Schmit and Fleury [1980] or more recently Svanberg and Werme [2007] so as to be able to select materials from existing catalogues.

Bibliography

N. Aage, T. H. Poulsen, A. Gersborg-Hansen, and O. Sigmund. Topology optimization of large scale stokes flow problems. *Structural and Multidisciplinary Optimization*, 35(2):175–180, 2008.

H. M. Adelman and R. T. Haftka. Sensitivity analysis of discrete structural systems. *AIAA journal*, 24(5):823–832, 1986.

G. Allaire and F. Jouve. Minimum stress optimal design with the level set method. *Engineering analysis with boundary elements*, 32(11):909–918, 2008.

G. Allaire, F. Jouve, and A.-M. Toader. A level-set method for shape optimization. *Comptes Rendus Mathematique*, 334(12):1125–1130, 2002.

G. Allaire, F. Jouve, and A.-M. Toader. Structural optimization using sensitivity analysis and a level-set method. *Journal of computational physics*, 194(1):363–393, 2004.

J. S. Arora and E. J. Haug. Methods of design sensitivity analysis in structural optimization. *AIAA journal*, 17(9):970–974, 1979.

R. Balamurugan, C. Ramakrishnan, and N. Singh. Performance evaluation of a two stage adaptive genetic algorithm (tsaga) in structural topology optimization. *Applied Soft Computing*, 8(4):1607–1624, 2008.

M. Beckers. Topology optimization using a dual method with discrete variables. *Structural Optimization*, 17(1):14–24, 1999.

P. Beckers. Recent developments in shape sensitivity analysis: the physical approach. *Engineering optimization*, 18(1-3):67–78, 1991.

A. Belegundu and S. Rajan. A shape optimization approach based on natural design variables and shape functions. *Computer Methods in Applied Mechanics and Engineering*, 66(1):87–106, 1988.

M. P. Bendsøe. Optimal shape design as a material distribution problem. *Structural and multidisciplinary optimization*, 1(4):193–202, 1989.

M. P. Bendsøe and N. Kikuchi. Generating optimal topologies in structural design using a homogenization method. *Computer methods in applied mechanics and engineering*, 71(2):197–224, 1988.

M. P. Bendsøe and H. C. Rodrigues. Integrated topology and boundary shape optimization of 2-d solids. *Computer Methods in Applied Mechanics and Engineering*, 87(1):15–34, 1991.

M. P. Bendsøe and O. Sigmund. Material interpolation schemes in topology optimization. *Archive of applied mechanics*, 69(9):635–654, 1999.

H. Y. Benson, D. F. Shanno, and R. J. Vanderbei. A comparative study of large-scale nonlinear optimization algorithms. In *High performance algorithms and software for nonlinear optimization*, pages 95–127. Springer, 2003.

N. Bianchi and S. Bolognani. Design techniques for reducing the cogging torque in surface-mounted PM motors. *IEEE Transactions on Industry Applications*, 38(5):1259–1265, 2002.

N. Bianchi, S. Bolognani, D. Bon, and M. Dai Pre. Rotor flux-barrier design for torque ripple reduction in synchronous reluctance and PM-assisted synchronous reluctance motors. *IEEE Transactions on Industry Applications*, 45(3):921–928, 2009.

J. Biedinger and D. Lemoine. Shape sensitivity analysis of magnetic forces. *IEEE Transactions on Magnetics*, 33(3):2309–2316, 1997.

C. Bischof, P. Khademi, A. Mauer, and A. Carle. Adifor 2.0: Automatic differentiation of fortran 77 programs. *IEEE Computational Science and Engineering*, 3(3):18–32, 1996.

K.-U. Bletzinger and K. Maute. Towards generalized shape and topology optimization. *Engineering Optimization*, 29(1-4):201–216, 1997.

K.-U. Bletzinger, M. Firl, J. Linhard, and R. Wüchner. Optimal shapes of mechanically motivated surfaces. *Computer methods in applied mechanics and engineering*, 199(5):324–333, 2010.

A. Boglietti, A. M. El-Refaie, O. Drubel, A. M. Omekanda, N. Bianchi, E. B. Agamloh, M. Popescu, A. Di Gerlando, and J. B. Bartolo. Electrical machine topologies: Hottest topics in the electrical machine research community. *IEEE Industrial Electronics Magazine*, 8(2):18–30, 2014.

P. I. Borel, L. H. Frandsen, A. Harpøth, M. Kristensen, J. S. Jensen, and O. Sigmund. Topology optimised broadband photonic crystal y-splitter. *Electronics Letters*, 41(2):69–71, 2005.

C. A. Borghi, D. Casadei, A. Cristofolini, M. Fabbri, and G. Serra. Application of a multiobjective minimization technique for reducing the torque ripple in permanent-magnet motors. *IEEE Transactions on Magnetics*, 35(5):4238–4246, 1999.

S. Börm, L. Grasedyck, and W. Hackbusch. Introduction to hierarchical matrices with applications. *Engineering analysis with boundary elements*, 27(5):405–422, 2003.

M. Botkin. Shape optimization of plate and shell structures. *AIAA Journal*, 20 (2):268–273, 1982.

V. Braibant and C. Fleury. Shape optimal design using b-splines. *Computer Methods in Applied Mechanics and Engineering*, 44(3):247–267, 1984.

M. Bruggi. On an alternative approach to stress constraints relaxation in topology optimization. *Structural and multidisciplinary optimization*, 36(2):125–141, 2008.

S. Burtovoy and I. Galkin. Geometry optimization of half-bridge converter with symmetrical busbar structure. In *Electronics Conference (BEC), 2012 13th Biennial Baltic*, pages 251–254. IEEE, 2012.

M. Buschendorf, M. Köbe, R. Alvarez, and S. Bernet. Comprehensive design of dc busbars for medium voltage applications. In *Energy Conversion Congress and Exposition (ECCE), 2013 IEEE*, pages 1880–1885. IEEE, 2013.

J.-K. Byun and I.-H. Park. Design of dielectric waveguide filters using topology optimization technique. *IEEE Transactions on Magnetics*, 43(4):1573–1576, 2007.

O. Canyurt and P. Hajela. A sand approach based on cellular computation models for analysis and optimization. *Engineering Optimization*, 39(4):381–396, 2007.

M. C. Caponet, F. Profumo, R. W. De Doncker, and A. Tenconi. Low stray inductance bus bar design and construction for good emc performance in power electronic circuits. *IEEE Transactions on Power Electronics*, 17(2):225–231, 2002.

C. Chen, X. Pei, Y. Shi, X. Lin, X. Liu, and Y. Kang. Modeling and optimization of high power inverter three-layer laminated busbar. In *Energy Conversion Congress and Exposition (ECCE), 2012 IEEE*, pages 1380–1385. IEEE, 2012.

C. Chen, X. Pei, Y. Chen, and Y. Kang. Investigation, evaluation, and optimization of stray inductance in laminated busbar. *IEEE Transactions on Power Electronics*, 29(7):3679–3693, 2014.

G. Cheng and X. Guo. ε-relaxed approach in structural topology optimization. *Structural and Multidisciplinary Optimization*, 13(4):258–266, 1997.

G. Cheng and Z. Jiang. Study on topology optimization with stress constraints. *Engineering Optimization*, 20(2):129–148, 1992.

J. S. Choi, K. Izui, S. Nishiwaki, A. Kawamoto, and T. Nomura. Topology optimization of the stator for minimizing cogging torque of IPM motors. *IEEE Transactions on Magnetics*, 47(10):3024–3027, 2011.

J. S. Choi, K. Izui, S. Nishiwaki, A. Kawamoto, and T. Nomura. Rotor pole design of IPM motors for a sinusoidal air-gap flux density distribution. *Structural and Multidisciplinary Optimization*, 46(3):445–455, 2012.

K. K. Choi. *Shape design sensitivity analysis and optimal design of structural systems*. Springer, 1987.

K. K. Choi and T.-M. Yao. On 3-D modeling and automatic regridding in shape design sensitivity analysis. *NASA Conference Publication*, 2457:329–345, 1987.

A. N. Christiansen, M. Nobel-Jørgensen, N. Aage, O. Sigmund, and J. A. Bærentzen. Topology optimization using an explicit interface representation. *Structural and Multidisciplinary Optimization*, 49(3):387–399, 2014.

G. Dajaku and D. Gerling. Air-gap flux density characteristics of salient pole synchronous permanent-magnet machines. *IEEE Transactions on Magnetics*, 48(7):2196–2204, 2012.

J. Daňková and J. Haslinger. Numerical realization of a fictitious domain approach used in shape optimization. part i: Distributed controls. *Applications of Mathematics*, 41(2):123–147, 1996.

J. De La Ree and N. Boules. Induced voltage harmonic reduction of PM cylindrical machines. *IEEE Transactions on Industry Applications*, 28(3):619–624, 1992.

M. C. Delfour and J.-P. Zolésio. *Shapes and geometries: metrics, analysis, differential calculus, and optimization*. SIAM, 2011.

K. Dems and Z. Mroz. Variational approach by means of adjoint systems to structural optimization and sensitivity analysis -II: Structure shape variation. *International Journal of Solids and Structures*, 20(6):527–552, 1984.

E. D. Dolan and J. J. Moré. Benchmarking optimization software with performance profiles. *Mathematical programming*, 91(2):201–213, 2002.

T. Dreyer, B. Maar, and V. Schulz. Multigrid optimization in applications. *Journal of Computational and Applied Mathematics*, 120(1):67–84, 2000.

F. Duboeuf and E. Béchet. Embedded solids of any dimension in the x-fem. part i—building a dedicated p1 function space. *Finite Elements in Analysis and Design*, 130:80–101, 2017.

M. B. Dühring, J. S. Jensen, and O. Sigmund. Acoustic design by topology optimization. *Journal of sound and vibration*, 317(3):557–575, 2008.

M. B. Dühring, O. Sigmund, and T. Feurer. Design of photonic bandgap fibers by topology optimization. *JOSA B*, 27(1):51–58, 2010.

P. Dular, C. Geuzaine, F. Henrotte, and W. Legros. A general environment for the treatment of discrete problems and its application to the finite element method. *IEEE Transactions on Magnetics*, 34(5):3395–3398, Sept. 1998.

P. Dular, C. Geuzaine, A. Genon, and W. Legros. An evolutive software environment for teaching finite element methods in electromagnetism. *IEEE Transactions on Magnetics*, 35(3):1682–1685, May 1999.

P. Duysinx and M. P. Bendsøe. Topology optimization of continuum structures with local stress constraints. *International journal for numerical methods in engineering*, 43(8):1453–1478, 1998.

P. Duysinx and O. Sigmund. New developments in handling stress constraints in optimal material distribution. *Proceedings of the 7th AIAA/USAF/NASAISSMO Symp on Multidisciplinary Analysis and Optimization*, 1:1501–1509, 1998.

D. N. Dyck and D. A. Lowther. Automated design of magnetic devices by optimizing material distribution. *IEEE Transactions on Magnetics*, 32(3):1188–1193, 1996.

D. N. Dyck and D. A. Lowther. Composite microstructure of permeable material for the optimized material distribution method of automated design. *IEEE Transactions on Magnetics*, 33(2):1828–1831, 1997.

H. A. Eschenauer and N. Olhoff. Topology optimization of continuum structures: a review. *Applied Mechanics Reviews*, 54(4):331–390, 2001.

H. A. Eschenauer, V. V. Kobelev, and A. Schumacher. Bubble method for topology and shape optimization of structures. *Structural and Multidisciplinary Optimization*, 8(1):42–51, 1994.

P. E. Farrell, D. A. Ham, S. W. Funke, and M. E. Rognes. Automated derivation of the adjoint of high-level transient finite element programs. *SIAM Journal on Scientific Computing*, 35(4):C369–C393, 2013.

C. Fleury. Conlin: an efficient dual optimizer based on convex approximation concepts. *Structural Optimization*, 1(2):81–89, 1989.

C. Fleury. Sequential convex programming for structural optimization problems. In *Optimization of large structural systems*, pages 531–553. Springer, 1993.

A. Forsgren. Inertia-controlling factorizations for optimization algorithms. *Applied Numerical Mathematics*, 43(1-2):91–107, 2002.

T. Frankel. *The geometry of physics: an introduction*. Cambridge University Press, 2011.

W. Gao, Y. Zhang, D. Ramanujan, K. Ramani, Y. Chen, C. B. Williams, C. C. Wang, Y. C. Shin, S. Zhang, and P. D. Zavattieri. The status, challenges, and future of additive manufacturing in engineering. *Computer-Aided Design*, 69: 65–89, 2015.

C. Geuzaine. High order hybrid finite element schemes for maxwell's equations taking thin structures and global quantities into account. *University of Liege Faculty of Applied Sciences, doctoral thesis*, 2001.

C. Geuzaine and J.-F. Remacle. Gmsh: A 3-D finite element mesh generator with built-in pre-and post-processing facilities. *International Journal for Numerical Methods in Engineering*, 79(11):1309–1331, 2009.

P. E. Gill, M. A. Saunders, and E. Wong. On the performance of sqp methods for nonlinear optimization. In *Modeling and Optimization: Theory and Applications*, pages 95–123. Springer, 2015.

A. Griewank, D. Juedes, and J. Utke. Algorithm 755: Adol-c: a package for the automatic differentiation of algorithms written in c/c++. *ACM Transactions on Mathematical Software (TOMS)*, 22(2):131–167, 1996.

J. K. Guest, J. H. Prévost, and T. Belytschko. Achieving minimum length scale in topology optimization using nodal design variables and projection functions. *International journal for numerical methods in engineering*, 61(2):238–254, 2004.

J. Guichon, J. Aimé, J. Schanen, C. Martin, J. Roudet, E. Clavel, M. Arpilliere, R. Pasterczyk, and Y. Le Floch. Busbar design: How to spare nanohenries? In *Industry Applications Conference, 2006. 41st IAS Annual Meeting. Conference Record of the 2006 IEEE*, volume 4, pages 1865–1869. IEEE, 2006.

J. Gyselinck, L. Vandevelde, J. Melkebeek, P. Dular, F. Henrotte, and W. Legros. Calculation of eddy currents and associated losses in electrical steel laminations. *IEEE Transactions on Magnetics*, 35(3):1191–1194, 1999.

S.-H. Ha, K. Choi, and S. Cho. Numerical method for shape optimization using t-spline based isogeometric method. *Structural and Multidisciplinary Optimization*, 42(3):417–428, 2010.

R. T. Haftka and R. V. Grandhi. Structural shape optimization—a survey. *Computer methods in applied mechanics and engineering*, 57(1):91–106, 1986.

E. J. Haug and J. S. Arora. *Applied optimal design: mechanical and structural systems*. Wiley, 1979.

F. Henrotte. Handbook for the computation of electromagnetic forces in a continuous medium. *Int. Compumag Society Newsletter*, 24(2):3–9, 2004.

R. Hermann et al. Harley flanders, differential forms with applications to the physical sciences. *Bulletin of the American Mathematical Society*, 70(4):483–487, 1964.

R. Hiptmair and J. Li. Shape derivatives in differential forms i: An intrinsic perspective. *Annali di Matematica Pura ed Applicata*, 192(6):1077–1098, 2013.

R. Hiptmair and J. Li. Shape derivatives in differential forms ii: Shape derivatives for scattering problems. SAM Seminar for Applied Mathematics, ETH, Zürich, Switzerland, Research Report, 2017.

P. Hor, Z. Zhu, D. Howe, and J. Rees-Jones. Minimization of cogging force in a linear permanent magnet motor. *IEEE Transactions on Magnetics*, 34(5): 3544–3547, 1998.

M.-H. Hsu and Y.-L. Hsu. Interpreting three-dimensional structural topology optimization results. *Computers & structures*, 83(4-5):327–337, 2005.

Y.-L. Hsu, M.-S. Hsu, and C.-T. Chen. Interpreting results from topology optimization using density contours. *Computers & Structures*, 79(10):1049–1058, 2001.

T. J. Hughes, J. A. Cottrell, and Y. Bazilevs. Isogeometric analysis: cad, finite elements, nurbs, exact geometry and mesh refinement. *Computer methods in applied mechanics and engineering*, 194(39):4135–4195, 2005.

A. Iga, S. Nishiwaki, K. Izui, and M. Yoshimura. Topology optimization for thermal conductors considering design-dependent effects, including heat conduction and convection. *International Journal of Heat and Mass Transfer*, 52(11):2721–2732, 2009.

C.-H. Im, H.-K. Jung, and Y.-J. Kim. Hybrid genetic algorithm for electromagnetic topology optimization. *IEEE Transactions on Magnetics*, 39(5):2163–2169, 2003.

M. H. Imam. Three-dimensional shape optimization. *International Journal for Numerical Methods in Engineering*, 18(5):661–673, 1982.

K. A. James, E. Lee, and J. R. Martins. Stress-based topology optimization using an isoparametric level set method. *Finite Elements in Analysis and Design*, 58: 20–30, 2012.

H. A. Kalameh, O. Pierard, C. Friebel, and E. Béchet. Semi-implicit representation of sharp features with level sets. *Finite Elements in Analysis and Design*, 117: 31–45, 2016.

M. Khan, P. Magne, B. Bilgin, S. Wirasingha, and A. Emadi. Laminated busbar design criteria in power converters for electrified powertrain applications. In *Transportation Electrification Conference and Expo (ITEC), 2014 IEEE*, pages 1–6. IEEE, 2014.

D.-H. Kim, J. K. Sykulski, and D. A. Lowther. Design optimisation of electromagnetic devices using continuum design sensitivity analysis combined with commercial em software. *IET Science, Measurement & Technology*, 1(1):30–36, 2007a.

I. K. Kim, W. Kim, and Y. Y. Kim. Magnetostrictive grating with an optimal yoke for generating high-output frequency-tuned sh waves in a plate. *Sensors and Actuators A: Physical*, 137(1):141–146, 2007b.

N. Kim, K. Choi, and M. Botkin. Numerical method for shape optimization using meshfree method. *Structural and Multidisciplinary Optimization*, 24(6):418–429, 2002.

N. H. Kim and Y. Chang. Eulerian shape design sensitivity analysis and optimization with a fixed grid. *Computer methods in applied mechanics and engineering*, 194(30):3291–3314, 2005.

S.-I. Kim, G.-H. Lee, J.-P. Hong, and T.-U. Jung. Design process of interior PM synchronous motor for 42-v electric air-conditioner system in hybrid electric vehicle. *IEEE Transactions on Magnetics*, 44(6):1590–1593, 2008.

A. Kioumarsi, M. Moallem, and B. Fahimi. Mitigation of torque ripple in interior permanent magnet motors by optimal shape design. *IEEE Transactions on Magnetics*, 42(11):3706–3711, 2006.

C.-S. Koh, S.-Y. Hahn, K.-S. Lee, and K. Choi. Design sensitivity analysis for shape optimization of 3-D electromagnetic devices. *IEEE Transactions on Magnetics*, 29(2):1753–1757, 1993.

E. Kuci, F. Henrotte, P. Duysinx, and C. Geuzaine. Design sensitivity analysis for shape optimization based on the Lie derivative. *Computer Methods in Applied Mechanics and Engineering*, 317:702 – 722, 2017. ISSN 0045-7825.

A. Kumar and D. Gossard. Synthesis of optimal shape and topology of structures. *Journal of Mechanical Design*, 118(1):68–74, 1996.

J. Kwack, S. Min, and J.-P. Hong. Optimal stator design of interior permanent magnet motor to reduce torque ripple using the level set method. *IEEE Transactions on Magnetics*, 46(6):2108–2111, 2010.

N. H. K. Kyung K. Choi. *Structural Sensitivity Analysis and Optimization 1*. Springer Science & Business Media, Inc., 2005. ISBN 0-387-23232-X.

T. Labbé. *Topology optimization methods for the design of electromagnetic actuators*. PhD thesis, PhD thesis, department: electromechanic, Université catholique de Louvain, Ecole Polytechnique de Louvain, Belgique, 2011.

C. Le, J. Norato, T. Bruns, C. Ha, and D. Tortorelli. Stress-based topology optimization for continua. *Structural and Multidisciplinary Optimization*, 41 (4):605–620, 2010.

J. Lee and S. Wang. Topological shape optimization of permanent magnet in voice coil motor using level set method. *IEEE Transactions on Magnetics*, 48 (2):931–934, 2012.

J. Lee, J. H. Seo, and N. Kikuchi. Topology optimization of switched reluctance motors for the desired torque profile. *Structural and Multidisciplinary Optimization*, 42(5):783–796, 2010.

S. Lim, S. Min, and J.-P. Hong. Low torque ripple rotor design of the interior permanent magnet motor using the multi-phase level-set and phase-field concept. *IEEE Transactions on Magnetics*, 48(2):907–910, 2012.

C.-Y. Lin and L.-S. Chao. Automated image interpretation for integrated topology and shape optimization. *Structural and Multidisciplinary Optimization*, 20(2): 125–137, 2000.

B. Maar and V. Schulz. Interior point multigrid methods for topology optimization. *Structural and Multidisciplinary Optimization*, 19(3):214–224, 2000.

T. Matsumori, T. Kondoh, A. Kawamoto, and T. Nomura. Topology optimization for fluid–thermal interaction problems under constant input power. *Structural and Multidisciplinary Optimization*, 47(4):571–581, 2013.

M. K. Misztal, K. Erleben, A. Bargteil, J. Fursund, B. B. Christensen, J. A. Bærentzen, and R. Bridson. Multiphase flow of immiscible fluids on unstructured moving meshes. *IEEE Transactions on Visualization and Computer Graphics*, 20(1):4–16, 2014.

J. Nocedal. Updating quasi-newton matrices with limited storage. *Mathematics of computation*, 35(151):773–782, 1980.

J. Norato, R. Haber, D. Tortorelli, and M. P. Bendsøe. A geometry projection method for shape optimization. *International Journal for Numerical Methods in Engineering*, 60(14):2289–2312, 2004.

A. A. Novotny, R. A. Feijóo, E. Taroco, and C. Padra. Topological sensitivity analysis. *Computer methods in applied mechanics and engineering*, 192(7):803–829, 2003.

L. B. NS Khot and V. B. Venkayya. Comparison of optimality criteria algorithms for minimum weight design of structures. *AIAA Journal*, 17(2):182–190, 1979.

S. Oh, S. Min, and J.-P. Hong. Air gap flux density waveform design of surface-mounted permanent magnet motor considering magnet shape and magnetization direction. *IEEE Transactions on Magnetics*, 49(5):2393–2396, 2013.

T. Ohi, T. Horiguchi, T. Okuda, T. Kikunaga, and H. Matsumoto. Analysis and measurement of chip current imbalances caused by the structure of bus bars in an igbt module. In *Industry Applications Conference, 1999. Thirty-Fourth IAS Annual Meeting. Conference Record of the 1999 IEEE*, volume 3, pages 1775–1779. IEEE, 1999.

Y. Okamoto, M. Ohtake, and N. Takahashi. Magnetic shield design of perpendicular magnetic recording head by using topology optimization technique. *IEEE transactions on Magnetics*, 41(5):1788–1791, 2005.

N. Olhoff. Optimal design of vibrating circular plates. *International Journal of Solids and Structures*, 6(1):139–156, 1970.

N. Olhoff, M. P. Bendsøe, and J. Rasmussen. On CAD-integrated structural topology and design optimization. *Computer Methods in Applied Mechanics and Engineering*, 89(1-3):259–279, 1991.

C. E. Orozco and O. N. Ghattas. A reduced sand method for optimal design of non-linear structures. *International Journal for Numerical Methods in Engineering*, 40(15):2759–2774, 1997.

S. Osher and J. A. Sethian. Fronts propagating with curvature-dependent speed: algorithms based on hamilton-jacobi formulations. *Journal of computational physics*, 79(1):12–49, 1988.

I.-H. Park, J.-L. Coulomb, and S.-Y. Hahn. Implementation of continuum sensitivity analysis with existing finite element code. *IEEE Transactions on Magnetics*, 29(2):1787–1790, 1993.

R. Pasterczyk, C. Martin, J.-M. Guichon, and J.-L. Schanen. Planar busbar optimization regarding current sharing and stray inductance minimization. In *Power Electronics and Applications, 2005 European Conference on*, pages 9–pp. IEEE, 2005.

J. Petersson and O. Sigmund. Slope constrained topology optimization. *International Journal for Numerical Methods in Engineering*, 41(8):1417–1434, 1998.

W. Prager and J. Taylor. Problems of optima! structural design1. *Appl. Meeh. S*, 3:102, 1968.

O. Puigdellivol, Y. Le Menach, S. Harmand, D. Méresse, and J.-F. Wecxsteen. Multiphysics topology optimization for laminated busbars. In *Electromagnetic Field Computation (CEFC), 2016 IEEE Conference on*, pages 1–1. IEEE, 2016.

O. Puigdellivol, D. Méresse, Y. Le Menach, S. Harmand, and J.-F. Wecxsteen. Thermal topology optimization of a three-layer laminated busbar for power converters. *IEEE Transactions on Power Electronics*, 32(6):4691–4699, 2017.

Z. Qian and G. Ananthasuresh. Optimal embedding of rigid objects in the topology design of structures. *Mechanics Based Design of Structures and Machines*, 32 (2):165–193, 2004.

S. Rojas-Labanda and M. Stolpe. Benchmarking optimization solvers for structural topology optimization. *Structural and Multidisciplinary Optimization*, 52(3): 527–547, 2015.

G. Rozvany. Aims, scope, methods, history and unified terminology of computer-aided topology optimization in structural mechanics. *Structural and Multidisciplinary optimization*, 21(2):90–108, 2001.

G. Rozvany and M. Zhou. The coc algorithm, part i: cross-section optimization or sizing. *Computer Methods in Applied Mechanics and Engineering*, 89(1-3): 281–308, 1991.

G. I. Rozvany. A critical review of established methods of structural topology optimization. *Structural and multidisciplinary optimization*, 37(3):217–237, 2009.

K. Schittkowski. Nlpql: A fortran subroutine solving constrained nonlinear programming problems. *Annals of operations research*, 5(1):485–500, 1986.

L. Schmit and R. Fox. An integrated approach to structural synthesis and analysis. *AIAA JOURNAL*, 3(6), 1965.

L. A. Schmit. Structural design by systematic synthesis. In *Proceedings of the Second ASCE Conference on Electronic Computation*, pages 105–122, 1960.

L. A. Schmit and C. Fleury. Discrete-continuous variable structural synthesis using dual methods. *AIAA Journal*, 18(12):1515–1524, 1980.

O. Sigmund and K. Maute. Topology optimization approaches. *Structural and Multidisciplinary Optimization*, 48(6):1031–1055, 2013.

C. Silva and M. Bittencourt. Velocity fields using nurbs with distortion control for structural shape optimization. *Structural and Multidisciplinary Optimization*, 33(2):147–159, 2007.

E. N. Silva, J. O. Fonseca, and N. Kikuchi. Optimal design of piezoelectric microstructures. *Computational mechanics*, 19(5):397–410, 1997.

J. Sokolowski and J.-P. Zolesio. Introduction to shape optimization. In *Introduction to Shape Optimization*, pages 5–12. Springer, 1992.

J. Stegmann and E. Lund. Discrete material optimization of general composite shell structures. *International Journal for Numerical Methods in Engineering*, 62(14):2009–2027, 2005.

M. Stolpe and K. Svanberg. A note on stress-constrained truss topology optimization. *Structural and multidisciplinary optimization*, 25(1):62–64, 2003.

K. Svanberg. The method of moving asymptotes- a new method for structural optimization. *International journal for numerical methods in engineering*, 24 (2):359–373, 1987.

K. Svanberg. A globally convergent version of mma without linesearch. In *Proceedings of the first world congress of structural and multidisciplinary optimization*, volume 28, pages 9–16. Goslar, Germany, 1995.

K. Svanberg and M. Werme. Sequential integer programming methods for stress constrained topology optimization. *Structural and Multidisciplinary Optimization*, 34(4):277–299, 2007.

P.-S. Tang and K.-H. Chang. Integration of topology and shape optimization for design of structural components. *Structural and Multidisciplinary Optimization*, 22(1):65–82, 2001.

Z. Tang, P. Pillay, Y. Chen, and A. M. Omekanda. Prediction of electromagnetic forces and vibrations in srms operating at steady-state and transient speeds. *IEEE Transactions on Industry Applications*, 41(4):927–934, 2005.

N. P. van Dijk, K. Maute, M. Langelaar, and F. Van Keulen. Level-set methods for structural topology optimization: a review. *Structural and Multidisciplinary Optimization*, 48(3):437–472, 2013.

L. Van Miegroet and P. Duysinx. Stress concentration minimization of 2d filets using x-fem and level set description. *Structural and Multidisciplinary Optimization*, 33(4-5):425–438, 2007.

M. Y. Wang, X. Wang, and D. Guo. A level set method for structural topology optimization. *Computer methods in applied mechanics and engineering*, 192(1): 227–246, 2003.

S. Wang, J. Kang, and J. Noh. Topology optimization of a single-phase induction motor for rotary compressor. *IEEE Transactions on Magnetics*, 40(3):1591–1596, 2004.

S. Wang, K. Tai, and M. Y. Wang. An enhanced genetic algorithm for structural topology optimization. *International Journal for Numerical Methods in Engineering*, 65(1):18–44, 2006.

H. Wen and W. Xiao. Design and optimization of laminated busbar to reduce transient voltage spike. In *Industrial Electronics (ISIE), 2012 IEEE International Symposium on*, pages 1478–1483. IEEE, 2012.

R. Yang and M. Botkin. A modular approach for three-dimensional shape optimization of structures. *AIAA journal*, 25(3):492–497, 1987.

T.-M. Yao and K. K. Choi. 3-D shape optimal design and automatic finite element regridding. *International Journal for Numerical Methods in Engineering*, 28(2): 369–384, 1989.

J. Yoo, N. Kikuchi, and J. Volakis. Structural optimization in magnetic fields using the homogenization design method—part i. *Archives of Computational Methods in Engineering*, 8(4):387–406, 2001.

T. Zegard and G. H. Paulino. Bridging topology optimization and additive manufacturing. *Structural and Multidisciplinary Optimization*, 53(1):175–192, 2016.

J. Zhang, W. Zhang, J. Zhu, and L. Xia. Integrated layout design of multi-component systems using xfem and analytical sensitivity analysis. *Computer Methods in Applied Mechanics and Engineering*, 245:75–89, 2012.

S. Zhang and A. Belegundu. A systematic approach for generating velocity fields in shape optimization. *Structural and Multidisciplinary Optimization*, 5(1):84–94, 1992.

W. Zhang and Q. Zhang. Finite-circle method for component approximation and packing design optimization. *Engineering Optimization*, 41(10):971–987, 2009.

W. Zhang, L. Xia, J. Zhu, and Q. Zhang. Some recent advances in the integrated layout design of multicomponent systems. *Journal of Mechanical Design*, 133 (10):104503, 2011.

W.-H. Zhang, P. Beckers, and C. Fleury. A unified parametric design approach to structural shape optimization. *International Journal for Numerical Methods in Engineering*, 38(13):2283–2292, 1995.

J. Zhu, W. Zhang, and P. Beckers. Integrated layout design of multi-component system. *International journal for numerical methods in engineering*, 78(6):631–651, 2009.

O. Zienkiewicz and J. Campbell. Shape optimization and sequential linear programming. *Optimum structural design*, pages 109–126, 1973.

List of publications and communications

Papers in international journals

- Erin Kuci, François Henrotte, Pierre Duysinx, and Christophe Geuzaine. "Combination of Shape and Topology Optimization based on the Lie Derivative". In Structural and multidisciplinary optimization (2018). Submitted for publication.
- Erin Kuci, François Henrotte, Pierre Duysinx, and Christophe Geuzaine. "Three-dimensional Topology Optimization of a Planar Multilayer Busbar". In Structural and multidisciplinary optimization (2018). Submitted for publication.
- Erin Kuci, Christophe Geuzaine, and Pierre Duysinx. "Efficient iterative solver for MMA subproblems in topology optimization with stress constraints". In International Journal for Numerical Methods in Engineering (2017). Submitted for publication.
- Erin Kuci, François Henrotte, Pierre Duysinx, and Christophe Geuzaine. "Design sensitivity analysis for shape optimization based on the Lie derivative". In Computer Methods in Applied Mechanics and Engineering (2017), pp. 702–722, issn: 0045-7825.
- Erin Kuci, François Henrotte, Pierre Duysinx, Patrick Dular, and Christophe Geuzaine. "Design sensitivity analysis for shape optimization of nonlinear magnetostatic systems". In IEEE Transactions on Magnetics (2016), pp. 1–4.
- Erin Kuci, Christophe Geuzaine, Patrick Dular, and Pierre Duysinx. "Shape Optimization of Interior Permanent Magnet Motor for Torque Ripple Reduction". In Proceedings of the 4th International Conference on Engineering Optimization (2014), p. 187–193.

International conferences

- Erin Kuci, François Henrotte, Christophe Geuzaine, and Pierre Duysinx. "Shape and Topology Optimization of Electrical Machines using Lie Derivative-Based Analytical Sensitivity Analysis". Talk at the 12th World Congress of Structural and Multidisciplinary Optimisation (WCSMO12) – Braunschweig (Germany), 2017 (5 - 9 June).
- Erin Kuci, Jon Velasco, Pierre Duysinx, and Christophe Geuzaine. "Topology Optimization for Impedance Mismatch Reduction of a 3D Planar Multilayer Busbar". Talk at the 9eme Conference Européene sur les Methodes Numériques en Electromagnetisme (EMF 2016) – Paris (France), 2017 (15-17 November).
- Erin Kuci, Pierre Duysinx, and Christophe Geuzaine. "Shape and Topology Optimization of Electric Drives". Talk at the 10th International Symposium on Electric and Magnetic Fields (EMF 2016) – Lyon (France), 2016 (12-14 April).
- Erin Kuci, François Henrotte, Christophe Geuzaine, and Pierre Duysinx. "Shape and Topology Optimization of Electrical Machines using Lie Derivative-Based Analytical Sensitivity Analysis". Talk at the 17th Biennial Conference on Electromagnetic Field Computation (CEFC2016) – Miami (Florida), 2016 (13-16 November).
- Erin Kuci, Pierre Duysinx, Patrick Dular, and Christophe Geuzaine. "Design Sensitivity Analysis for Shape Optimization of Nonlinear Magnetostatic Systems". Poster at 20th International Conference on the Computation of Electromagnetic Fields (Compumag 2015) – Montreal (Canada), 2015 (28 June - 2 July).
- Erin Kuci, François Henrotte, Patrick Dular, Christophe Geuzaine, and Pierre Duysinx. "Direct and Adjoint Sensitivity Analysis of Nonlinear Magnetostatic System: Application to Shape Optimization of Electrical Machines". Talk at the 11th world congress of structural and multidisciplinary optimization (WCSMO11) – Sydney (Australia), 2015 (7-12 June).
- Erin Kuci, Christophe Geuzaine, Patrick Dular, and Pierre Duysinx. "Shape Optimization of Interior Permanent Magnet Motor for Torque Ripple Reduction". Talk at the 4th International Conference on Engineering Optimization (EngOpt 2014) – Lisbon (Portugal), 2014 (8-11 September).

Appendix

A

Paper I: Design sensitivity analysis for shape optimization based on the Lie derivative

Available online at www.sciencedirect.com
ScienceDirect
Comput. Methods Appl. Mech. Engrg. 317 (2017) 702–722
Computer methods in applied mechanics and engineering
www.elsevier.com/locate/cma

Design sensitivity analysis for shape optimization based on the Lie derivative

Erin Kuci[a,b,*], François Henrotte[b,c], Pierre Duysinx[a], Christophe Geuzaine[b]

[a] *University of Liège, Department of Aerospace and Mechanical Engineering, Belgium*
[b] *University of Liège, Department of Electrical Engineering and Computer Science, Belgium*
[c] *Université catholique de Louvain, EPL-iMMC-MEMA, Belgium*

Received 17 August 2016; received in revised form 25 December 2016; accepted 30 December 2016
Available online 11 January 2017

Highlights

- Framework for shape sensitivity analysis of systems governed by PDEs.
- Make use of differential geometry concepts.
- Applied to electromagnetic and elastic systems.
- Exactness proved by the finite difference approach.
- Convergence analysis in 2D and 3D, with first and second order finite elements.

A

Abstract

The paper presents a theoretical framework for the shape sensitivity analysis of systems governed by partial differential equations. The proposed approach, based on geometrical concepts borrowed from differential geometry, shows that sensitivity of a performance function (i.e. any function of the solution of the problem) with respect to a given design variable can be represented mathematically as a Lie derivative, i.e. the derivative of that performance function along a flow representing the continuous shape modification of the geometrical model induced by the variation of the considered design variable. Theoretical formulae to express sensitivity analytically are demonstrated in detail in the paper, and applied to a nonlinear magnetostatic and a linear elastic problem, following both the direct and the adjoint approaches. Following the analytical approach, one linear system of which only the right-hand side needs be evaluated (the system matrix being known already) has to be solved for each of the design variables in the direct approach, or for each performance functions in the adjoint approach. A substantial gain in computation time is obtained this way compared to a finite difference evaluation of sensitivity, which requires solving a second nonlinear system for each design variable. This is the main motivation of the analytical approach. There is some freedom in the definition of the auxiliary flow that represents the shape modification. We present a method that makes benefit of this freedom to express sensitivity locally as a volume integral over a single layer of finite elements connected to both sides of the surfaces undergoing shape modification. All sensitivity

* Corresponding author at: University of Liège, Department of Aerospace and Mechanical Engineering, Belgium.
E-mail address: Erin.Kuci@ulg.ac.be (E. Kuci).

http://dx.doi.org/10.1016/j.cma.2016.12.036

E. Kuci et al. / Comput. Methods Appl. Mech. Engrg. 317 (2017) 702–722 703

calculations are checked with a finite difference in order to validate the analytic approach. Convergence is analyzed in 2D and 3D, with first and second order finite elements.

Keywords: Lie derivative; Shape optimization; Velocity field; Elasticity; Magnetostatics

1. Introduction

Shape optimization has been an active research area since the seminal work of Zienkiewicz et al. in the early 1970s [1,2], which was aiming at determining the layout of a mechanical structure maximizing a performance measure under some design constraints. Shape optimization can however also be applied to systems governed by partial differential equations (PDEs), which introduces one extra level of difficulty. Methods for tackling such problems have been developed in the field of nonlinear mathematical programming since the early 1960s [3–6]. In the most successful approaches, the original problem is approximated by a sequence of convex optimization subproblems that are explicit in the design variables, and that can be minimized effectively by relying on the derivative of the performance functions, e.g. through an interior point method [7], or a dual Lagrange maximization [5].

In this context, the concept of sensitivity is pivotal. Two approaches have emerged over the years. The first one differentiates the discretized algebraic system [8], whereas the second one acts as an analytical differentiation at the level of the variational formulation of the problem [9]. Sensitivity analysis has been developed so far mostly in the area of structural mechanics [10–12,1,13–16]. Applications in other disciplines such as electromagnetics have also been proposed [17–19], but have been limited to problems expressed in terms of a scalar potential, leaving aside the problem of handling vector unknown fields, which requires a more general theoretical framework.

This generalized framework is the purpose of this paper. With the concept of Lie derivative [20–24], sensitivity is expressed analytically at the continuous level, prior to discretization. The Lie derivative is the derivative along a flow, and the flow considered here is a continuous modification of the geometrical domain as design variables variate. Several methods have been proposed to generate the velocity field of this flow, using either an isoparametric mapping [25–28], the boundary displacement method [29–31], or the fictitious load method [32,33]. In this paper, we propose a generic CAD-based mesh relocalization method for the computation of the velocity field, which is suited for shape optimization problems based on CAD representations and allows an efficient numerical implementation.

The paper is organized as follows. The optimization problem is posed in Section 2. Section 3 develops the theoretical aspects of sensitivity analysis based on differential geometry, and formulae to express Lie derivative practically are detailed in Section 4. Section 5 details the construction of the velocity field. In Sections 6 and 7, the general framework is used to derive analytical sensitivity formulae for various linear or nonlinear systems. The proposed approach is shown to give the same sensitivity formulae as [34] in the case of linear elastic problems, and to generalize to non-scalar fields the results established in [35,36] for nonlinear magnetostatics.

2. Optimization problem

Let us consider a bounded domain Ω whose regions are separated by interfaces $\gamma^{\boldsymbol{\tau}}$ undergoing shape modifications controlled by a set of design variables $\boldsymbol{\tau}$, Fig. 1. A physical problem is defined over Ω by a system of nonlinear PDEs expressed in terms of a state variable $\boldsymbol{z}$ and a design variable set $\boldsymbol{\tau}$. A weak formulation of this problem is obtained by, e.g., a Galerkin linearization approach, and can be written in a generic form

$$r(\boldsymbol{\tau}, \boldsymbol{z}^\star, \tilde{\boldsymbol{z}}) = 0, \ \forall \tilde{\boldsymbol{z}} \in Z_z^0, \tag{1}$$

with Z_z^0 an appropriate function space and $\boldsymbol{z}^\star$ the solution of the problem. The functional $r(\boldsymbol{\tau}, \boldsymbol{z}, \tilde{\boldsymbol{z}})$ is called residual and is always linear with respect to $\tilde{\boldsymbol{z}}$, i.e.

$$r(\boldsymbol{\tau}, \boldsymbol{z}, \boldsymbol{a} + \boldsymbol{b}) = r(\boldsymbol{\tau}, \boldsymbol{z}, \boldsymbol{a}) + r(\boldsymbol{\tau}, \boldsymbol{z}, \boldsymbol{b}).$$

The aim of a PDE-constrained shape optimization problem is to determine the geometric configuration $\boldsymbol{\tau}$ that minimizes a cost function $f_0(\boldsymbol{\tau}, \boldsymbol{z})$, subjected to m inequalities $f_j(\boldsymbol{\tau}, \boldsymbol{z}) \leq 0$, $j = 1, \ldots, m$, ensuring the

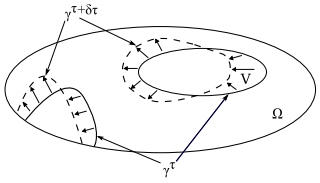

Fig. 1. Considered domain Ω for a PDE-constrained shape optimization problem (2), where an interface γ^{τ}, parametrized by a design variable τ, is deformed onto $\gamma^{\tau+\delta\tau}$ as the design variable is perturbed by a small amount $\delta\tau$. The perturbation of the γ^{τ} generates a velocity field $\mathbf{v}$.

manufacturability or the feasibility of the design. The design space is also limited by physical or technological side constraints $\tau_i^{min} \leq \tau_i \leq \tau_i^{max}$, $i = 1, \ldots, n$. Hence, the optimization problem reads

$$\begin{aligned} \min_{\boldsymbol{\tau}} \quad & f_0(\boldsymbol{\tau}, \boldsymbol{z}^\star) \\ s.t. \quad & f_j(\boldsymbol{\tau}, \boldsymbol{z}^\star) \leq 0, \ j = 1, \ldots, m \\ & \tau_i^{min} \leq \tau_i \leq \tau_i^{max}, \ i = 1, \ldots, n \\ & r(\boldsymbol{\tau}, \boldsymbol{z}^\star, \bar{\boldsymbol{z}}) = 0, \ \forall \bar{\boldsymbol{z}} \in Z_z^0. \end{aligned} \tag{2}$$

The evaluation of the performance functions f_0 and f_j for a given $\boldsymbol{\tau}$ requires the knowledge of $\boldsymbol{z}^\star$ for that particular value of $\boldsymbol{\tau}$, which implies solving anew the nonlinear physical problem (1). The repetition of these evaluations is time-consuming for large scale applications.

The sensitivity matrix of problem (2) is the matrix

$$S_{ji} = \frac{\mathrm{d}f_j}{\mathrm{d}\tau_i}(\boldsymbol{\tau}, \boldsymbol{z}^\star) \tag{3}$$

of the derivatives of the performance functions with respect to the design variables. Optimization algorithms that do not rely on the sensitivity matrix necessitate a large number of function evaluations, and are therefore inefficient. Sensitivity-based algorithms, also often called gradient-based algorithms, on the other hand, offer a higher convergence rate, lesser function evaluations, and hence, in our case, limit the required number of resolutions of the finite element physical problem. In this article, a mathematical programming algorithm is used, coupled with a finite element analysis code [37,38]. The optimization problem (2) is approximated by a series of convex subproblems explicit in the design variables, such as CONLIN [39] or MMA [40], which are then solved efficiently by a gradient-based primal, dual, or even combined primal–dual approach.

A

3. Design sensitivity analysis

We shall, for the sake of simplicity, consider one particular performance function, noted $f(\tau, \boldsymbol{z}^\star)$, and one particular design variable, noted τ. This amounts to deal with one particular component of the sensitivity matrix (3). The treatment of any other component would be identical.

3.1. Finite difference

The most straightforward approach approximates sensitivity with a simple finite difference [16]

$$\frac{\mathrm{d}f}{\mathrm{d}\tau}(\tau, \boldsymbol{z}^\star) \approx \frac{f\left(\tau + \delta\tau, \boldsymbol{z}^\dagger\right) - f\left(\tau, \boldsymbol{z}^\star\right)}{\delta\tau}, \tag{4}$$

where $\delta\tau$ is a small perturbation of the design variable. This evaluation requires solving two nonlinear problems on slightly different geometries to evaluate $\boldsymbol{z}^\star$ and $\boldsymbol{z}^\dagger$,

$$\begin{aligned} r(\tau, \boldsymbol{z}^\star, \bar{\boldsymbol{z}}) &= 0, \ \forall \bar{\boldsymbol{z}} \in Z_z^0, \\ r(\tau + \delta\tau, \boldsymbol{z}^\dagger, \bar{\boldsymbol{z}}) &= 0, \ \forall \bar{\boldsymbol{z}} \in Z_z^0, \end{aligned}$$

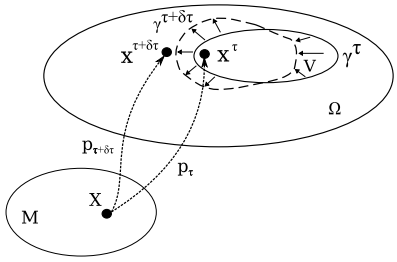

Fig. 2. Considered material manifold M and Euclidean space Ω where the physical problem (1) is defined. Each geometrical configuration of Ω is characterized by an instance of the design variable τ, and represented by a smooth mapping p_τ (placement map) of each point $X \in M$ to each point $x^\tau \in \Omega$.

of which only the first one is necessary and must be done in any case. The cost of the second one is indeed prohibitive considered that the sought sensitivity pertains to the linearization of the problem in the configuration corresponding to τ and $\mathbf{z}^\star$, and that this linearization has been done already to solve the first nonlinear problem. The finite difference approach is thus simple, but slow, and it is essentially used for validation purpose.

3.2. Analytical expression of sensitivity

It is more efficient to express the derivative of f with respect to τ analytically at a continuous level, prior to discretization. Writing the performance function explicitly in the form of an integral[1]

$$f(\tau, \mathbf{z}^\star) = \int_{\Omega(\tau)} F(\tau, \mathbf{z}^\star)\, \mathrm{d}\Omega, \tag{5}$$

sensitivity is the derivative with respect to τ of this integral and, in order to obtain an analytical expression, one has to be able to perform the differentiation under the integral sign.

The definition of the Lie derivative involves in this context a one parameter family of mappings

$$p_{\delta\tau} : \Omega(\tau) \subset E^3 \mapsto \Omega(\tau + \delta\tau) \subset E^3 \tag{6}$$

describing a smooth geometrical transformation of Ω in the Euclidean space E^3, with no tearing nor overlapping, that brings the interfaces between regions from their position γ^τ to their position $\gamma^{\tau+\delta\tau}$, Fig. 2. The mappings (6) with the scalar parameter $\delta\tau$ taking values in a neighborhood of zero and playing the role of a pseudo time variable, determines a flow on E^3 whose velocity field is noted $\mathbf{v}$. This velocity field plays a central role in the evaluation of the Lie derivative. An automatic procedure to build it in the general case is described in Section 5.

As the mappings (6) are invertible for all $\delta\tau$, tensor quantities (i.e. scalar fields, vector fields, or tensor fields) can be mapped back from $\Omega(\tau + \delta\tau)$ into $\Omega(\tau)$ using the inverse $p_{\delta\tau}^{-1}$ of $p_{\delta\tau}$. The Lie derivative of an arbitrary field ω in $\Omega(\tau)$ is then defined as

$$L_{\mathbf{v}}\omega = \lim_{\delta\tau \to 0} \frac{p_{\delta\tau}^{-1}\omega - \omega}{\delta\tau}, \tag{7}$$

where the index $\mathbf{v}$ in the notation $L_{\mathbf{v}}\omega$ makes reference to the velocity field characterizing the flow.

The Lie derivative is the mathematical concept describing the differentiation of an integral quantity over a deforming domain and verifies by definition the fundamental property

$$\frac{\mathrm{d}}{\mathrm{d}\tau} \int_{\Omega(\tau)} \omega = \int_{\Omega(\tau)} L_{\mathbf{v}}\omega. \tag{8}$$

Its properties and formulae to evaluate it practically are detailed in Section 4.

[1] If the performance function is a pointwise value, the expression of $F(\tau, \mathbf{z}^\star)$ will then involve a Dirac function.

A

In particular, for the performance function (5) one can thus write

$$\frac{\mathrm{d}f}{\mathrm{d}\tau}(\tau, z^\star) = \int_{\Omega(\tau)} L_{\mathbf{v}} F(\tau, z^\star) \mathrm{d}\Omega. \tag{9}$$

By the chain rule of derivatives, the Lie derivative of the functional $F(\tau, z^\star)$ has got two terms

$$L_{\mathbf{v}} F(\tau, z^\star) = L_{\mathbf{v}} F(\tau, z^\star)\Big|_{L_{\mathbf{v}} z = 0} + \big\{\mathrm{D}_z F(\tau, z^\star)\big\}\big(L_{\mathbf{v}} z^\star\big). \tag{10}$$

The first term is the partial Lie derivative of the functional, defined as the Lie derivative holding the field argument z constant

$$D_\tau F(\tau, z^\star) = L_{\mathbf{v}} F(\tau, z^\star)\Big|_{L_{\mathbf{v}} z = 0}. \tag{11}$$

It accounts for changes in the value of the functional unrelated to the variation of the field. The second term involves the Fréchet derivative of the functional $F(\tau, z)$ with respect to its field argument z. The Fréchet derivative is the linear operator $\big\{\mathrm{D}_z F(\tau, z)\big\}(\cdot)$ defined by

$$\lim_{|\delta z| \to 0} \frac{1}{|\delta z|} \Big| F(\tau, z + \delta z) - F(\tau, z) - \big\{\mathrm{D}_z F(\tau, z)\big\}(\delta z) \Big| = 0, \tag{12}$$

where the limit is taken over all sequences of non-zero δz that converge to zero. The arguments between parenthesis inside the curly braces indicate where the operator is evaluated, whereas the argument in between parenthesis outside the curly braces indicates to what the operator is applied. If the functional has several field arguments, a Fréchet derivative can be defined similarly for each of them.

3.3. Direct approach

We have shown in the previous section that sensitivity is expressed analytically

$$\frac{\mathrm{d}f}{\mathrm{d}\tau}(\tau, z^\star) = \int_{\Omega(\tau)} \Big(D_\tau F(\tau, z^\star) + \big\{\mathrm{D}_z F(\tau, z^\star)\big\}\big(L_{\mathbf{v}} z^\star\big) \Big) \mathrm{d}\Omega \tag{13}$$

in terms of $L_{\mathbf{v}} z^\star$, which represents the evolution of the solution $z^\star$ of the physical problem as the design parameter τ is changing. In order to determine this quantity, one states that the derivative of the residual (1) with respect to τ is zero in $z^\star$,

$$\frac{\mathrm{d}}{\mathrm{d}\tau} r(\boldsymbol{\tau}, z^\star, \bar{z}) = 0, \ \forall \bar{z} \in Z_z^0. \tag{14}$$

As the residual is an integral of the form

$$r(\tau, z^\star, \bar{z}) = \int_{\Omega(\tau)} R(\tau, z^\star, \bar{z}) \mathrm{d}\Omega, \tag{15}$$

the condition (14) is again the derivative of an integral. It can be treated in a similar fashion as the derivative of the performance function. By the chain rule of derivatives, one has

$$\frac{\mathrm{d}}{\mathrm{d}\tau} r(\tau, z^\star, \bar{z}) = \int_{\Omega(\tau)} \Big(D_\tau R(\tau, z^\star, \bar{z}) + \big\{\mathrm{D}_z R(\tau, z^\star, \bar{z})\big\}\big(L_{\mathbf{v}} z^\star\big) + \big\{\mathrm{D}_{\bar{z}} R(\tau, z^\star, \bar{z})\big\}\big(L_{\mathbf{v}} \bar{z}\big) \Big) \mathrm{d}\Omega. \tag{16}$$

The last term in the right-hand side of (16) vanishes, because linearity of $r(\tau, z^\star, \bar{z})$ with respect to its argument $\bar{z}$ implies

$$\begin{aligned} &\lim_{|\delta \bar{z}| \to 0} \frac{1}{|\delta \bar{z}|} \Big| R(\tau, z, \bar{z} + \delta \bar{z}) - R(\tau, z, \bar{z}) - \big\{\mathrm{D}_{\bar{z}} R(\tau, z, \bar{z})\big\}(\delta \bar{z}) \Big| \\ &\quad = \lim_{|\delta \bar{z}| \to 0} \frac{1}{|\delta \bar{z}|} \Big| R(\tau, z, \delta \bar{z}) - \big\{\mathrm{D}_{\bar{z}} R(\tau, z, \bar{z})\big\}(\delta \bar{z}) \Big| = 0. \end{aligned}$$

Hence the identity

$$\{\mathrm{D}_z R(\tau, z, \bar{z})\}(\delta\bar{z}) = R(\tau, z, \delta\bar{z}), \tag{17}$$

and in particular, for $z = z^\star$, $\delta\bar{z} = L_\mathbf{v}\bar{z}$ and using (1),

$$\int_{\Omega(\tau)} \{\mathrm{D}_z R(\tau, z^\star, \bar{z})\}(L_\mathbf{v}\bar{z})\mathrm{d}\Omega = r(\tau, z^\star, L_\mathbf{v}\bar{z}) = 0. \tag{18}$$

The left-hand side of (16) being zero, one has finally

$$\int_{\Omega(\tau)} \Big(D_\tau R(\tau, z^\star, \bar{z}) + \{\mathrm{D}_z R(\tau, z^\star, \bar{z})\}(L_\mathbf{v} z^\star)\Big)\mathrm{d}\Omega = 0, \ \forall \bar{z} \in Z_z^0, \tag{19}$$

which is the sought weak form of a linear problem allowing to solve for $L_\mathbf{v} z^\star$.

The Fréchet derivative term in (19) involves the tangent stiffness matrix of the nonlinear problem (1), and hence, in practice, the jacobian matrix of the problem after finite element discretization and convergence of the iterative nonlinear process. This term is therefore already known from the finite element solving, and needs not be recomputed when solving (19). The partial Lie derivative in (19) accounts for the explicit dependency (i.e. holding the field argument constant) of the residual on the variation of τ. It is the right-hand side of the system determining $L_\mathbf{v} z^\star$, which can also be evaluated analytically. The *semi-analytic approach* [41], however, consists in evaluating this term by a finite difference. Finite difference is done at a moderate numerical cost here, as $z^\star$ is already known and $z^\dagger$ is not needed.

3.4. Adjoint approach

An alternative to the method of previous section that solves explicitly for $L_\mathbf{v} z^\star$ is the adjoint approach. The idea is to define an auxiliary performance function, called augmented Lagrangian function,

$$\bar{f}(\tau, z, \boldsymbol{\lambda}) = f(\tau, z) - r(\tau, z, \boldsymbol{\lambda}) = \int_{\Omega(\tau)} \Big(F(\tau, z^\star) - R(\tau, z^\star, \boldsymbol{\lambda})\Big)\mathrm{d}\Omega, \tag{20}$$

with $\boldsymbol{\lambda}$ a Lagrange multiplier. As (1) implies that the residual $r(\tau, z^\star, \lambda)$ is zero at equilibrium, one has

$$\bar{f}(\tau, z^\star, \boldsymbol{\lambda}) = f(\tau, z^\star), \tag{21}$$

and the sensitivity is expressed in terms of the auxiliary performance function $\bar{f}$ by

$$\frac{\mathrm{d}f}{\mathrm{d}\tau}(\tau, z^\star) = \frac{\mathrm{d}\bar{f}}{\mathrm{d}\tau}(\tau, z^\star, \boldsymbol{\lambda}). \tag{22}$$

Differentiation of (20) with respect to τ yields

$$\begin{aligned}\frac{\mathrm{d}\bar{f}}{\mathrm{d}\tau}(\tau, z^\star, \boldsymbol{\lambda}) = \int_{\Omega(\tau)} \Big(&D_\tau F(\tau, z^\star) - D_\tau R(\tau, z^\star, \boldsymbol{\lambda}) \\ &+ \{\mathrm{D}_z F(\tau, z^\star)\}(L_\mathbf{v} z^\star) - \{\mathrm{D}_z R(\tau, z^\star, \boldsymbol{\lambda})\}(L_\mathbf{v} z^\star)\Big)\mathrm{d}\Omega,\end{aligned} \tag{23}$$

where we have already omitted the null term (18).

Let now $\boldsymbol{\lambda}^\star$ be the solution of the so-called adjoint problem

$$\int_{\Omega(\tau)} \Big(\{\mathrm{D}_z F(\tau, z^\star)\}(\bar{\lambda}) - \{\mathrm{D}_z R(\tau, z^\star, \boldsymbol{\lambda}^\star)\}(\bar{\lambda})\Big)\mathrm{d}\Omega = 0, \ \forall \bar{\lambda} \in Z_{\boldsymbol{\lambda}}. \tag{24}$$

As (24) holds for $\bar{\lambda} = L_\mathbf{v} z^\star \in Z_{\boldsymbol{\lambda}}$, and has the identity

$$\int_{\Omega(\tau)} \Big(\{\mathrm{D}_z F(\tau, z^\star)\}(L_\mathbf{v} z^\star) - \{\mathrm{D}_z R(\tau, z^\star, \boldsymbol{\lambda}^\star)\}(L_\mathbf{v} z^\star)\Big)\mathrm{d}\Omega = 0, \tag{25}$$

and the last two terms in the right-hand side of (23) cancel out each other if $\boldsymbol{\lambda} = \boldsymbol{\lambda}^\star$. Sensitivity is then given by

$$\frac{\mathrm{d}\bar{f}}{\mathrm{d}\tau}(\tau, \boldsymbol{z}^\star, \boldsymbol{\lambda}^\star) = \int_{\Omega(\tau)} \Big(D_\tau F(\tau, \boldsymbol{z}^\star) - D_\tau R(\tau, \boldsymbol{z}^\star, \boldsymbol{\lambda}) \Big) \mathrm{d}\Omega, \tag{26}$$

in terms of the solutions of the nonlinear problem (1) and of the adjoint problem (24).

The system matrix of adjoint problem (24) is again the tangent stiffness matrix of the nonlinear problem (1), i.e. the jacobian matrix after finite element discretization and convergence of the iterative nonlinear process. It can be reused if the same discretization is used for solving (24) and (1).

3.5. Discussion

The direct and the adjoint methods are now compared to determine in which conditions one has to favor one over the other.

Assuming a discretization $\boldsymbol{z} = \sum_{p=1}^{N} z_p \boldsymbol{w}_p$ of the unknown field, with basis functions $\boldsymbol{w}_p \in Z_z^0$ and N the number of nodal unknowns, one solves with the direct method the linear problem (19), which is of the form

$$\sum_{q=1}^{N} J_{pq}^\star \, x_q = b_p, \tag{27}$$

with

$$J_{pq}^\star = \big\{ \mathrm{D}_z R(\tau, \boldsymbol{z}^\star, \boldsymbol{w}_p) \big\} (\boldsymbol{w}_q) \tag{28}$$

the component of the nonlinear physical problem (1) jacobian matrix, and

$$b_p = D_\tau R(\tau, \boldsymbol{z}^\star, \boldsymbol{w}_p) \tag{29}$$

the fictitious load proper to the design variable τ, representing the partial Lie derivative of the residual associated with the test function $\bar{\boldsymbol{z}} \equiv \boldsymbol{w}_p$. One has a vector b_p for each design variable τ, and thus n linear systems like (27) to solve in a system with n design variables. Both $J_{pq}^\star$ and b_p are evaluated for $\boldsymbol{z} = \boldsymbol{z}^\star$, i.e., for the converged solution of the nonlinear iterative process. The matrix $J_{pq}^\star$ is thus known from the solving of (1) and needs not be recomputed.

The solution of (27), which is the field $\sum_{p=1}^{N} x_p \boldsymbol{w}_p \equiv L_{\boldsymbol{v}} \boldsymbol{z}^\star$, is a discrete estimation of the derivative of the solution $\boldsymbol{z}^\star$ of (1) with respect to the design variable τ or, put in a more accurate way, of the Lie derivative of $\boldsymbol{z}^\star$ along the flow associated with the variation of τ. This field is exactly what is needed to evaluate the sensitivity of the performance function with respect to τ

$$\frac{\mathrm{d}f}{\mathrm{d}\tau}(\tau, \boldsymbol{z}^\star) = \int_{\Omega(\tau)} \Big(D_\tau F(\tau, \boldsymbol{z}^\star) + \big\{ \mathrm{D}_z F(\tau, \boldsymbol{z}^\star) \big\} (x_p \boldsymbol{w}_p) \Big) \mathrm{d}\Omega, \tag{30}$$

since the performance function f being known (5), its Fréchet derivative $\mathrm{D}_z F$ and its partial Lie derivative $D_\tau F$ can both be expressed analytically.

With the adjoint approach, a system like (27) is also solved, with $J_{pq}^\star$ again given by (28), and

$$b_p = \big\{ \mathrm{D}_z F(\tau, \boldsymbol{z}^\star) \big\} (\boldsymbol{w}_p) \tag{31}$$

the adjoint load proper to the performance function f. The solution of the system, $\sum_{p=1}^{N} x_p \boldsymbol{w}_p \equiv \boldsymbol{\lambda}^\star \in Z_{\boldsymbol{\lambda}}$, is now the so-called adjoint field, in terms of which the sensitivity of the performance function with respect to τ is expressed as

$$\frac{\mathrm{d}f}{\mathrm{d}\tau}(\tau, \boldsymbol{z}^\star) = \int_{\Omega(\tau)} \Big(D_\tau F(\tau, \boldsymbol{z}^\star) - D_\tau R(\tau, \boldsymbol{z}^\star, \boldsymbol{\lambda}) \Big) \mathrm{d}\Omega. \tag{32}$$

The first term is identical to that in (30), and the second term implies an evaluation of the partial Lie derivative of the residual of the problem (1) with the adjoint field $\boldsymbol{\lambda}^\star$ as test function $\bar{\boldsymbol{z}}$. One has also a vector b_p for each performance function f, and thus m linear systems like (27) to solve in a system with m performance functions.

A

Both the direct and the adjoint approaches require solving the nonlinear system (1), in order to determine the solution $z^\star$ corresponding to the selected design variables $\boldsymbol{\tau}$. One has then to solve one linear system for each of the n design variables in the direct approach, or alternatively one linear system for each of the m performance functions in the adjoint approach. This is in both cases a clear performance advantage compared to the finite difference approach, for which a nonlinear problem like (1) has to be solved for each design variable. The direct method should be preferred when the number of performance functions exceeds the number of design variables, $m > n$, otherwise the adjoint method is preferable.

4. Lie derivative formula sheet

Lie derivatives are playing an important role in the analytical expression of sensitivity. We now present formulae to evaluate the Lie derivative of scalar, vector and tensor fields. The purpose of this paper is however not to give a complete mathematical derivation of this, but rather to provide engineers and practitioners in the field of optimization with a useful formula sheet. We therefore stick with standard vector and tensor analysis notations and give a number of results without proof.

The Lie derivative verifies the Leibniz rule for scalar fields

$$L_{\mathbf{v}}(fg) = (L_{\mathbf{v}}f)g + f(L_{\mathbf{v}}g), \tag{33}$$

vector fields

$$L_{\mathbf{v}}(\boldsymbol{F}\cdot\boldsymbol{G}) = (L_{\mathbf{v}}\boldsymbol{F})\cdot\boldsymbol{G} + \boldsymbol{F}\cdot(L_{\mathbf{v}}\boldsymbol{G}), \tag{34}$$

and tensor fields

$$L_{\mathbf{v}}(A : B) = (L_{\mathbf{v}}A) : B + A : (L_{\mathbf{v}}B), \tag{35}$$

where the colon : stands for the tensor product, $A : B = A_{ij}B_{ij}$ (implicit summation assumed on repeated indices in all the paper).

The Lie derivative of a scalar function f is

$$L_{\mathbf{v}}f = \frac{\partial f}{\partial \tau} + \mathbf{v}^T\nabla f, \tag{36}$$

with $\mathbf{v}$ the velocity field characterizing the flow. This is the classical expression for the convective derivative of a scalar quantity.

The Lie derivative of vector fields is more delicate. There exist several geometrical objects that have three components in an Euclidean space, but behaving differently under transformations like (6). Besides genuine vector fields, which convey the idea of motion and trajectory (e.g. the velocity $\mathbf{v}$ or displacement $\boldsymbol{u}$ fields), we have to deal with circulation densities (also called 1-forms), which are quantities that make sense when integrated over a curve, and whose tangential component is continuous at material interfaces (e.g. the magnetic vector potential $\boldsymbol{A}$ or the magnetic field $\boldsymbol{H}$) and flux densities (2-forms), which are quantities that make sense when integrated over a surface, and whose normal component is continuous at material interfaces (e.g. the flux density $\boldsymbol{B}$ and the current density $\boldsymbol{J}$). Although genuine vector fields, circulation densities and flux densities can be indiscriminately regarded as vector fields in an Euclidean space, their Lie derivatives are different under the transformation (6) and they must therefore be carefully distinguished when evaluating the Lie derivative of an expression involving such objects. The Lie derivative of a vector field $\boldsymbol{W} = W_i\boldsymbol{e}_i$ reads

$$L_{\mathbf{v}}\boldsymbol{W} = (L_{\mathbf{v}}W_i)\boldsymbol{e}_i - (\nabla\mathbf{v})^T\boldsymbol{W}, \tag{37}$$

whereas that of a 1-form $\boldsymbol{H} = H_i\boldsymbol{e}_i$ reads

$$L_{\mathbf{v}}\boldsymbol{H} = (L_{\mathbf{v}}H_i)\boldsymbol{e}_i + (\nabla\mathbf{v})\boldsymbol{H}, \tag{38}$$

and that of a 2-form $\boldsymbol{B} = B_i\boldsymbol{e}_i$

$$L_{\mathbf{v}}\boldsymbol{B} = (L_{\mathbf{v}}B_i)\boldsymbol{e}_i - (\nabla\mathbf{v})^T\boldsymbol{B} + \boldsymbol{B}\,\mathrm{div}\,\mathbf{v} \tag{39}$$

in an orthonormal basis $\{\boldsymbol{e}_i, i = 1, 2, 3\}$ and with the notations

$$
\begin{aligned}
(\nabla \mathbf{v}) &= (\nabla \mathbf{v})_{kj}\, \boldsymbol{e}_k \boldsymbol{e}_j^T = \frac{\partial V_j}{\partial x_k}\, \boldsymbol{e}_k \boldsymbol{e}_j^T \\
(\nabla \mathbf{v})^T &= \frac{\partial V_j}{\partial x_k}\, \boldsymbol{e}_j \boldsymbol{e}_k^T \\
(\nabla \mathbf{v})\boldsymbol{e}_i &= \frac{\partial V_i}{\partial x_k}\, \boldsymbol{e}_k \\
(\nabla \mathbf{v})^T \boldsymbol{e}_i &= \frac{\partial V_j}{\partial x_i}\, \boldsymbol{e}_j \\
(\nabla \mathbf{v})\boldsymbol{F} &= \frac{\partial V_i}{\partial x_k} F_i\, \boldsymbol{e}_k \\
(\nabla \mathbf{v})^T \boldsymbol{F} &= \frac{\partial V_j}{\partial x_i} F_i\, \boldsymbol{e}_j \\
\operatorname{div} \mathbf{v} &= \partial V_i / \partial x_i = \operatorname{tr}(\nabla \mathbf{v}) \\
A : B &= A_{ij} B_{ij} \\
\boldsymbol{e}_i \boldsymbol{e}_j^T : \boldsymbol{e}_p \boldsymbol{e}_q^T &= \delta_{ip} \delta_{jq}.
\end{aligned}
$$

We shall only use (38) and (39) in the expression of sensitivity.

The Lie derivative of a material law like $\boldsymbol{H}(\boldsymbol{B})$ is the Lie derivative of a functional (a function of a field quantity) instead of the derivative of a field. It is treated as follows. First, the material law must be regarded as a relationship between the components of the fields

$$
H_i(B_k) = \nu_{ij} B_j, \tag{40}
$$

with ν_{ij} the components of the nonlinear reluctivity tensor of the material. Taking the Lie derivative yields

$$
\begin{aligned}
L_{\mathbf{v}} H_i(B_k) &= \nu_{ij}\, L_{\mathbf{v}} B_j + \frac{\partial \nu_{ij}}{\partial B_k} B_j\, L_{\mathbf{v}} B_k + D_\tau H_i(B_k) \\
&= \nu^{\partial}_{ik}\, L_{\mathbf{v}} B_k + D_\tau H_i(B_k),
\end{aligned}
$$

with

$$
\nu^{\partial}(B_k) = \nu^{\partial}_{ik}\, \boldsymbol{e}_i \boldsymbol{e}_k^T = \Big(\nu_{ik} + \frac{\partial \nu_{ij}}{\partial B_k} B_j\Big) \boldsymbol{e}_i \boldsymbol{e}_k^T \tag{41}
$$

the components of the tangent reluctivity tensor of the material. The partial Lie derivative $D_\tau H_i(B_k)$ would represent a variation of the magnetic field components H_i under a change of τ, that would not be due to a variation of the field components B_k. This term accounts thus for a possible explicit dependency of the material law in the design variable τ and the geometrical changes associated to it, independently of the field argument dependency. There is no such dependency in general. The transformations (6) move indeed the interfaces γ^τ but leave by definition material laws unchanged, so that one has

$$
D_\tau H_i(B_k) = 0. \tag{42}
$$

We can now write successively

$$
\begin{aligned}
L_{\mathbf{v}} H_i(B_k)\, \boldsymbol{e}_i &= \nu^{\partial}_{ik}\, L_{\mathbf{v}} B_k\, \boldsymbol{e}_i \\
&= \nu^{\partial}_{ij}\, L_{\mathbf{v}} B_k\, \boldsymbol{e}_i \boldsymbol{e}_j^T \boldsymbol{e}_k \\
&= \nu^{\partial}_{ij}\, \boldsymbol{e}_i \boldsymbol{e}_j^T\, L_{\mathbf{v}} B_k\, \boldsymbol{e}_k \\
&= \{\nu^{\partial}(B_k)\}(L_{\mathbf{v}} B_k\, \boldsymbol{e}_k)
\end{aligned}
$$

where $\boldsymbol{e}_j^T \boldsymbol{e}_k = \delta_{jk}$ has been used. At the last line, the tangent reluctivity tensor has been written as an operator acting on the vector (actually a 2-form) $L_{\mathbf{v}} B_k\, \boldsymbol{e}_k$.

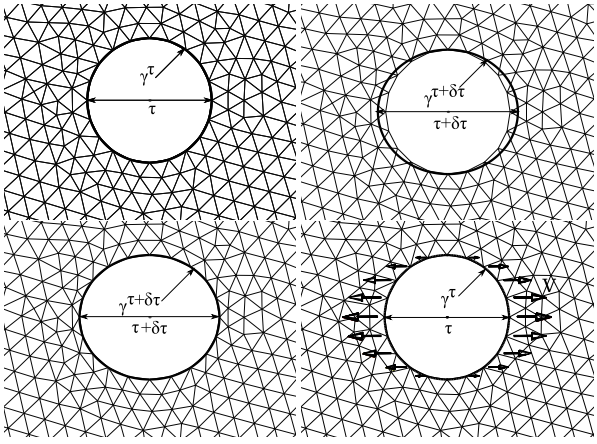

Fig. 3. A plate with an elliptic hole γ^τ is considered. The design variable τ is the major axis of the ellipse. After a finite perturbation $\delta\tau$, the mesh nodes lying on the surface γ^τ are relocalized on $\gamma^{\tau+\delta\tau}$ thanks to the CAD parametrization of the surface. The velocity field (46) is approximated by finite difference of the node positions before and after the perturbation.

The vectors $L_{\mathbf{v}}H_i(B_k)\,\boldsymbol{e}_i$ and $L_{\mathbf{v}}B_k\,\boldsymbol{e}_k$ can now be expressed in terms of $L_{\mathbf{v}}\boldsymbol{H}(\boldsymbol{B})$ and $L_{\mathbf{v}}\boldsymbol{B}$ using (38) and (39) to obtain

$$L_{\mathbf{v}}\boldsymbol{H}(\boldsymbol{B}) - (\nabla\mathbf{v})\,\boldsymbol{H}(\boldsymbol{B}) = \{\nu^\partial(B_k)\}\big(L_{\mathbf{v}}\boldsymbol{B} + (\nabla\mathbf{v})^T\boldsymbol{B} - \boldsymbol{B}\,\mathrm{div}\,\mathbf{v}\big). \tag{43}$$

Similarly, one has for inverse material law $\boldsymbol{B}(\boldsymbol{H})$

$$L_{\mathbf{v}}\boldsymbol{B}(\boldsymbol{H}) + (\nabla\mathbf{v})^T\boldsymbol{B}(\boldsymbol{H}) - \boldsymbol{B}(\boldsymbol{H})\,\mathrm{div}\,\mathbf{v} = \{\mu^\partial(H_k)\}\big(L_{\mathbf{v}}\boldsymbol{H} - (\nabla\mathbf{v})\boldsymbol{H}\big), \tag{44}$$

with $\mu^\partial = (\nu^\partial)^{-1}$.

5. Design velocity field computation

There is some freedom in the definition of the mappings (6), and, hence in the choice of an auxiliary flow with velocity $\mathbf{v}$, that represents the shape modification. Once the flow is chosen, the mathematical expression of the velocity field is the Lie derivative

$$\mathbf{v} = L_{\mathbf{v}}\boldsymbol{x}, \tag{45}$$

of the coordinate vector $\boldsymbol{x} = (x, y, z)$, where $\{x, y, z\}$ are coordinates on E^3.

Various methods for the automatic generation of (45) have been proposed in the literature, using either a geometrical constructive approach such as the isoparametric mapping [25–28], or an auxiliary structure, such as the boundary displacement method [29–31] or the fictitious load method [32,33]. In our approach, which belongs to the first category, we propose a generic computer-aided design (CAD) based method in which mesh nodes are relocalized on perturbed geometrical surfaces thanks to their CAD parametric coordinates [37]. The procedure is illustrated in Fig. 3 for a simple plate with an elliptic hole γ^τ, the considered design variable τ being the major axis of the ellipse. The CAD corresponding to the initial value τ is first meshed, so that the coordinates $\boldsymbol{x}^\tau$ of all nodes in that initial situation are known. The design variable τ is then modified by a small amount $\delta\tau$, leading to a slightly perturbed CAD, and in particular a perturbed surface $\gamma^{\tau+\delta\tau}$, Fig. 3. Mesh nodes lying on γ^τ with coordinates $\boldsymbol{x}^\tau$ can then be

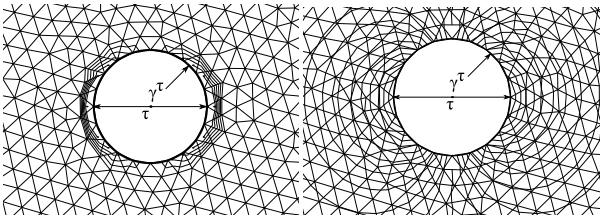

Fig. 4. The velocity field (46) so far computed for the mesh nodes lying in the elliptic surface γ^τ, is extended into either a one element thick layer on both sides of the surface γ^τ using the EL method (left), or in the whole domain using a LaS method (right).

relocalized on $\gamma^{\tau+\delta\tau}$ thanks to their parametric coordinates. If $\boldsymbol{x}^{\tau+\delta\tau}$ represent the relocalized coordinates, a discrete approximation of the vector field (45) is given by the finite difference

$$\mathbf{v} \approx \frac{\boldsymbol{x}^{\tau+\delta\tau} - \boldsymbol{x}^{\tau}}{\delta\tau}, \tag{46}$$

at all nodes on the surface γ^τ.

We however need the velocity field over the whole simulation domain Ω. It is thus extended from the surface γ^τ into Ω by one of the following two methods:

- Laplacian smoothing (LaS) [42]: the velocity field at inner nodes is obtained by solving a scalar Laplace equation for each component of the velocity field, with Dirichlet boundary conditions equal to (46) on γ^τ, and to zero on all other surfaces of the geometrical model. The x-component of the velocity field is illustrated in Fig. 4.
- Element layer (EL) extension: the velocity field is simply interpolated with the nodal shape functions of the initial mesh, assuming nodal values given by (46) at nodes on γ^τ, and equal to zero otherwise. The support of this velocity field is thus limited to a one element thick layer on both sides of the surface γ^τ. The x-component of the velocity field for the same example as above is illustrated in Fig. 4.

A

Comparative convergence [43] diagrams are presented in Fig. 5. The sensitivity of a performance function is computed with first order finite elements for various perturbation step $\delta\tau$ and mesh refinement. It is observed that perturbation steps $\delta\tau$ between 10^{-3} and 10^{-10} are equally valid. A similar convergence rate is obtained with both methods. The main advantage of the LaS method is to generate velocity fields that preserve mesh quality for large perturbations. For sensitivity calculations however, where the perturbation is infinitesimal, the EL approach is to be preferred since it offers the same accuracy at a much lower computational cost. In addition to bypassing the solution of the Laplace equation necessary for the LaS approach, the support of all the volume integrals in sensitivity Eqs. (13), (19), (24) and (26) which involve the velocity field is reduced to the layer of elements connected to the moving interfaces of Ω. Compared to classical algorithms, where the volume contributions are expressed directly on the interface γ^τ (via application of the divergence theorem), the proposed approach exhibits much better accuracy and stability, without any significant overhead.

6. Application to magnetostatics

6.1. Problem formulation

Let us consider the magnetic vector potential $\boldsymbol{A}$ formulation, $\boldsymbol{B} = \mathbf{curl}\,\boldsymbol{A}$, on a bounded domain Ω of the Magnetostatics problem excited by a current density $\boldsymbol{J}$

$$\mathbf{curl}\,\boldsymbol{H}(\boldsymbol{B}) = \boldsymbol{J} \qquad \text{in } \Omega \tag{47}$$

$$\boldsymbol{H}(\boldsymbol{B}) = \nu_{ij} B_j \boldsymbol{e}_i \qquad \text{in } \Omega \tag{48}$$

$$\boldsymbol{A} = 0 \qquad \text{on } \partial\Omega. \tag{49}$$

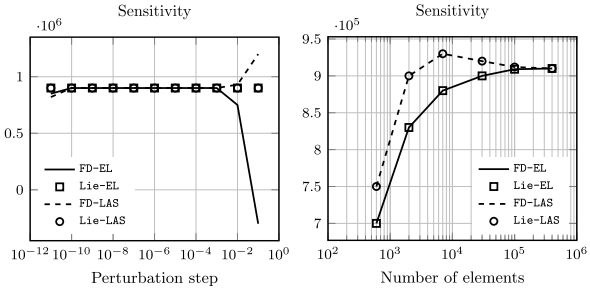

Fig. 5. A linear elastic model is defined over the plate, in Fig. 3, where the design variable τ is the major axis of the elliptical hole and the internal energy is the performance function. The sensitivity of the internal energy with respect to τ is computed using a global finite difference (FD) and the Lie derivative (Lie), for which the velocity field obtained through EL method and LaS method is used. Sensitivity based in either EL or LaS exhibits similar convergence rate with respect to perturbation step $\delta\tau$ (where the number of elements in the finite element mesh is set to 10^5) and mesh refinement (where $\delta\tau$ is set to 10^{-6}).

A homogeneous Dirichlet boundary condition (49) is assumed for the sake of simplicity. In (48), the reluctivity tensor components can be function of $\boldsymbol{B}$ (nonlinear material). The weak formulation of the problem reads [44]: find $\boldsymbol{A}^\star$ in an appropriate function space Z_A^0 verifying (49) such that

$$r(\tau, \boldsymbol{A}^\star, \bar{\boldsymbol{A}}) \equiv \int_\Omega R(\tau, \boldsymbol{A}^\star, \bar{\boldsymbol{A}}) \mathrm{d}\Omega = 0, \quad \forall \bar{\boldsymbol{A}} \in Z_A^0, \tag{50}$$

with

$$R(\tau, \boldsymbol{A}^\star, \bar{\boldsymbol{A}}) \equiv \boldsymbol{H}(\boldsymbol{B}^\star) \cdot \bar{\boldsymbol{B}} - \boldsymbol{J} \cdot \bar{\boldsymbol{A}}, \tag{51}$$

where $\boldsymbol{B}^\star = \mathbf{curl}\, \boldsymbol{A}^\star$, $\bar{\boldsymbol{B}} = \mathbf{curl}\, \bar{\boldsymbol{A}}$.

6.2. Problem sensitivity analysis

The derivative of the residual (50) at equilibrium with respect to a design variable τ is obtained by applying the chain rule of derivatives,

$$\begin{aligned} \frac{\mathrm{d}}{\mathrm{d}\tau} r(\tau, \boldsymbol{A}^\star, \bar{\boldsymbol{A}}) &= \int_\Omega \Big(L_{\mathbf{v}} \boldsymbol{H}(\boldsymbol{B}^\star) \cdot \bar{\boldsymbol{B}} + \boldsymbol{H}(\boldsymbol{B}^\star) \cdot L_{\mathbf{v}} \bar{\boldsymbol{B}} - L_{\mathbf{v}} \boldsymbol{J} \cdot \bar{\boldsymbol{A}} - \boldsymbol{J} \cdot L_{\mathbf{v}} \bar{\boldsymbol{A}} \Big) \mathrm{d}\Omega \\ &= \int_\Omega \Big(L_{\mathbf{v}} \boldsymbol{H}(\boldsymbol{B}^\star) \cdot \bar{\boldsymbol{B}} - L_{\mathbf{v}} \boldsymbol{J} \cdot \bar{\boldsymbol{A}} \Big) \mathrm{d}\Omega = 0, \end{aligned} \tag{52}$$

since the fact that $\boldsymbol{B}^\star$ is the solution of (50) implies

$$\int_\Omega \Big(H(\boldsymbol{B}^\star) \cdot L_{\mathbf{v}} \bar{\boldsymbol{B}} - \boldsymbol{J} \cdot L_{\mathbf{v}} \bar{\boldsymbol{A}} \Big) \mathrm{d}\Omega = 0,$$

since $L_{\mathbf{v}} \bar{\boldsymbol{A}} \in Z_A^0$.

Using (43), on the one hand, one has

$$L_{\mathbf{v}} \boldsymbol{H}(\boldsymbol{B}^\star) = \nu^\partial L_{\mathbf{v}} \boldsymbol{B}^\star + \nu^\partial \Big((\nabla \mathbf{v})^T \boldsymbol{B}^\star - \boldsymbol{B}^\star \operatorname{div} \mathbf{v} \Big) + (\nabla \mathbf{v})\, \boldsymbol{H}(\boldsymbol{B}^\star). \tag{53}$$

The current $\boldsymbol{J}$, on the other hand, is a 2-form. Its Lie derivative depends on how current is imposed in the model. If the current I flowing in a conducting region Ω^C of the model is fixed, one has

$$\frac{\mathrm{d}I}{\mathrm{d}\tau} = 0 = \int_{\Omega^C} L_{\mathbf{v}} \boldsymbol{J} \mathrm{d}\Omega, \tag{54}$$

A

and the term $L_{\mathbf{v}}\boldsymbol{J}$ then simply vanishes. If on the other hand the current density is constant, which is the case in our application example, one has $L_{\mathbf{v}} J_i = 0$ and by (39)

$$L_{\mathbf{v}}\boldsymbol{J} = \boldsymbol{J}\,\mathrm{div}\,\mathbf{v} - (\nabla\mathbf{v})^T\boldsymbol{J}. \tag{55}$$

Substituting (53) and (55) into (52) yields the linear system to solve for $L_{\mathbf{v}}\boldsymbol{A}^\star$

$$\int_\Omega \nu^\vartheta\, L_{\mathbf{v}}\boldsymbol{B}^\star\cdot\bar{\boldsymbol{B}}\mathrm{d}\Omega + \Big[\int_\Omega \Big(\nu^\vartheta\big((\nabla\mathbf{v})^T\boldsymbol{B}^\star - \boldsymbol{B}^\star\,\mathrm{div}\,\mathbf{v}\big)\cdot\bar{\boldsymbol{B}} + (\nabla\mathbf{v})\,\nu\boldsymbol{B}^\star\cdot\bar{\boldsymbol{B}} - (\boldsymbol{J}\,\mathrm{div}\,\mathbf{v} - (\nabla\mathbf{v})^T\boldsymbol{J})\cdot\bar{\boldsymbol{A}}\Big)\mathrm{d}\Omega\Big] = 0, \quad \forall\bar{\boldsymbol{A}}\in Z_A^0. \tag{56}$$

The first term in (56) involves the tangent stiffness matrix, which is already known from the computation of $A^\star$, and the bracketed terms make up the partial derivative term $\int_\Omega D_\tau R\mathrm{d}\Omega$ of (19).

It is to be noted that (56) is valid for 2D and 3D formulations, and generalizes the methods proposed in [17–19] that were limited to scalar unknown fields, i.e. to scalar potential 3D formulations or 2D electromagnetic problems.

6.3. Performance function

As a simple example of performance function, we choose the magnetic energy in the airgap $\Omega_f \subset \Omega$, i.e.,

$$f(\tau,\boldsymbol{A}) = \int_{\Omega_f} F(\tau,\boldsymbol{A})\mathrm{d}\Omega, \tag{57}$$

with

$$F(\tau,\boldsymbol{A}) = \frac{1}{2}\nu_0|\boldsymbol{B}|^2. \tag{58}$$

The correct way to evaluate the Lie derivative of the norm $|\boldsymbol{B}|^2$ is to write it as a scalar product $\boldsymbol{H}(\boldsymbol{B})\cdot\boldsymbol{B}$ and to invoke (43) in the linear material case this time.

One has then

$$L_{\mathbf{v}}\boldsymbol{H} = \nu_0\Big(L_{\mathbf{v}}\boldsymbol{B}\Big) + \nu_0\Big((\nabla\mathbf{v})^T\boldsymbol{B} + (\nabla\mathbf{v})\boldsymbol{B} - \boldsymbol{B}\,\mathrm{div}\,\mathbf{v}\Big),$$

and

$$\frac{\mathrm{d}}{\mathrm{d}\tau} f(\boldsymbol{\tau},\boldsymbol{A}^\star) = \int_{\Omega_f} \nu_0\, L_{\mathbf{v}}\boldsymbol{B}^\star\cdot\boldsymbol{B}^\star\mathrm{d}\Omega + \Big[\int_{\Omega_f}\frac{\nu_0}{2}\Big((\nabla\mathbf{v})^T\boldsymbol{B}^\star + (\nabla\mathbf{v})\,\boldsymbol{B}^\star - \boldsymbol{B}^\star\,\mathrm{div}\,\mathbf{v}\Big)\cdot\boldsymbol{B}^\star\mathrm{d}\Omega\Big], \tag{59}$$

where the first term and the bracketed terms are the Fréchet derivative term and the partial Lie derivative term $\int_\Omega D_\tau F\mathrm{d}\Omega$ of (13), respectively.

6.4. Numerical example

The calculation of the sensitivity is demonstrated with the inductor system depicted in Fig. 6. The system is excited by a fixed current density $\boldsymbol{J}$. The design variable τ is the thickness of the core and the performance function f is chosen as the energy in the airgap (57). The E-core is modeled with either a linear or a nonlinear magnetic material, and both a 2D and a 3D geometrical model are considered.

The EL method has been used to extend the velocity field associated with the perturbation of τ (cf. Section 5), and its nodal values (46) are shown in the bottom pictures in Fig. 6. The support of all volume integrals in (56) and (59) is then limited to one finite element layer on both sides of the moving interfaces.

The sensitivity calculated analytically is compared with that obtained by finite difference with a perturbation step chosen small enough to avoid truncation and condition errors as illustrated in Fig. 7. Convergence diagrams for the sensitivity (with $\delta\tau = 10^{-6}$) of energy and for the energy itself are presented in Figs. 8 and 9. It is first observed that the analytic approach exactly matches the finite difference approach in all cases. Convergence is slower for sensitivity

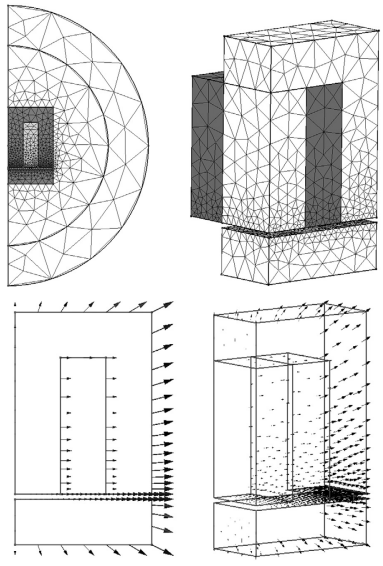

Fig. 6. Top: Magnetostatic test case for the sensitivity analysis: inductor with symmetries in 2D (left) and 3D (right) excited by a fixed current density. The design variable τ is the thickness of the magnetic core. Bottom: Nodal values on the boundaries of the velocity field (46) related to the perturbation of τ.

than for energy as the mesh is refined. As expected, convergence is also faster with second order elements. One notices that energy for first order in 3D is clearly not converged as a lot of elements in the airgap are needed. Then sensitivity is not converged yet to the exact value.

7. Application to linear elastostatics

7.1. Problem formulation

In linear elasticity, the displacement field $\boldsymbol{u} = u_j \boldsymbol{E}_j$ is expressed in an absolute vector basis $\{\boldsymbol{E}_j,\ j = 1, 2, 3\}$ of the Euclidean space E^3, whose basis vectors are not affected by the geometrical deformation associated with the variation of τ.

The gradient of the displacement field is the tensor

$$(\nabla \boldsymbol{u}) = (\nabla u_j)\boldsymbol{E}_j^T = \frac{\partial u_j}{\partial x_i}\, \boldsymbol{e}_i \boldsymbol{E}_j^T, \tag{60}$$

and the strain tensor is defined as the symmetrical part of $(\nabla \boldsymbol{u})$,

$$\boldsymbol{\epsilon} = \frac{1}{2}\big((\nabla \boldsymbol{u}) + (\nabla \boldsymbol{u})^T\big) = \epsilon_{ij}\, \boldsymbol{e}_i \boldsymbol{E}_j^T, \quad \epsilon_{ij} = \frac{1}{2}\left(\frac{\partial u_j}{\partial x_i} + \frac{\partial u_i}{\partial x_j}\right). \tag{61}$$

The stress tensor

$$\boldsymbol{\sigma} = \sigma_{ij}\, \boldsymbol{e}_i \boldsymbol{E}_j^T, \quad \sigma_{ij} = \sigma_{ji} \tag{62}$$

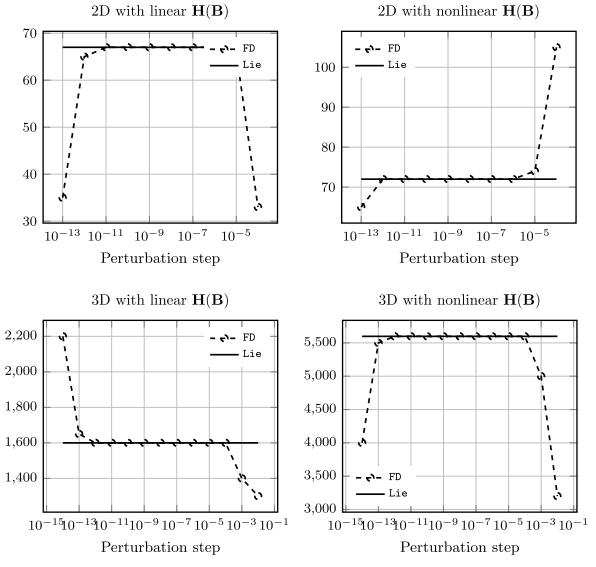

Fig. 7. Sensitivity (59) of the inductor energy (evaluated in the airgap) with respect to the magnetic core thickness computed with the finite difference method (FD) and the Lie derivative approach (Lie) for varying perturbation step in 2D (left column) and in 3D (right column). The magnetic core of the inductor is considered as linear in the top while a nonlinear reluctivity is considered in the bottom.

A

is a symmetric tensor obtained from the strain tensor by means of a constitutive relationship

$$\sigma_{ij}(\epsilon_{kl}) = C_{ijkl}\,\epsilon_{kl}. \tag{63}$$

Assuming, for the sake of simplicity, a homogeneous Dirichlet boundary condition, the elasticity problem reads

$$\operatorname{div}\boldsymbol{\sigma}(\boldsymbol{\epsilon}) + \boldsymbol{g} = 0 \qquad \text{in } \Omega, \tag{64}$$

$$\boldsymbol{\sigma}(\boldsymbol{\epsilon}) = C_{ijkl}\,\epsilon_{kl}\,\boldsymbol{e}_i\boldsymbol{E}_j^T \qquad \text{in } \Omega, \tag{65}$$

$$\boldsymbol{u} = 0 \qquad \text{on } \partial\Omega, \tag{66}$$

with $\boldsymbol{g}$ an imposed volume force density. The weak formulation of the problem reads [45]: find $\boldsymbol{u}^\star$ in an appropriate function space Z_u^0 verifying (66) such that

$$r\left(\tau, \boldsymbol{u}^\star, \bar{\boldsymbol{u}}\right) = \int_\Omega R(\tau, \boldsymbol{u}^\star, \bar{\boldsymbol{u}})\mathrm{d}\Omega, \quad \forall \bar{\boldsymbol{u}} \in Z_u^0, \tag{67}$$

with

$$R(\tau, \boldsymbol{u}^\star, \bar{\boldsymbol{u}}) \equiv \boldsymbol{\sigma}(\boldsymbol{\epsilon}^\star) : \nabla\bar{\boldsymbol{u}} - \boldsymbol{g}\cdot\bar{\boldsymbol{u}}, \tag{68}$$

where $\boldsymbol{\epsilon}^\star = \frac{1}{2}((\nabla\boldsymbol{u}^\star) + (\nabla\boldsymbol{u}^\star)^T)$.

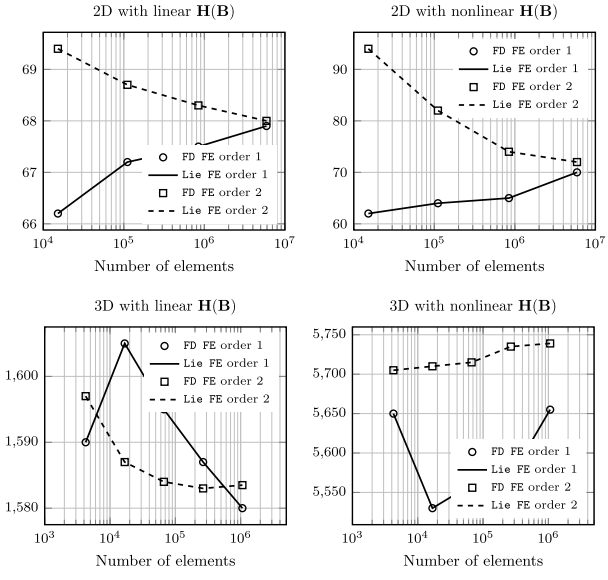

Fig. 8. Sensitivity (59) of the inductor energy (evaluated in the airgap) with respect to the magnetic core thickness computed with the finite difference method (FD) and the analytical approach (Lie) for refined mesh with respectively first order (order 1) and second order (order 2) finite elements (FE). The magnetic core of the inductor is considered as linear in the top while a nonlinear reluctivity is considered in the bottom.

A

7.2. Problem sensitivity analysis

The derivative of the residual (67) at equilibrium is obtained by the chain rule of derivatives

$$\begin{aligned}\frac{\mathrm{d}r}{\mathrm{d}\tau}(\tau,\boldsymbol{u}^\star,\bar{\boldsymbol{u}}) &= \int_\Omega \Big(L_{\mathbf{v}}\boldsymbol{\sigma}(\boldsymbol{\epsilon}^\star) : \nabla\bar{\boldsymbol{u}} + \boldsymbol{\sigma}(\boldsymbol{\epsilon}^\star) : L_{\mathbf{v}}\nabla\bar{\boldsymbol{u}} - L_{\mathbf{v}}\boldsymbol{g}\cdot\bar{\boldsymbol{u}} - \boldsymbol{g}\cdot L_{\mathbf{v}}\bar{\boldsymbol{u}}\Big)\mathrm{d}\Omega \\ &= \int_\Omega \Big(L_{\mathbf{v}}\boldsymbol{\sigma}(\boldsymbol{\epsilon}^\star) : \nabla\bar{\boldsymbol{u}} - L_{\mathbf{v}}\boldsymbol{g}\cdot\bar{\boldsymbol{u}}\Big)\mathrm{d}\Omega = 0, \end{aligned} \tag{69}$$

since

$$\int_\Omega \Big(\boldsymbol{\sigma}(\boldsymbol{\epsilon}^\star) : L_{\mathbf{v}}\nabla\bar{\boldsymbol{u}} - \boldsymbol{g}\cdot L_{\mathbf{v}}\bar{\boldsymbol{u}}\Big)\mathrm{d}\Omega = 0,$$

by (67) because $L_{\mathbf{v}}\bar{\boldsymbol{u}} \in Z_u^0$.

The Lie derivative of the elastic constitutive relationship (65) is evaluated as follows. One first note that

$$L_{\mathbf{v}}\sigma_{ij}(\epsilon_{kl}) = C_{ijkl}(L_{\mathbf{v}}\epsilon_{kl}) + D_\tau\sigma_{ij}(\epsilon_{kl}), \tag{70}$$

where, based on the same argument as (42), $D_\tau\sigma_{ij}(\epsilon_{kl}) = 0$. It then follows, reintroducing the tensor basis,

$$\begin{aligned}(L_{\mathbf{v}}\sigma_{ij})\boldsymbol{e}_i\boldsymbol{E}_j^T &= C_{ijkl}\,(L_{\mathbf{v}}\epsilon_{kl})\boldsymbol{e}_i\boldsymbol{E}_j^T \\ &= \{C\}\big(L_{\mathbf{v}}\epsilon_{kl}\,\boldsymbol{e}_k\boldsymbol{E}_l^T\big)\end{aligned}$$

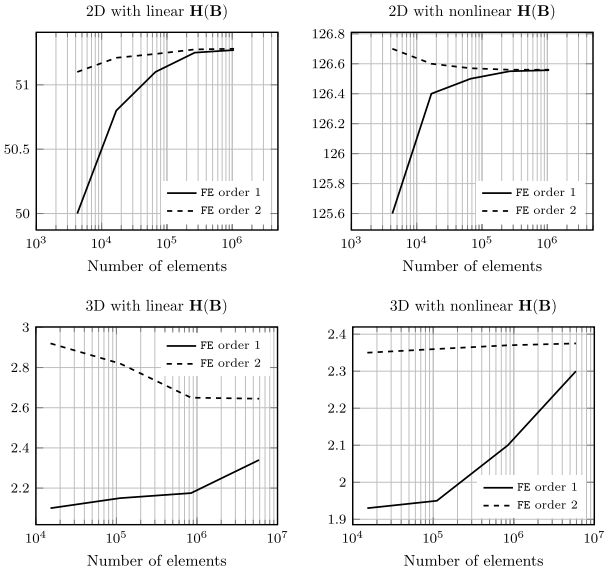

Fig. 9. Energy (57) evaluated in the airgap of the inductor, considered in 2D (first column) and 3D (second column) for refined mesh with respectively first (order 1) and second order (order 2) finite elements (FE). The magnetic core of the inductor is considered as linear in the first row while a nonlinear reluctivity is considered in the second row.

A

where, at the last line, the Hooke tensor has been written as an operator acting on the tensor $L_{\mathbf{v}}\epsilon_{kl}\ \boldsymbol{e}_k\boldsymbol{E}_l^T$. Eq. (44) can now be invoked, if one notes that the gradient $\nabla u_j = (\nabla \boldsymbol{u})\boldsymbol{E}_j$ is a 1-form whereas the vector $\sigma_{ij}\boldsymbol{e}_i = \boldsymbol{\sigma}\boldsymbol{E}_j$ is a 2-form. One has by (39) and (38)

$$L_{\mathbf{v}}(\boldsymbol{\sigma}\boldsymbol{E}_j) = (L_{\mathbf{v}}\sigma_{ij})\boldsymbol{e}_i - (\nabla\mathbf{v})^T(\boldsymbol{\sigma}\boldsymbol{E}_j) + (\boldsymbol{\sigma}\boldsymbol{E}_j)\operatorname{div}\mathbf{v}$$
$$L_{\mathbf{v}}\big((\nabla\boldsymbol{u})\boldsymbol{E}_j\big) = L_{\mathbf{v}}\epsilon_{kl}\ \boldsymbol{e}_k + (\nabla\mathbf{v})\big((\nabla\boldsymbol{u})\boldsymbol{E}_j\big),$$

so that

$$L_{\mathbf{v}}(\boldsymbol{\sigma}\boldsymbol{E}_j) + (\nabla\mathbf{v})^T(\boldsymbol{\sigma}\boldsymbol{E}_j) - (\boldsymbol{\sigma}\boldsymbol{E}_j)\operatorname{div}\mathbf{v} = \{C\}\Big(L_{\mathbf{v}}\big((\nabla\boldsymbol{u})\boldsymbol{E}_j\big) - (\nabla\mathbf{v})\big((\nabla\boldsymbol{u})\boldsymbol{E}_j\big)\Big),$$

and, after removing the constant and uniform absolute basis vector $\boldsymbol{E}_j$, which are not affected by the geometrical deformation,

$$L_{\mathbf{v}}\boldsymbol{\sigma}(\boldsymbol{\epsilon}) + (\nabla\mathbf{v})^T\boldsymbol{\sigma}(\boldsymbol{\epsilon}) - \boldsymbol{\sigma}(\boldsymbol{\epsilon})\operatorname{div}\mathbf{v} = \{C\}\big(L_{\mathbf{v}}\nabla\boldsymbol{u} - (\nabla\mathbf{v})(\nabla\boldsymbol{u})\big). \tag{71}$$

Substituting into (69) and noting that $L_{\mathbf{v}}\boldsymbol{g} = 0$ if the resultant force associated with $\boldsymbol{g}$ is independent of τ, one has finally

$$\int_\Omega \{C\}\big(L_{\mathbf{v}}\nabla\boldsymbol{u}^\star\big) : \nabla\bar{\boldsymbol{u}}\,\mathrm{d}\Omega + \Big[\int_\Omega \Big(\operatorname{div}\mathbf{v}\,\boldsymbol{\sigma}(\boldsymbol{\epsilon}^\star) : \nabla\bar{\boldsymbol{u}} - \{C\}\big((\nabla\mathbf{v})(\nabla\boldsymbol{u}^\star)\big) : \nabla\bar{\boldsymbol{u}}$$
$$- (\nabla\mathbf{v})^T\boldsymbol{\sigma}(\boldsymbol{\epsilon}^\star) : (\nabla\bar{\boldsymbol{u}})\Big)\mathrm{d}\Omega\Big] = 0, \quad \forall\bar{\boldsymbol{u}} \in Z_u^0. \tag{72}$$

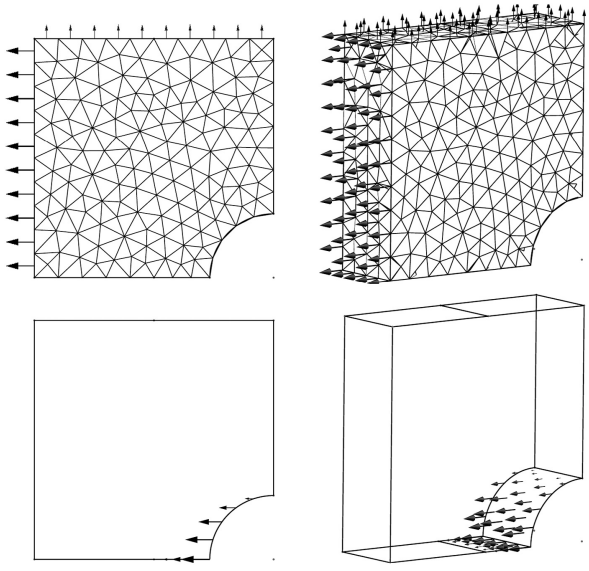

Fig. 10. Top: Elasticity test case for the sensitivity analysis: infinite plate with symmetries in 2D (left) and 3D (right) excited by a biaxial load. The design variable τ is the major axis of the elliptic hole. Bottom: Nodal values on the boundaries of the velocity field (46) related to the perturbation of τ.

The first term in (72) involves the tangent stiffness matrix of problem (67), while the bracketed terms account for the explicit dependency (i.e. holding the field argument $\boldsymbol{u}$ constant) of the residual on the variation of τ, i.e. $\int_\Omega D_\tau R \mathrm{d}\Omega$ as introduced in (19), exactly as obtained in [34].

7.3. Performance function

As a simple example of performance function, we choose the internal energy in the domain Ω, i.e.,

$$f(\tau, \boldsymbol{u}) = \int_\Omega F(\tau, \boldsymbol{u}) \mathrm{d}\Omega, \tag{73}$$

with

$$F(\tau, \boldsymbol{u}) = \frac{1}{2}\boldsymbol{\sigma}(\boldsymbol{\epsilon}) : \boldsymbol{\epsilon}. \tag{74}$$

The derivative of the performance function (73) is now obtained similarly to the derivative of the residual (69), by recalling the Lie derivative of the stress tensor (71),

$$\begin{aligned} \frac{\mathrm{d}}{\mathrm{d}\tau} f(\tau, \boldsymbol{u}^\star) = \int_\Omega \boldsymbol{\sigma}\Big(\nabla(L_{\mathbf{v}}\boldsymbol{u}^\star)\Big) : \nabla \boldsymbol{u}^\star \mathrm{d}\Omega + \Big[\frac{1}{2}\int_\Omega \Big(\operatorname{div} \mathbf{v}\, \boldsymbol{\sigma}(\boldsymbol{\epsilon}^\star) : \nabla \bar{\boldsymbol{u}} \\ - \boldsymbol{\sigma}\big((\nabla \mathbf{v})(\nabla \boldsymbol{u}^\star)\big) : \nabla \bar{\boldsymbol{u}} - \boldsymbol{\sigma}(\boldsymbol{\epsilon}^\star) : \big((\nabla \mathbf{v})(\nabla \bar{\boldsymbol{u}})\big)\Big)\mathrm{d}\Omega\Big], \end{aligned} \tag{75}$$

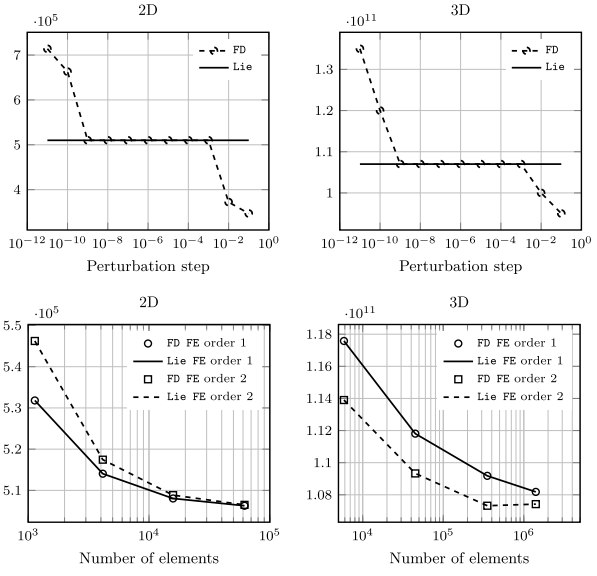

Fig. 11. Sensitivity (75) of the plate compliance (internal energy) with respect to the elliptical hole major axis length computed with the finite difference method (FD) and the Lie derivative approach (Lie). Top: the perturbation step is varied in 2D (left column) and 3D (right column). The sensitivity based on the Lie derivative does not suffer from the truncation and conditions errors proper to the FD then the choice of the perturbation step is not critical. Bottom: the mesh is refined and the convergence is studied with respectively first (order 1) and second (order 2) order finite elements (FE). Both methods converge to the same result when the mesh is refined, with a faster convergence for second order finite elements.

where the first term in (75) is the Fréchet derivative of the performance function with respect to the unknown field $\boldsymbol{u}$, while the bracketed terms are the explicit dependency (i.e. holding the field argument $\boldsymbol{u}$ constant) of f on the variation of τ, i.e. $\int_\Omega D_\tau F \mathrm{d}\Omega$ as introduced in (13).

7.4. Numerical example

The calculation of the sensitivity is demonstrated with the infinite plate with an elliptic hole depicted in Fig. 10. The system is excited by a biaxial load of fixed magnitude. The design variable τ is the major axis of the ellipse and the performance function f is chosen as the energy in the plate (73). The plate is made a linear elastic steel, and both a 2D and a 3D geometrical model are considered.

The EL method has been used, similarly to the inductor system (cf. Fig. 6), to extend the velocity field associated with the perturbation of τ (cf. Section 5), and its nodal values (46) are shown in the bottom pictures in Fig. 10. The support of all volume integrals in (72) and (75) is then limited to one finite element layer on both sides of the moving interfaces.

The sensitivity calculated analytically is compared with that obtained by finite difference with a perturbation step chosen small enough to avoid truncation and condition errors as illustrated in the top of Fig. 11. Convergence diagrams for the sensitivity (with $\delta\tau = 10^{-6}$) and the internal energy are presented in Figs. 11 and 12. All the conclusions obtained for the Magnetostatic numerical example (cf. Section 6) still hold here.

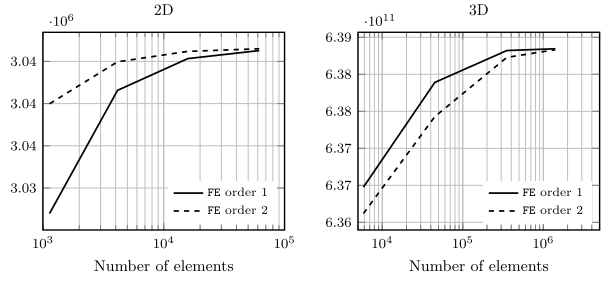

Fig. 12. Internal energy (73), considered in 2D (left) and 3D (right) for refined mesh with respectively first (order 1) and second order (order 2) finite elements (FE).

8. Conclusion and perspectives

The shape sensitivity of a performance function can be expressed analytically as a Lie derivative. Related differential geometry concepts are introduced in this paper and reformulated with conventional tensor and vector analysis notations. Theoretical formulae for shape sensitivity are derived in detail, following both the direct and the adjoint approach. The obtained formulae have a rather large number of terms, which can however either be reused from the finite element solution or evaluated on a support limited to a one layer thick layer of finite elements on both sides of the surfaces involved in the shape variation. A number of results previously obtained by other authors with a classical vector calculus approach in the area of structural mechanics and scalar magnetostatics are recovered with the proposed framework, which is however more general.

Numerical examples in nonlinear magnetostatics and linear elasticity have been presented, and validated with the finite difference approach. Convergence of the computed sensitivity with mesh refinement have been studied with first and second order elements. An efficient method for the construction of the design velocity field has been described, which allows to complete a general automatic sensitivity computation tool.

The theoretical results gathered in this paper pave the way towards more involved applications, such as eddy current problems, and multiphysics problems.

Acknowledgments

This work was supported in part by the Walloon Region of Belgium under grant RW-1217703 (WBGreen FEDO) and the Belgian Science Policy under grant IAP P7/02.

References

[1] O. Zienkiewicz, J. Campbell, Shape optimization and sequential linear programming, Optimum Struct. Des. (1973) 109–126.
[2] A. Francavilla, C. Ramakrishnan, O. Zienkiewicz, Optimization of shape to minimize stress concentration, J. Strain Anal. Eng. Des. 10 (2) (1975) 63–70.
[3] R. Fox, Constraint surface normals for structural synthesis techniques, AIAA J. 3 (8) (1965) 1517–1518.
[4] L.A. Schmit, Structural design by systematic synthesis, in: Proceedings of the Second ASCE Conference on Electronic Computation, 1960, pp. 105–122.
[5] C. Fleury, L.A. Schmit Jr., Dual methods and approximation concepts in structural synthesis, NASA (1980) CR–3226.
[6] K. Svanberg, The method of moving asymptotes- a new method for structural optimization, Internat. J. Numer. Methods Engrg. 24 (2) (1987) 359–373.
[7] Y. Nesterov, A. Nemirovskii, Y. Ye, Interior-point Polynomial Algorithms in Convex Programming, vol. 13, SIAM, 1994.
[8] H.M. Adelman, R.T. Haftka, Sensitivity analysis of discrete structural systems, AIAA J. 24 (5) (1986) 823–832.
[9] J.S. Arora, E.J. Haug, Methods of design sensitivity analysis in structural optimization, AIAA J. 17 (9) (1979) 970–974.
[10] G. Allaire, F. Jouve, A.-M. Toader, Structural optimization using sensitivity analysis and a level-set method, J. Comput. Phys. 194 (1) (2004) 363–393.

[11] K. Dems, Z. Mroz, Variational approach by means of adjoint systems to structural optimization and sensitivity analysis-II: Structure shape variation, Int. J. Solids Struct. 20 (6) (1984) 527–552.
[12] R. Haber, Application of the Eulerian-Lagrangian kinematic description to structural shape optimization, in: Proceedings of NATO ASI Computer Aided Optimal Design, 1986, pp. 297–307.
[13] E.J. Haug, J.S. Arora, Applied Optimal Design: Mechanical and Structural Systems, Wiley, 1979.
[14] U. Kirsch, Optimum Structural Design: Concepts, Methods, and Applications, McGraw-Hill, 1981.
[15] V. Komkov, K.K. Choi, E.J. Haug, Design Sensitivity Analysis of Structural Systems, vol. 177, Academic press, 1986.
[16] R.T. Haftka, Z. Gürdal, Elements of Structural Optimization, vol. 11, Springer Science & Business Media, 2012.
[17] J. Biedinger, D. Lemoine, Shape sensitivity analysis of magnetic forces, IEEE Trans. Magn. 33 (3) (1997) 2309–2316.
[18] C.-S. Koh, S.-Y. Hahn, K.-S. Lee, K. Choi, Design sensitivity analysis for shape optimization of 3-D electromagnetic devices, IEEE Trans. Magn. 29 (2) (1993) 1753–1757.
[19] I.-H. Park, J.-L. Coulomb, S.-Y. Hahn, Implementation of continuum sensitivity analysis with existing finite element code, IEEE Trans. Magn. 29 (2) (1993) 1787–1790.
[20] B. Schutz, Geometrical Methods of Mathematical Physics, Cambridge University Press, 1980.
[21] F.W. Warner, Foundations of differentiable manifolds and Lie groups, in: Graduate Texts in Mathematics, Springer-Verlag, New York, 1983.
[22] R. Bishop, S. Goldberg, Tensor Analysis on Manifolds, Macmillan, 1968.
[23] T. Frankel, The Geometry of Physics: An Introduction, Cambridge University Press, 1997.
[24] F. Henrotte, Handbook for the computation of electromagnetic forces in a continuous medium, Int. Compumag Soc. Newslett. 24 (2) (2004) 3–9.
[25] M. Botkin, Shape optimization of plate and shell structures, AIAA J. 20 (2) (1982) 268–273.
[26] V. Braibant, C. Fleury, Shape optimal design using B-splines, Comput. Methods Appl. Mech. Engrg. 44 (3) (1984) 247–267.
[27] R. Yang, M. Botkin, A modular approach for three-dimensional shape optimization of structures, AIAA J. 25 (3) (1987) 492–497.
[28] M.H. Imam, Three-dimensional shape optimization, Internat. J. Numer. Methods Engrg. 18 (5) (1982) 661–673.
[29] K.K. Choi, Shape Design Sensitivity Analysis and Optimal Design of Structural Systems, Springer, 1987.
[30] K.K. Choi, T.-M. Yao, On 3-D modeling and automatic regridding in shape design sensitivity analysis, NASA Conf. Publ. 2457 (1987) 329–345.
[31] T.-M. Yao, K.K. Choi, 3-D shape optimal design and automatic finite element regridding, Internat. J. Numer. Methods Engrg. 28 (2) (1989) 369–384.
[32] A. Belegundu, S. Rajan, A shape optimization approach based on natural design variables and shape functions, Comput. Methods Appl. Mech. Engrg. 66 (1) (1988) 87–106.
[33] S. Zhang, A. Belegundu, A systematic approach for generating velocity fields in shape optimization, Struct. Multidiscip. Optim. 5 (1) (1992) 84–94.
[34] N.H.K. Kyung K. Choi, Structural Sensitivity Analysis and Optimization 1, Springer Science & Business Media, Inc., 2005.
[35] Il-Han Park, J.L. Coulomb, Song-yop Hahn, Design sensitivity analysis for nonlinear magnetostatic problems by continuum approach, J. Phys. III France 2 (11) (1992) 2045–2053.
[36] D.-H. Kim, S.-H. Lee, I.-H. Park, J.-H. Lee, Derivation of a general sensitivity formula for shape optimization of 2-D magnetostatic systems by continuum approach, IEEE Trans. Magn. 38 (2) (2002) 1125–1128.
[37] C. Geuzaine, J.-F. Remacle, Gmsh: A 3-D finite element mesh generator with built-in pre-and post-processing facilities, Internat. J. Numer. Methods Engrg. 79 (11) (2009) 1309–1331.
[38] P. Dular, C. Geuzaine, A. Genon, W. Legros, An evolutive software environment for teaching finite element methods in electromagnetism, IEEE Trans. Magn. 35 (3) (1999) 1682–1685.
[39] C. Fleury, Conlin: an efficient dual optimizer based on convex approximation concepts, Struct. Optim. 1 (2) (1989) 81–89.
[40] K. Svanberg, A class of globally convergent optimization methods based on conservative convex separable approximations, SIAM J. Optim. (2002) 555–573.
[41] E. Kuci, C. Geuzaine, P. Dular, P. Duysinx, Shape optimization of interior permanent magnet motor for torque ripple reduction, in: Proceedings of the 4th International Conference on Engineering Optimization, 2014, p. 187.
[42] P. Duysinx, W. Zhang, C. Fleury, Sensitivity analysis with unstructured free mesh generators in 2-d shape optimization, in: Proceedings of Structural Optimization 93, The World Congress on Optimal Design of Structural Systems, Vol. 2, Structural Optimization, 1993, pp. 205–2012.
[43] R.T. Haftka, B. Barthelemy, On the accuracy of shape sensitivity, Struct. Optim. 3 (1) (1991) 1–6.
[44] A. Bossavit, Computational Electromagnetism: Variational Formulations, Complementarity, Edge Elements, Academic Press, 1998.
[45] C. Zienkiewicz, R.L. Taylor, The Finite Element Method Vol. 1: Basic Formulation and Linear Problems, in: Finite Element Method Series, vol. 3, Wiley, 1990.

A

Appendix

B

Paper II: Three-dimensional Topology Optimization of a Planar Multilayer Busbar

Noname manuscript No.
(will be inserted by the editor)

Three-dimensional Topology Optimization of a Planar Multi-layer Busbar

E. Kuci · J. Velasco · F. Henrotte · P. Duysinx · C. Geuzaine

Received: date / Accepted: date

Abstract This paper addresses the optimal design of a three-dimensional planar multilayer busbar through a density-based topology optimization. The design variables upon which the optimization acts represent the presence or absence of material at each point of the region where it is applied. They are called *densities*, and are by essence attached to matter. The optimization problem dealt with in this paper is furthermore constrained to verify the linear, time-harmonic magnetodynamic formulation governing the physical behavior of the busbar, and discretized by means of the finite element method (FEM). This paper proposes an approach to minimize the mismatch between the complex currents that go through the power switching components of the busbar, while filling at most a given volume fraction of the available domain. In addition, theoretical formulae to express sensitivity are derived based on the Lie derivative, so as to be able to use a gradient-based sequential convex programming approach, called Method of the Moving Asymptotes (MMA).

Keywords Density-based topology optimization · Lie derivative · MMA · 3D Busbar

1 Introduction

The use of switching technology, at all levels of the electrical power sector, e.g. generation, transmission and distribution [7], and for industrial processes [3], has enabled the decrease in size of hardware while maintaining high power density combined with a high efficiency and safe operation of the converter at all operating points [14], [1]. Nowadays, the switching components, characterized by a very low switching time and always increasing current levels, are interconnected to other electronic components in power converters through multilayer busbars, i.e. a thick strips of copper or aluminum. In addition to offering much lower impedances than conventional cable wiring, planar busbars allow at the same time flat, rigid and compact mechanical support for the devices. However, the presence of loop inductance can still bring significant surge voltage due to hard-switching operation of voltage source inverters [5]. This generally requires high-voltage rating of switching devices, which results in additional cost and power loss, and also, electromagnetic interferences [18]. Even if the stray effects are kept small in practical busbars, as studied for instance in [22] or [13], impedance asymmetry can appear and hence lead to current imbalance between the outputs of the busbar, especially during transients of the switching power devices [17]. Higher current capacity, on the other hand, will naturally increase heat generation in the busbar system. The main

E. Kuci
Department of Electrical Engineering and Computer Science, University of Liège, Liège, Belgium
E-mail: Erin.Kuci@uliege.be

B

challenge lies in defining the appropriate topology of the device to make them compact, light and inexpensive without compromising their performances (power losses, electromagnetic interference compatibility).

Conventionally, the bars are subdivided into several elements, seen as straight thin conductors in parallel, and the computations of the current distribution and stray inductance are done by the partial equivalent element circuit (PEEC) method [20,25]. The resulting numerical models are then used to design the busbar so as to tackle the issues mentioned above (see e.g. [19,27,6]) as well as the thermal problem (see e.g. [16,23]). Two dimensional finite element models have also been proposed, which provide a good compromise between model flexibility, accuracy and computational cost [21].

More accurate, albeit computationally more expensive, methods are also worth investigating when high fidelity simulations are desired, e.g. for high-resolution topology optimization. In this work we investigate the use of a full 3D CAD representation of the busbar combined with a linear, time-harmonic magnetodynamic finite element model, coupled with a density-based topology optimization [2]. The optimization aims at determining how copper should be distributed within the design domain, e.g. the conducting plates, to reach the objectives mentioned above without having to make any a priori guess about the final distribution, which offers a great flexibility in the design.

A sequential convex programming method, well known in the field of structural engineering, called Method of the Moving Asymptotes (MMA) is used in this paper to determine the solution of such problems [11,26], based on the sensitivity matrix of the problem. The latter accounts for the dependency of the performance functions with respect to the design variables. Most existing sensitivity calculation approaches deal with 2D static systems, leaving aside 3D and time-harmonic cases. The extension to harmonic fields however requires adapted theoretical frameworks [15,4]. We show in this paper how this setting allows to derive the variational sensitivity formula for a general 3D time-harmonic magnetodynamic problem, in an adjoint approach.

The paper is organized as follows. The parameterization of the busbar and the time-harmonic magnetodynamic variational formulation are presented in Section 2, while the density based topology optimization problem is posed in Section 3. Section 4 details formulae to express practically the derivative of both the performance functions and the time-harmonic magnetodynamic problem with respect to density variables. In Section 5, the general framework is applied to the optimal design of a 3D busbar.

2 Description of the physical model

A representative three-dimensional laminated busbar is considered as a bounded domain, noted Ω. It is made up of tightly pressed conducting plates separated by a thin dielectric material for insulation, see Fig. 1. A sinusoidal current, injected through a surface Σ_I, feeds the busbar. A fixed spatial discretization of Ω is undertaken and in particular, the spatial discretization of the conducting domain, noted $\Omega_C \subset \Omega$, is used as the support for a density field, noted ρ. The optimization design variables are chosen as an element-wise sampling of that field, and are allowed to vary between a lower bound that represents air noted ρ^{min}, and an upper bound that represents copper, noted ρ^{max}, allowing hence to create or remove holes in Ω_C.

The system is modeled in terms of a time-harmonic magnetodynamic $\boldsymbol{A}-v$ formulation, written at the continuous level by its weak formulation [10]. It reads: find $\boldsymbol{A}$ and v in appropriate complex function spaces, respectively Z_A^0 and Z_v^I and verifying appropriate boundary conditions such that

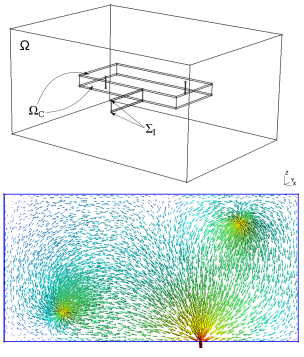

Fig. 1 Considered three-dimensional busbar fed by a sinusoidal current (scaling factor of 10 in the z direction for better visibility).

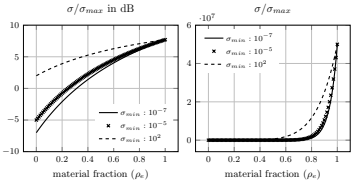

Fig. 2 Conductivity as a function of densitiy in logarithmic scale (2) (left) and natural scale (right) for various σ_{min}, and σ_{max} set to $5 \cdot 10^7$ (S/m).

the residual $r(\boldsymbol{A}, v, \boldsymbol{A}', v')$ is cancelled:

$$\begin{aligned} &\int_{\Omega} \nu \, \mathbf{curl}\, \boldsymbol{A} \cdot \mathbf{curl}\, \boldsymbol{A}' \, \mathrm{d}\Omega + \int_{\Omega_C} \sigma \left(i\omega \boldsymbol{A} + \nabla v \right) \cdot \boldsymbol{A}' \, \mathrm{d}\Omega = 0, \ \forall \boldsymbol{A}' \in Z_A^0 \\ &\int_{\Omega_C} \sigma \left(i\omega \boldsymbol{A} + \nabla v \right) \cdot \nabla v' \, \mathrm{d}\Omega - \int_{\Sigma_I} I_s \cdot v' \, \mathrm{d}\Omega = 0, \ \forall v' \in Z_v^I \end{aligned} \tag{1}$$

with $\boldsymbol{A}$ the magnetic vector potential on Ω and v the electric potential on the conducting region $\Omega_C \subset \Omega$. In (1), ν is the reluctivity, σ is the conductivity, i is the pure imaginary complex number (such that $i^2 = -1$), $\omega = 2\pi f$ is the angular frequency computed for a given frequency f and I_s, the global current. The two left-hand sides in (1) define the residual $r(\boldsymbol{A}, v, \boldsymbol{A}', v')$, which is complex-valued for the time-harmonic problem. The residual as well as $\boldsymbol{A}$ and v are complex-valued, while the test functions $\boldsymbol{A}'$ and v' are real-valued.

An interpolation scheme assigns conductivity to points of intermediate density. However, special care must be taken in the selection of the interpolation scheme as the magnitude of the conductivity at $\rho = \rho_{max}$ strongly affects the solution of (1), and thus the span of several order of magnitudes of σ in the design domain is crucial. As the conductivity varies from σ_{min} to σ_{max}, an interpolation in logarithmic scale [8] is adopted,

$$\log_{10}\sigma = \log_{10}(\sigma_{max}) - \frac{1-\rho}{1+\rho}\log_{10}(\frac{\sigma_{max}}{\sigma_{min}}), \tag{2}$$

with numerical experiments shown in Fig. 2 for various σ_{min}.

3 Topology optimization problem

Let us introduce,

$$\Delta I(\rho, \boldsymbol{A}^\dagger, v^\dagger) = I_{\Sigma_1}(\rho, \boldsymbol{A}^\dagger, v^\dagger) - I_{\Sigma_2}(\rho, \boldsymbol{A}^\dagger, v^\dagger), \tag{3}$$

the mismatch between the complex currents I_{Σ_1} and I_{Σ_2} in the vertical vias, Σ_1 and Σ_2, of the busbar, and

$$||\Delta I(\rho, \boldsymbol{A}^\dagger, v^\dagger)||_2^2 = \Delta I(\rho, \boldsymbol{A}^\dagger, v^\dagger) \cdot \Big(\Delta I(\rho, \boldsymbol{A}^\dagger, v^\dagger)\Big)^\star, \tag{4}$$

the square L-2 norm of ΔI. The density-based topology optimization problem aims at determining the optimal density field ρ for the two plates of the busbar, that minimizes the mismatch between the complex currents I_{Σ_1} and I_{Σ_2} in the vertical vias, while filling at most a given volume fraction α of the available domain and keeping at the same time the impedance of the busbar unchanged from the basic design. The performance functions of the optimization problem are a function of the physical problem (1) solution. The optimization problem reads,

$$\begin{aligned} \min_{\rho} \quad & f(\rho, \boldsymbol{A}^\dagger, v^\dagger) \equiv ||\Delta I(\rho, \boldsymbol{A}^\dagger, v^\dagger)||_2^2 \\ s.t. \quad & \int_{\Omega_C} \rho \, \mathrm{d}\Omega \leq \alpha \int_{\Omega_C} \mathrm{d}\Omega \\ & \rho^{min} \equiv 0 \leq \rho \leq \rho^{max} \\ & r(\boldsymbol{A}^\dagger, v^\dagger, \boldsymbol{A}', v') = 0, \ \forall \boldsymbol{A}' \in Z_A^0, \forall v' \in Z_v^I. \end{aligned} \tag{5}$$

In (5), the results $\boldsymbol{A}^\dagger$ and $v^\dagger$ of problem (1) are used to determine the currents I_{Σ_1} and I_{Σ_2} in the vertical branches for a given density field ρ. The repetition of these evaluations is time-consuming for large scale applications. In this article, a gradient-based sequential convex programming algorithm called Method of the Moving Asymptotes [26] (MMA) is used. It builds convex and separable local approximations of the performance functions (currents and volume).

4 Adjoint-based sensitivity analysis

We shall, for sake of simplicity, consider one particular performance function, noted f, and one particular design variable, noted ρ. The treatment of any other performance function will be identical. The real part of a complex number x is noted $\mathcal{R}_e\{x\}$, while its imaginary part is noted $\mathcal{I}_m\{x\}$ and the conjugate complex of x is noted $x^\star$.

4.1 Analytical expression of sensitivity

In a general setting, the real-valued square L-2 norm of the current mismatch can be written as

$$f(\rho, \boldsymbol{A}^\dagger, v^\dagger) = \int_{\Omega_C} F(\rho, \boldsymbol{A}^\dagger, v^\dagger)\ \mathrm{d}\Omega, \tag{6}$$

where the function F depends explicitly on its complex-valued parameters; $\boldsymbol{A}$ and v themselves depending implicitly on ρ. Their derivative with respect to ρ, can be obtained analytically (prior to discretization) by differentiation under the integral sign. We have shown previously (see [15]) that for real-valued physical problems the sensitivities can be derived in a unified fashion, in 2D or 3D with the velocity method [24], by means of an explicit Lie differentiation of the weak formulation terms. Building on the same methodology, analytical expressions of sensitivity are derived in what follows.

The derivative of f with respect to ρ,

$$\begin{aligned}\frac{\mathrm{d}f}{\mathrm{d}\rho}(\rho, \boldsymbol{A}^\dagger, v^\dagger) = \int_{\Omega_C} \Big(& D_\rho F(\rho, \boldsymbol{A}^\dagger, v^\dagger) + \big\{\mathrm{D}_{\boldsymbol{A}} F(\rho, \boldsymbol{A}^\dagger, v^\dagger)\big\}\big(\frac{\mathrm{d}\boldsymbol{A}^\dagger}{\mathrm{d}\rho}\big) \\ & + \big\{\mathrm{D}_v F(\rho, \boldsymbol{A}^\dagger, v^\dagger)\big\}\big(\frac{\mathrm{d}v^\dagger}{\mathrm{d}\rho}\big)\Big)\ \mathrm{d}\Omega,\end{aligned} \tag{7}$$

has got three terms. The first term is the partial derivative of the functional,

$$D_\rho F(\rho, \boldsymbol{A}^\dagger, v^\dagger) = \frac{\mathrm{d}F}{\mathrm{d}\rho}(\rho, \boldsymbol{A}^\dagger, v^\dagger)\Big|_{\frac{\mathrm{d}\boldsymbol{A}}{\mathrm{d}\rho}=0, \frac{\mathrm{d}v}{\mathrm{d}\rho}=0} \tag{8}$$

defined as the derivative holding the field arguments $\boldsymbol{A}$ and v constants, while the other terms involve the Fréchet derivative of the functional $F(\rho, \boldsymbol{A}, v)$ with respect to its field arguments $\boldsymbol{A}$, defined by

$$\lim_{|\delta\boldsymbol{A}|\to 0} \frac{1}{|\delta\boldsymbol{A}|}\Big|F(\rho, \boldsymbol{A}+\delta\boldsymbol{A}, v) - F(\rho, \boldsymbol{A}, v) - \big\{\mathrm{D}_{\boldsymbol{A}} F(\rho, \boldsymbol{A}, v)\big\}(\delta\boldsymbol{A})\Big| = 0, \tag{9}$$

where the limit is taken over all sequences of non-zero $\delta\boldsymbol{A}$ that converge to zero. Similarly, the Fréchet derivative of the functional with respect to v reads

$$\lim_{|\delta v|\to 0} \frac{1}{|\delta v|}\Big|F(\rho, \boldsymbol{A}, v+\delta v) - F(\rho, \boldsymbol{A}, v) - \big\{\mathrm{D}_v F(\rho, \boldsymbol{A}, v)\big\}(\delta v)\Big| = 0. \tag{10}$$

The Fréchet derivative is a linear operator applied to the argument in between parenthesis outside the curly braces, and evaluated in arguments between parenthesis inside the curly braces.

A real-valued augmented Lagrangian function is defined,

$$\begin{aligned} f_a(\rho, \boldsymbol{A}, v, \boldsymbol{\lambda}_A, \lambda_v) &= f(\rho, \boldsymbol{A}, v) - r(\rho, \boldsymbol{A}, v, \boldsymbol{\lambda}_A, \lambda_v) \\ &\quad - r^\star(\rho, \boldsymbol{A}^\star, v^\star, \boldsymbol{\lambda}_A^\star, \lambda_v^\star) \\ &= \mathcal{R}_e\Big\{f(\rho, \boldsymbol{A}, v) - 2\, r(\rho, \boldsymbol{A}, v, \boldsymbol{\lambda}_A, \lambda_v)\Big\}\end{aligned} \tag{11}$$

with $\boldsymbol{\lambda}_A$ a Lagrange multiplier associated to $\boldsymbol{A}$ and λ_v a Lagrange multiplier associated to v. Both $\boldsymbol{\lambda}_A$ and λ_v are complex-valued adjoint fields.

As (1) implies that the residual $r(\rho, \boldsymbol{A}^\dagger, v^\dagger, \boldsymbol{\lambda}_A, \lambda_v)$, as well as its complex conjugate, is zero at equilibrium, one has

$$f_a(\rho, \boldsymbol{A}^\dagger, v^\dagger, \boldsymbol{\lambda}_A, \lambda_v) = f(\rho, \boldsymbol{A}^\dagger, v^\dagger), \tag{12}$$

B

and the sensitivity is expressed in terms of f_a by

$$\frac{\mathrm{d}f}{\mathrm{d}\rho}(\rho, \boldsymbol{A}^\dagger, v^\dagger) = \frac{\mathrm{d}f_a}{\mathrm{d}\rho}(\rho, \boldsymbol{A}^\dagger, v^\dagger, \boldsymbol{\lambda}_A, \lambda_v). \tag{13}$$

The differentiation of (11) with respect to ρ yields

$$\begin{aligned}\frac{\mathrm{d}f_a}{\mathrm{d}\rho}(\rho, \boldsymbol{A}^\dagger, v^\dagger, \boldsymbol{\lambda}_A, \lambda_v) = \mathcal{R}_e\Big\{ \int_{\Omega_C} \Big(& D_\rho F(\rho, \boldsymbol{A}^\dagger, v^\dagger) \\ & + \{\mathrm{D}_{\boldsymbol{A}} F(\rho, \boldsymbol{A}^\dagger, v^\dagger)\}(\frac{\mathrm{d}\boldsymbol{A}^\dagger}{\mathrm{d}\rho}) + \{\mathrm{D}_v F(\rho, \boldsymbol{A}^\dagger, v^\dagger)\}(\frac{\mathrm{d}v^\dagger}{\mathrm{d}\rho}) \Big)\ \mathrm{d}\Omega \\ & - 2\int_\Omega \nu\, \mathbf{curl}\, \frac{\mathrm{d}\boldsymbol{A}^\dagger}{\mathrm{d}\rho} \cdot \mathbf{curl}\, \boldsymbol{\lambda}_A\ \mathrm{d}\Omega - 2\int_{\Omega_C} \frac{\mathrm{d}\sigma}{\mathrm{d}\rho} \left(i\omega \boldsymbol{A}^\dagger + \nabla v^\dagger \right) \cdot \boldsymbol{\lambda}_A\ \mathrm{d}\Omega \\ & - 2\int_{\Omega_C} \sigma \left(i\omega \frac{\mathrm{d}\boldsymbol{A}^\dagger}{\mathrm{d}\rho} + \nabla \frac{\mathrm{d}v^\dagger}{\mathrm{d}\rho} \right) \cdot \boldsymbol{\lambda}_A\ \mathrm{d}\Omega - 2\int_{\Omega_C} \frac{\mathrm{d}\sigma}{\mathrm{d}\rho} \left(i\omega \boldsymbol{A}^\dagger + \nabla v^\dagger \right) \cdot \nabla\lambda_v\ \mathrm{d}\Omega \\ & - 2\int_{\Omega_C} \sigma \left(i\omega \frac{\mathrm{d}\boldsymbol{A}^\dagger}{\mathrm{d}\rho} + \nabla \frac{\mathrm{d}v^\dagger}{\mathrm{d}\rho} \right) \cdot \nabla\lambda_v\ \mathrm{d}\Omega \Big\}\end{aligned} \tag{14}$$

where we have already omitted the null term.

Let now $\boldsymbol{\lambda}_A^\dagger$ and $\lambda_v^\dagger$ be the solution of the so-called adjoint problem,

$$\begin{cases} \displaystyle\int_{\Omega_C} \{\mathrm{D}_{\boldsymbol{A}} F(\rho, \boldsymbol{A}^\dagger, v^\dagger)\}(\frac{\mathrm{d}\boldsymbol{A}^\dagger}{\mathrm{d}\rho})\ \mathrm{d}\Omega - \int_\Omega \nu\, \mathbf{curl}\, \boldsymbol{\lambda}_A \cdot \mathbf{curl}\, \frac{\mathrm{d}\boldsymbol{A}^\dagger}{\mathrm{d}\rho}\ \mathrm{d}\Omega \\ \displaystyle - \int_{\Omega_C} i\omega\sigma \left(\boldsymbol{\lambda}_A + \nabla\lambda_v \right) \cdot \frac{\mathrm{d}\boldsymbol{A}^\dagger}{\mathrm{d}\rho}\ \mathrm{d}\Omega = 0,\ \forall \frac{\mathrm{d}\boldsymbol{A}^\dagger}{\mathrm{d}\rho} \in Z_{\boldsymbol{\lambda}_A} \\ \displaystyle\int_{\Omega_C} \{\mathrm{D}_v F(\rho, \boldsymbol{A}^\dagger, v^\dagger)\}(\frac{\mathrm{d}v^\dagger}{\mathrm{d}\rho})\ \mathrm{d}\Omega \\ \displaystyle - \int_{\Omega_C} \sigma \left(\boldsymbol{\lambda}_A + \nabla\lambda_v \right) \cdot \nabla \frac{\mathrm{d}v^\dagger}{\mathrm{d}\rho}\ \mathrm{d}\Omega = 0,\ \forall \frac{\mathrm{d}v^\dagger}{\mathrm{d}\rho} \in Z_{\boldsymbol{\lambda}_v}. \end{cases} \tag{15}$$

Sensitivity is then given by

$$\begin{aligned}\frac{\mathrm{d}f_a}{\mathrm{d}\rho}(\rho, \boldsymbol{A}^\dagger, v^\dagger, \boldsymbol{\lambda}_A, \lambda_v) = & \int_{\Omega_C} D_\rho F(\rho, \boldsymbol{A}^\dagger, v^\dagger)\ \mathrm{d}\Omega \\ & - 2\,\mathcal{R}_e\Big\{ \int_{\Omega_C} \frac{\mathrm{d}\sigma}{\mathrm{d}\rho}\ (i\omega \boldsymbol{A} + \nabla v) \cdot (\boldsymbol{\lambda}_A + \nabla\lambda_v)\ \mathrm{d}\Omega \Big\}\end{aligned} \tag{16}$$

in terms of the solutions of (1) and of the adjoint problem (15).

The system matrix of adjoint problem (15) is the tangent stiffness matrix of the problem (1), i.e. the Jacobian matrix after finite element discretization and convergence of the iterative nonlinear process. It can be reused since the same discretization is used for solving (15) and (1).

B

4.2 Wirtinger's derivative

We now present formulae to evaluate the derivative of a real-valued performance function g with respect to its complex-valued argument x. We then extend the result to the calculation of the Fréchet derivative of f with respect to $\boldsymbol{A}$ and v, which appears in the load of the adjoint problem (15).

The complex-valued function argument x can be written by means of its real part, $\mathcal{R}_e\{x\}$, and its imaginary part, $\mathcal{I}_m\{x\}$, such as $x = \mathcal{R}_e\{x\} + i\,\mathcal{I}_m\{x\}$. One can therefore use classical $\mathbb{R}^2$

calculus for the calculation of the partial derivatives of g with respect to the real and imaginary components of the function arguments, i.e. $g(\rho, x) = g(\mathcal{R}_e\{x\}, \mathcal{I}_m\{x\})$, and obtain the sensitivity of g with respect to each component of g. Going back to the function f, this approach will require to split the adjoint formulation (15) for the real part and imaginary part of $\boldsymbol{A}$ and v fields. It will therefore lead to a total of four adjoint systems which should be solved. One can, on the other hand, apply the more general framework of Wirtinger's calculus (see for instance [4]), which provides a more elegant and comfortable alternative that allows to solve the single adjoint problem.

Let us consider the first order Taylor expansion of $g(x)$,

$$g(x+\delta x) = g(x) + \frac{\partial g(x)}{\partial \mathcal{R}_e\{x\}}\, \mathcal{R}_e\{\delta x\} + \frac{\partial g(x)}{\partial \mathcal{I}_m\{x\}}\, \mathcal{I}_m\{\delta x\} + O\Big(|\delta x|^2\Big)\,, \tag{17}$$

since g is differentiable at any x. We can write successively the real part of δx,

$$\mathcal{R}_e\{\delta x\} = \frac{1}{2}\Big(\delta x + \delta x^\star\Big),$$

as well as the imaginary part of δx,

$$\mathcal{I}_m\{\delta x\} = \frac{1}{2i}\Big(\delta x - \delta x^\star\Big),$$

in terms of δx and $\delta x^\star$ and replace them in (17),

$$\begin{aligned} g(x+\delta x) = g(x) &+ \frac{1}{2}\Big(\frac{\partial g(x)}{\partial \mathcal{R}_e\{x\}} - i\,\frac{\partial g(x)}{\partial \mathcal{I}_m\{x\}}\Big)\,\delta x \\ &+ \frac{1}{2}\Big(\frac{\partial g(x)}{\partial \mathcal{R}_e\{x\}} + i\,\frac{\partial g(x)}{\partial \mathcal{I}_m\{x\}}\Big)\,\delta x^\star + O\Big(|\delta x|^2\Big)\,, \end{aligned}$$

so that we end up with

$$\begin{aligned} \frac{g(x+\delta x) - g(x)}{\delta x} = &\frac{1}{2}\Big(\frac{\partial g(x)}{\partial \mathcal{R}_e\{x\}} - i\,\frac{\partial g(x)}{\partial \mathcal{I}_m\{x\}}\Big) \\ &+ \frac{1}{2}\Big(\frac{\partial g(x)}{\partial \mathcal{R}_e\{x\}} + i\,\frac{\partial g(x)}{\partial \mathcal{I}_m\{x\}}\Big)\,\frac{\delta x^\star}{\delta x} + \frac{O\big(|\delta x|^2\big)}{\delta x}. \end{aligned} \tag{18}$$

Taking the limit of (18) for δx going to zero, the term in $\delta x^\star/\delta x$ vanishes. Indeed, expressing δx in polar coordinates, one has $\delta x = r\, e^{\theta}$ and $\delta x^\star = r\, e^{-\theta}$,

$$\lim_{r\to 0} \frac{1}{2}\Big(\frac{\partial g}{\partial \mathcal{R}_e\{x\}} + i\,\frac{\partial g}{\partial \mathcal{I}_m\{x\}}\Big)\, e^{-2\theta} = 0 \tag{19}$$

holds only if

$$\frac{\partial g}{\partial \mathcal{R}_e\{x\}} + i\,\frac{\partial g}{\partial \mathcal{I}_m\{x\}} = 0, \tag{20}$$

which is called the Cauchy-Riemann condition.

Hence, (18) leads to the Wirtinger's derivative of g with respect to its complex argument,

$$\frac{\mathrm{d}g}{\mathrm{d}x}(x) \equiv \frac{1}{2}\Big(\frac{\partial g(x)}{\partial \mathcal{R}_e\{x\}} - i\,\frac{\partial g(x)}{\partial \mathcal{I}_m\{x\}}\Big), \tag{21}$$

which is expressed in terms of the derivative of g with respect to the real part as well as the imaginary part of x.

B

Building on the same methodology, the Fréchet derivative of F with respect to its arguments can therefore be obtained as the combination of the Fréchet derivative of F with respect to the real and imaginary parts of its arguments:

$$\{\mathrm{D}_{\boldsymbol{A}} F(\rho, \boldsymbol{A}^\dagger, v^\dagger)\}\big(\frac{\mathrm{d}\boldsymbol{A}^\dagger}{\mathrm{d}\rho}\big) = \frac{1}{2}\Big(\{\mathrm{D}_{\mathcal{R}_e\{\boldsymbol{A}\}} F(\rho, \boldsymbol{A}^\dagger, v^\dagger)\}\big(\frac{\mathrm{d}\boldsymbol{A}^\dagger}{\mathrm{d}\rho}\big) - i\,\{\mathrm{D}_{\mathcal{I}_m\{\boldsymbol{A}\}} F(\rho, \boldsymbol{A}^\dagger, v^\dagger)\}\big(\frac{\mathrm{d}\boldsymbol{A}^\dagger}{\mathrm{d}\rho}\big)\Big) \tag{22}$$

$$\{\mathrm{D}_{v} F(\rho, \boldsymbol{A}^\dagger, v^\dagger)\}\big(\frac{\mathrm{d}v^\dagger}{\mathrm{d}\rho}\big) = \frac{1}{2}\Big(\{\mathrm{D}_{\mathcal{R}_e\{v\}} F(\rho, \boldsymbol{A}^\dagger, v^\dagger)\}\big(\frac{\mathrm{d}v^\dagger}{\mathrm{d}\rho}\big) - i\,\{\mathrm{D}_{\mathcal{I}_m\{v\}} F(\rho, \boldsymbol{A}^\dagger, v^\dagger)\}\big(\frac{\mathrm{d}v^\dagger}{\mathrm{d}\rho}\big)\Big). \tag{23}$$

4.3 Numerical validation

The sensitivity (16) calculated analytically by solving the adjoint problem (15), with (22) and (23) as adjoint loads, is compared with that obtained by finite difference,

$$\frac{\mathrm{d}f}{\mathrm{d}\rho}(\rho, \boldsymbol{A}^\dagger, v^\dagger) \approx \frac{f(\rho + \delta\rho, \boldsymbol{A}^\dagger, v^\dagger) - f(\rho, \boldsymbol{A}^\dagger, v^\dagger)}{\delta\rho}, \tag{24}$$

with a perturbation step, $\delta\rho$, chosen small enough to avoid truncation and condition errors, see Fig. 3. It is observed that the analytic approach exactly matches the finite difference approach (with $\delta\rho = 10^{-6}$).

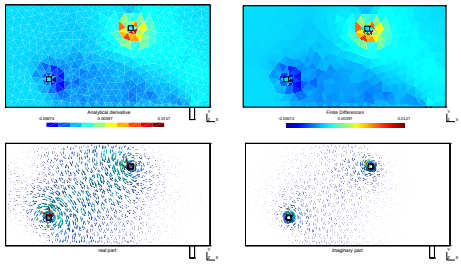

Fig. 3 The busbar is fed with a current I_s of a 500 Hz and the sensitivity of the current mismatch (4) is computed with the analytical formula (16), top left, with the complex-valued adjoint fields (see $\mathcal{R}_e\{\mathbf{curl}\,\boldsymbol{\lambda}_A\}$ in bottom left, and $\mathcal{I}_m\{\mathbf{curl}\,\boldsymbol{\lambda}_A\}$ in bottom right obtained by solving (15)). The finite differences, top right, with a perturbation step set to 10^{-6} are also applied. It is first observed that the variational approach exactly matches the finite difference approach.

5 Numerical application

The sensitivity formula (16) is now applied to a general procedure for the density-based topology optimization of the 3D busbar, see Fig. 1. The MMA optimizer [26] is used to solve the constrained optimization problem (5) for a volume fraction α set to 50%. The busbar is optimized for two frequencies: 500 Hz and 50 kHz, corresponding respectively to a mostly resistive and to an inductive behavior. The mesh is refined as the frequency increases so as to have about two elements in the skin depth, leading to a mesh with 112 794 finite elements at 500 Hz and a mesh with 360 962 finite elements at 50 kHz. The results are summarized in Fig. 4. The optimization process results in thinner copper paths compared to the original design. The optimized design enables to obtain currents in phase in the two vertical branches with a drastic reduction of the copper amount. In particular the optimization allows to improve the current sharing between the complex currents in the vertical vias from 36% to 0.2% at 500 Hz and from 42% to 0.1% at 50 kHz. All the numerical simulations have been performed using the open source finite element code GetDP/Gmsh [9, 12].

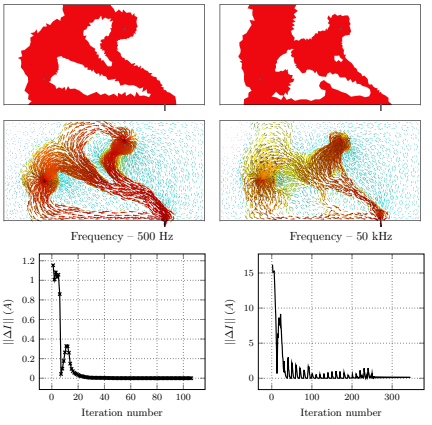

Fig. 4 The busbar is fed with a current I_s of a 500 Hz (left column), as well as a current of 50 kHz and the optimal copper distribution of its plates is obtained for both frequencies as the solution of (5). In all cases the squared L2-norm of the current mismatch between the currents, is greatly reduced compared to the initial design.

B

6 Conclusion and perspectives

A variational formulation for the sensitivity of a performance function as well as magnetodynamics equations in time-harmonic domain with respect to material densities has been obtained following both the direct and the adjoint approach. The sensitivity has been used by a gradient-based

sequential convex programming algorithm to determine the optimal layout for the two plates of a representative three-dimensional busbar that minimizes the mismatch between the complex currents in the vertical vias of the busbar, while filling at most a given volume fraction of the available domain. The impedance of the busbar remains unchanged from the basic design.

Acknowledgements This work was supported in part by the Walloon Region of Belgium under grant RW-1217703 (WBGreen FEDO), the Belgian Science Policy under grant IAP P7/02 and grant PIT7508 (ATAC-HP).

References

1. Abu-Rub, H., Holtz, J., Rodriguez, J., Baoming, G.: Medium-voltage multilevel convertersstate of the art, challenges, and requirements in industrial applications. IEEE Transactions on Industrial Electronics **57**(8), 2581–2596 (2010)
2. Bendsøe, M.P.: Optimal shape design as a material distribution problem. Structural and multidisciplinary optimization **1**(4), 193–202 (1989)
3. Bernet, S.: Recent developments of high power converters for industry and traction applications. IEEE Transactions on Power Electronics **15**(6), 1102–1117 (2000)
4. Bouboulis, P.: Wirtinger's Calculus in general Hilbert Spaces. CoRR **abs/1005.5170** (2010). URL http://arxiv.org/abs/1005.5170
5. Braun, D., Pixler, D., LeMay, P.: Igbt module rupture categorization and testing. In: Industry Applications Conference, 1997. Thirty-Second IAS Annual Meeting, IAS'97., Conference Record of the 1997 IEEE, vol. 2, pp. 1259–1266. IEEE (1997)
6. Caponet, M.C., Profumo, F., De Doncker, R.W., Tenconi, A.: Low stray inductance bus bar design and construction for good emc performance in power electronic circuits. IEEE Transactions on Power Electronics **17**(2), 225–231 (2002)
7. Carrasco, J.M., Franquelo, L.G., Bialasiewicz, J.T., Galván, E., PortilloGuisado, R.C., Prats, M.M., León, J.I., Moreno-Alfonso, N.: Power-electronic systems for the grid integration of renewable energy sources: A survey. IEEE Transactions on industrial electronics **53**(4), 1002–1016 (2006)
8. Diaz, A.R., Sigmund, O.: A topology optimization method for design of negative permeability metamaterials. Structural and Multidisciplinary Optimization **41**(2), 163–177 (2010)
9. Dular, P., Geuzaine, C., Henrotte, F., Legros, W.: A general environment for the treatment of discrete problems and its application to the finite element method. IEEE Transactions on Magnetics **34**(5), 3395–3398 (1998)
10. Dular, P., Henrotte, F., Legros, W.: A general and natural method to define circuit relations associated with magnetic vector potential formulations. IEEE transactions on magnetics **35**(3), 1630–1633 (1999)
11. Fleury, C., Schmit Jr, L.A.: Dual methods and approximation concepts in structural synthesis. NASA pp. CR–3226 (1980)
12. Geuzaine, C., Remacle, J.F.: Gmsh: A 3-D finite element mesh generator with built-in pre-and post-processing facilities. International Journal for Numerical Methods in Engineering **79**(11), 1309–1331 (2009)
13. Guichon, J., Aimé, J., Schanen, J., Martin, C., Roudet, J., Clavel, E., Arpilliere, M., Pasterczyk, R., Le Floch, Y.: Busbar design: How to spare nanohenries? In: Industry Applications Conference, 2006. 41st IAS Annual Meeting. Conference Record of the 2006 IEEE, vol. 4, pp. 1865–1869. IEEE (2006)
14. Kouro, S., Malinowski, M., Gopakumar, K., Pou, J., Franquelo, L.G., Wu, B., Rodriguez, J., Pérez, M.A., Leon, J.I.: Recent advances and industrial applications of multilevel converters. IEEE Transactions on industrial electronics **57**(8), 2553–2580 (2010)
15. Kuci, E., Henrotte, F., Duysinx, P., Geuzaine, C.: Design sensitivity analysis for shape optimization based on the Lie derivative. Computer Methods in Applied Mechanics and Engineering **317**, 702 – 722 (2017)
16. Matsumori, T., Kondoh, T., Kawamoto, A., Nomura, T.: Topology optimization for fluid–thermal interaction problems under constant input power. Structural and Multidisciplinary Optimization **47**(4), 571–581 (2013)
17. Ohi, T., Horiguchi, T., Okuda, T., Kikunaga, T., Matsumoto, H.: Analysis and measurement of chip current imbalances caused by the structure of bus bars in an igbt module. In: Industry Applications Conference, 1999. Thirty-Fourth IAS Annual Meeting. Conference Record of the 1999 IEEE, vol. 3, pp. 1775–1779. IEEE (1999)
18. Ott, H.W.: Electromagnetic compatibility engineering. John Wiley & Sons (2011)
19. Pasterczyk, R., Martin, C., Guichon, J.M., Schanen, J.L.: Planar busbar optimization regarding current sharing and stray inductance minimization. In: Power Electronics and Applications, 2005 European Conference on, pp. 9–pp. IEEE (2005)
20. Piette, N., Marechal, Y., Clavel, E.: Calculation of electrodynamic efforts on busbar technology: comparison between partial equivalent element circuit method (peec) and finite element method (fem). In: Industry Applications Conference, 1998. Thirty-Third IAS Annual Meeting. The 1998 IEEE, vol. 2, pp. 921–924. IEEE (1998)

21. Puigdellivol, O., Méresse, D., Le Menach, Y., Harmand, S., Wecxsteen, J.F.: Thermal topology optimization of a three-layer laminated busbar for power converters. IEEE Transactions on Power Electronics **32**(6), 4691–4699 (2017)
22. Schanen, J., Clavel, E., Roudet, J.: Modeling of low inductive busbar connections. IEEE Industry Applications Magazine **2**(5), 39–43 (1996)
23. Smirnova, L., Juntunen, R., Murashko, K., Musikka, T., Pyrhönen, J.: Thermal analysis of the laminated busbar system of a multilevel converter. IEEE Transactions on Power Electronics **31**(2), 1479–1488 (2016)
24. Sokolowski, J., Zolesio, J.P.: Introduction to shape optimization **16**, 5–12 (1992)
25. Stevanović, I., Cottet, D., Wider, B., Daroui, D., Ekman, J.: Modeling of large bus bars using peec method and circuit level simulators. In: Control and Modeling for Power Electronics (COMPEL), 2010 IEEE 12th Workshop on, pp. 1–7. IEEE (2010)
26. Svanberg, K.: The method of moving asymptotes- a new method for structural optimization. International journal for numerical methods in engineering **24**(2), 359–373 (1987)
27. Wen, H., Xiao, W.: Design and optimization of laminated busbar to reduce transient voltage spike. In: Industrial Electronics (ISIE), 2012 IEEE International Symposium on, pp. 1478–1483. IEEE (2012)

B

Appendix

C

Paper III: Efficient iterative solver for MMA subproblems in topology optimization with stress constraints

Efficient iterative solver for MMA subproblems in topology optimization with stress constraints

Erin Kuci[a,b], Christophe Geuzaine[b], Pierre Duysinx[a]

[a] *University of Liège, Department of Aerospace and Mechanical Engineering, Belgium*
[b] *University of Liège, Department of Electrical Engineering and Computer Science, Belgium*

Abstract

This paper presents a suitably preconditioned iterative solver for the interior point (IP) method, used to obtain the solution of large scale nonlinear optimization problems arising in the context of structural engineering. Such problems typically involve both a large number of design variables and a large number of restrictions such as stresses or slope constraints at each point of the region where it is applied. The preconditioner is based on successive modified partial Cholesky factorizations of the linearized Karush-Kuhn-Tucker (KKT) equations of the convex subproblems that approximate the original design problem. In addition, the preconditioner involves only matrix-vector products, avoiding hence the construction of the whole KKT matrix and its memory requirements are defined a-priori. The sparsity pattern of the sensitivity matrix of such problems is unfavorably low and determines the sparsity pattern of the KKT system of equations. A remedy which takes advantage of the local geometrical dependency of the stresses is proposed here, and leads to a much sparser truncated sensitivity matrix, which reduces the computational effort of the iterative solver. The performance of the preconditioned iterative method is demonstrated on classical stress constrained topology optimization benchmarks.

Keywords: topology optimization, stress constraints, sequential convex programming, primal-dual interior point method, iterative solver

Contents

Email address: Erin.Kuci@ulg.ac.be (Erin Kuci)

1. Introduction

Topology optimization has been an active research area since the seminal work of Bendsøe and Kikuchi in the late 1980's [1]. The design variables upon which density-based topology optimization acts represent the presence or absence of a specific material at each point of the region where it is applied. The method aims therefore at determining the material density field, [2, 3], that achieves specific design criteria while holding a number of design constraints fixed or within predefined limits. The physical behavior of the system is, in general, governed by partial differential equations (PDEs), set here as linear elasticity equations and discretized by means of, e.g., the finite element method (FEM). In engineering practice this may typically lead to several millions unknowns and to a computation time of several hours or even days. The PDE solution is included explicitly or implicitly as constraints in the optimization problem, and its solution for a given material density field is used to evaluate the performance functions.

Most of the developments in the field of structural engineering have been based on global design criteria such as compliance and have led to successful designs, [4, 5, 6]. Over the last ten years, however, a renewed interest has been directed towards topology optimization with local constraints, in particular stress constraints, [7, 8, 9], or more recently, slope constraints, [10]. Assuming a spatial discretization of the structure with N_e finite elements, a material density, noted ρ_e and defined in each finite element e, is determined so as to prevent failure in each point of the structure being optimized. The design problem reads,

$$(P)\begin{cases} \min\limits_{\boldsymbol{\rho}} & f_0(\boldsymbol{\rho},\boldsymbol{u}^\star) := \sum\limits_{e=1}^{N_e} \rho_e \\ s.t. & f_j(\boldsymbol{\rho},\boldsymbol{u}^\star) := \sigma_{vm,j}(\boldsymbol{u}^\star)/\bar{\sigma} - 1 \le 0,\ j = 1,\dots,n\cdot \\ & r(\boldsymbol{\rho},\boldsymbol{u}^\star,\bar{\boldsymbol{u}}) = 0,\ \forall \bar{\boldsymbol{u}} \in Z_u^0 \\ & 0 \le \rho_i \le 1,\ i = 1,\dots,n. \end{cases} \tag{1}$$

In (1), $\boldsymbol{u}^\star$ is the displacement field solution resulting from the linear elastic PDE problem written in a variational form through a residual, noted $r(\boldsymbol{\rho},\boldsymbol{u}^\star,\bar{\boldsymbol{u}}) = 0$, $\sigma_{vm,j}$ is the Von-Mises stress at the centroid of finite element j and $\bar{\sigma}$ is the maximum stress level that can be sustained by the material. The sensitivity matrix of (1) is denoted by,

$$S_{ji} = \frac{\mathrm{d}f_j}{\mathrm{d}\rho_i}(\boldsymbol{\rho},\boldsymbol{u}^\star). \tag{2}$$

It collects all performance functions (design constraints and objective function) derivatives with respect to the optimization variables. The matrix (2) is typically dense.

The optimization problems arising from the global design criteria are of the same complexity (in terms of the number of constraints) as the original minimum compliance problem. Conversely, topology optimization subjected to local stress constraints (1), or slope constraints,

leads to a large scale optimization problem with at least as many constraints as design variables. Therefore, the computational effort involved in repeated solutions of optimization problem (1) becomes comparable to the effort involved in repeated solutions of the PDEs, thus dominating the computational cost of the whole optimization iterative process.

Two paths have been followed over the years to make the solution of (1) able to tackle industrial designs. On the one hand, several reformulations of the local stress constrained problem, based on the behavior of the stresses, have been proposed to reduce the size of the problem, while still having a more or less precise control on the peak value of the stress criterion. Among the existing methods, the global stress constraint approach, [8], or its regional approach variant, form clusters of stresses, see for instance [11, 12, 13]. The computational effort has also been reduced by considering a global compliance constraint along with local stress constraints combined with an active-set strategy, [14, 15]. Much effort has been dedicated, on the other hand, to the design of efficient optimization algorithms for the solution of (1). The best approaches are based on the so-called sequential convex programming approach, [16], in which high precision local approximations of the performance functions, called subproblems, are built as convex and separable approximations by means of the gradient (2). Moreover, the approximated performance functions are explicit in terms of the design variables, and hence their evaluation does not require a FEM analysis. Such subproblems are solved efficiently thanks to dual maximization solvers, [17, 18, 19, 20], or interior point solvers, see for instance [21]. This paper aims at redesigning the linear algebraic core of the interior point optimization algorithm so as to solve (1) in a CPU time comparable to the global design criterion problem.

In the dual approach, a Lagrange multiplier is associated to each performance function of the subproblem. It is therefore transformed into a quasi unconstrained maximization problem which is solved in the space of the Lagrange multipliers, also called dual space, [19, 20]. The dimension of the dual space corresponds to the number of active constraints. It is, in particular for global design criteria, much smaller than the dimension of the design variables and leads therefore to an effective dual method. However, the dimensionality of the dual space tends to grow drastically for problems like (1) which involve local constraints and requires hence some adaptations.

IP methods, on the other hand, replace the inequality constrained subproblem by an equality constrained subproblem, called barrier subproblem, by introducing slack variables. Both the subproblem and the barrier subproblem have the same KKT optimality conditions and they have therefore the same optimizers. One should notice that the quasi unconstrained problem of the dual method can also be solved with an IP method. A Newton's method is, in general, used to obtain the design variables and the Lagrange variables for a sequence of linearized KKT systems of the barrier subproblems for a decreasing barrier parameter, see for instance [22, 23]. This system is however indefinite. It is therefore a common practice to perform block elimination and further reduce the system to the Schur complement. By doing so, the indefinite unreduced system is transformed into a symmetric positive definite system of normal equations. Any positive definite direct solver can hence be applied to the normal system of equations to obtain the optimal solution. However, turning to the point of view of algorithmic performance for large scale problems as (1), the CPU time spent in forming the system matrix of the normal equations could grow as fast as $O(n^3)$. Unfortunately, other strategies, e.g. [24], based on gradient projection, e.g. [25], would lead to the same pessimistic conclusion.

The replacement of the direct linear solver with an iterative method, e.g. preconditioned conjugate gradient (PCG), from the Krylov subspace family, [26], is hence considered in this paper. The convergence rate of Krylov-subspace iterative methods is however greatly influenced by the distribution of eigenvalues of the linearized KKT system matrix and its conditioning number. Unfortunately, the presence of barrier parameters and slack variables introduce an increasing ill-conditioning of the sequence of linearized systems along the iterations, from which only direct

C

solvers do not seem to suffer [27]. As far as the problem is feasible, the normal equations solved by a direct solver provide sufficiently accurate solutions. This property does not hold any more for iterative Krylov-subspace methods, and makes the solution of the system intractable unless suitably preconditioned, and at the expense of an increased number of iterations, [28, 29, 30].

In this paper, the preconditionner is designed as an approximated Cholesky factorization of only a few KKT matrix columns that contain the largest diagonal entries of the matrix, rather than the whole matrix. The method leads to a lower triangular matrix and a block diagonal matrix. The latter contains a Schur complement to which a sequence of successive partial Cholesky factorizations is applied so as to improve and preserve the quality of the preconditioner as the IP method unfolds. It has already been shown for the normal equations arising in linear and also quadratic programming, that the cluster of the largest eigenvalues of the system matrix can be captured by the use of partial Cholesky factorization of the matrix with static ordering, [31]. The application of the preconditioner brings therefore the highest eigenvalues down, and hence leads to a significant reduction in the condition number of the preconditioned matrix with respect to the unpreconditioned matrix.

The memory usage of the preconditioner is in general crucial. State-of-the-art preconditioners such as incomplete Cholesky factorizations, e.g. ILUT [26], try to limit the memory usage, but they may fail for general semi-positive definite (SPD) matrix, even though several strategies have been proposed to prevent the breakdown, e.g. [32]. Alternatively, approximate inverse preconditioners (AINV), [33], are successful approaches aiming at constructing a substitute for the inverse of the system matrix. After suitable permutations, the approximated inverse would be represented as the product of sparse triangular matrices, even the exact inverse is dense. In exact arithmetic, the preconditioner can be computed without breakdown for any SPD matrix. However, both ILUT and AINV struggle with memory requirements for dense matrices, which can grow linearly with the number of nonzero entries of the matrix for a zero fill-in variant of the Cholesky factorization. The preconditioner developed here avoids any excessive storage as the system matrix is only used to perform multiplication with a vector. Furthermore, our preconditioner requires memory bounded by the size of the problem rather then the number of nonzero entries of the system matrix.

In this paper, the preconditioner is further improved for the topology optimization subject to local stress constraints, by observing that the highest values of the stress sensitivity (2) with respect to a material density, defined at a given finite element, are located in a close vicinity of the element and tend rapidly to relatively small values for furthest elements. Using this practical observation, the density of the sensitivity matrix is significantly reduced by neglecting the elements located outside the neighborhood. The sensitivity matrix becomes sparse and it is hence used as an effective preconditioner of the system of normal KKT equations.

Two of the most classical topology optimization benchmarks with stress constraints are considered to assess the developments, Fig. 1. The optimized geometry of the two bar truss as well as the L-shape are obtained by using the IP solver which makes use of the proposed preconditioners. The computational cost of the overall solver tends to grow as $O(n^2)$ instead of $O(n^3)$.

The paper is organized as follows. In Section 2 we introduce the statement of a sequential convex programming approach based on a MMA approximation of the design problem (1), as well the relaxed KKT optimality conditions. Section 3 develops the Newton's based IP method and highlights the limitations of the solver in terms of computational effort. Section 4 details the preconditioner based on the partial Cholesky factorization of the linearized KKT system matrix. A sparse version of the former preconditioner is proposed in Section 5 based on a physical truncation of the original problem sensitivity matrix. Section 6 studies the spectral properties of both preconditioners so as to determine the permutation of rows, as well as the columns of the linearized KKT system of equations. Section 7 showcases the improvement of the numerical

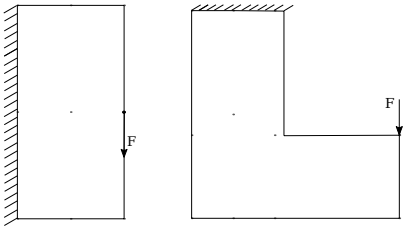

Figure 1: The two-bar truss, left, and the L-bracket, right, problems are considered in this paper in both a 2D and a 3D geometrical configuration. The Young modulus of the non void material, noted E_1, is set to unity, while the SIMP law is adopted for the intermediate material densities. The Poisson ratio, noted ν, is set to 0.3.

method of optimization problems subject to local stress constraints. The approach is applied to the classical stress-constrained topology design of two benchmarks: the two-bar truss and the L-bracket in 2D and 3D geometrical configuration.

2. Sequential convex programming approach

In this section, we adopt MMA approximation, available on `https://people.kth.se/~krille/mmagcmma.pdf`, to solve the original problem, see [34].

2.1. Successive convex approximations

Let us consider a sequence of approximated subproblems,

$$(\widetilde{P}^{(k)}) \begin{cases} \min\limits_{\boldsymbol{\rho}} & \widetilde{f}_0^{(k)}(\boldsymbol{\rho}) \\ s.t. & \widetilde{f}_j^{(k)}(\boldsymbol{\rho}) - b_i \leq 0,\ j = 1, \ldots, m \\ & \alpha_i \leq \rho_i \leq \beta_i,\ i = 1, \ldots, n, \end{cases} \tag{3}$$

valid in the vicinity of a design point $\boldsymbol{\rho}^{(k)}$. In (3), the approximated functions are convex, separable and explicit in the design variables $\boldsymbol{\rho}$. Their evaluation is then very efficient compared to the evaluation of the original functions of (1) as they do not require any FEM solution, [16, 18].

Using the sensitivity matrix (2) of the original problem at a given design point $\boldsymbol{\rho}^{(k)}$, the approximated functions $\widetilde{f}_j^{(k)}$ are obtained with either a first order or if available a second order Taylor series. The MMA approximation reads,

$$\widetilde{f}_j^{(k)}(\boldsymbol{\rho}) = r_j^{(k)} + \sum_{i=1}^{n} \Big(\frac{p_{ij}^{(k)}}{U_i^{(k)} - \rho_i} + \frac{q_{ij}^{(k)}}{\rho_i - L_i^{(k)}} \Big). \tag{4}$$

It is a first order and monotonous approximation of function f_j in (1) in terms of the intermediate variables $1/(U_i^{(k)} - \rho_i)$ and $1/(\rho_i - L_i^{(k)})$. The approximation (4) uses either a lower asymptote $L_i^{(k)}$ or an upper asymptote $U_i^{(k)}$ for each design variables ρ_i. Their values are obtained as

follows,

$$
\begin{aligned}
p_{ij}^{(k)} &= \max\Big\{0, S_{ji}(\boldsymbol{\rho}^{(k)}, \boldsymbol{u}^\star)\,(U_i^{(k)} - \rho_i^{(k)})^2\Big\},\\
q_{ij}^{(k)} &= \max\Big\{0, -S_{ji}(\boldsymbol{\rho}^{(k)}, \boldsymbol{u}^\star)\,(\rho_i^{(k)} - L_i^{(k)})^2\Big\},\\
r_j^{(k)} &= f_j(\boldsymbol{\rho}^{(k)}) - \sum_{i=1}^{n}\Big(\frac{p_{ij}^{(k)}}{U_i^{(k)} - \rho_i^{(k)}} + \frac{q_{ij}^{(k)}}{(\rho_i^{(k)} - L_i^{(k)})}\Big).
\end{aligned}
$$

They match the function value and its first derivative around the current point, i.e. $\widetilde{f}_j = f_j$ and $\mathrm{d}\widetilde{f}_j/\mathrm{d}\rho_i = S_{ji}$ at $\rho_i = \rho_i^{(k)}$.

The sensitivity matrix of the approximation (3) writes,

$$
\begin{aligned}
\widetilde{S}_{ji} &= \frac{\mathrm{d}\widetilde{f}_j^{(k)}}{\mathrm{d}\rho_i}(\boldsymbol{\rho}) = \frac{\mathrm{d}\widetilde{f}_{ji}}{\mathrm{d}\rho_i}(\rho_i) \qquad (5)\\
&= \begin{cases} S_{ji}(\boldsymbol{\rho}^{(k)}, \boldsymbol{u}^\star)\,\dfrac{(U_i^{(k)} - \rho_i^{(k)})^2}{(U_i^{(k)} - \rho_i)^2}, & \text{if } \dfrac{\mathrm{d}f_j}{\mathrm{d}\rho_i} > 0\\[2ex] S_{ji}(\boldsymbol{\rho}^{(k)}, \boldsymbol{u}^\star)\,\dfrac{(\rho_i^{(k)} - L_i^{(k)})^2}{(\rho_i - L_i^{(k)})^2}, & \text{if } \dfrac{\mathrm{d}f_j}{\mathrm{d}\rho_i} < 0 \end{cases}
\end{aligned}
$$

It preserves the sparsity pattern of the sensitivity matrix (2) of the original problem at a given iteration point $\boldsymbol{\rho}^{(k)}$. Hence if the original problem is dense, as it is the case for the topology optimization problem with stress constraints, the approximation of the problem will also be dense.

2.2. Optimality conditions of the convex approximations

To transform the inequality-constrained subproblem (3) into an equality-constrained problem at a given iteration point $\boldsymbol{\rho}^{(k)}$, let us introduce successively slack variables $\boldsymbol{s}$ and a barrier function $B(\boldsymbol{s}) := -\sum_{j=1}^{m}\log(s_j)$ so as to ensure $s_j > 0$, $j = 1, \ldots, m$,

$$
\begin{aligned}
\min_{\boldsymbol{\rho},\boldsymbol{s}} \quad & \widetilde{f}_0^{(k)}(\boldsymbol{\rho}) + \mu_p B(\boldsymbol{s})\\
s.t. \quad & \widetilde{f}_j^{(k)}(\boldsymbol{\rho}) + s_j = 0,\ j = 1, \ldots, m\\
& \rho_i^{min} \le \rho_i \le \rho_i^{max},\ i = 1, \ldots, n,
\end{aligned} \qquad (6)
$$

which depends on barrier parameter μ_p.

Minimization of (6) for a decreasing sequence of the barrier parameter $\mu_p \to 0$ results in a sequence of strictly feasible minimizers $\boldsymbol{\rho}^{(l)}$, such that the index $l = 0$ corresponds to the current point, i.e. $\boldsymbol{\rho}^{(l=0)} = \boldsymbol{\rho}^{(k)}$, and the actual minimizer $\boldsymbol{\rho}^\star = \boldsymbol{\rho}^{(k+1)}$, of the original subproblem (3), which turn out to be the solution of the original problem (1).

Introducing the Lagrangian function of (6),

$$
L_p(\boldsymbol{\rho}, \boldsymbol{s}, \boldsymbol{\lambda}) = \widetilde{f}_0^{(l)}(\boldsymbol{\rho}) + \mu_p^{(l)} B(\boldsymbol{s}) + \sum_{j=1}^{m}\lambda_j(\widetilde{f}_j^{(l)}(\boldsymbol{\rho}) + s_j),
$$

with λ_j the Lagrange multiplier (dual variables) for the j^{th} equality constraint, the first order optimality conditions of the barrier problem (6) are

$$\begin{aligned}
\frac{\partial \widetilde{f}_0^{(k)}}{\partial \rho_i}(\boldsymbol{\rho}^\star) + \sum_{j=1}^{m} \lambda_j^\star \frac{\partial \widetilde{f}_j^{(k)}}{\partial \rho_i}(\boldsymbol{\rho}^\star) = 0, \qquad & i = 1,\dots,n \qquad (\partial L_p/\partial \rho_i = 0) \qquad (7)\\
\lambda_j^\star s_j^\star - \mu_p^\star = 0, \qquad & j = 1,\dots,m \qquad (\partial L_p/\partial s_j = 0 : \text{compl. slackness})\\
\widetilde{f}_j^{(k)}(\boldsymbol{\rho}^\star) + s_j^\star = 0, \qquad & j = 1,\dots,m \qquad (\text{primal feasibility})\\
\alpha_i \le \rho_i \le \beta_i, \qquad & i = 1,\dots,n \qquad (\text{primal feasibility})\\
\lambda_j^\star \ge 0, \qquad & j = 1,\dots,m \qquad (\text{dual feasibility})
\end{aligned}$$

They consist of a nonlinear system respectively in the primal variables $\boldsymbol{\rho}$ and in the dual variables $\boldsymbol{\lambda}$. Subproblem (3) has exactly the same optimality conditions as the barrier subproblem (6). Therefore, solving (6) is also equivalent to solving the initial subproblem (3).

3. Newton-like interior point solver

A Newton's method is used to solve optimality conditions (7) for a given μ_p. Let l be the index of the iterative Newton Raphson process. Subsequent approximations of the solution $\boldsymbol{w}^{(l+1)} = \boldsymbol{w}^{(l)} + \gamma^{(l)}\Delta\boldsymbol{w}$, are obtained, by setting respectively $\boldsymbol{w}^{(l)} = (\boldsymbol{\rho}^{(l)}, \boldsymbol{s}^{(l)}, \boldsymbol{\lambda}^{(l)})$ for system (7) and using a linesearch technique to determine $\gamma^{(l)}$. We shall, for the sake of simplicity, omit the Newton's iteration index l.

Starting from an initial solution verifying (7), Newton's direction $\Delta\boldsymbol{w}$ for the barrier subproblem is obtained by solving the linearized KKT-system of $(n+m)$ equations, for a given barrier parameter μ,

$$\boldsymbol{\mathcal{A}}_{2\times 2}\,\Delta\boldsymbol{w} = \begin{pmatrix} \boldsymbol{D}_\rho & \widetilde{\boldsymbol{S}}^T \\ \widetilde{\boldsymbol{S}} & -\boldsymbol{D}_\lambda \end{pmatrix} \begin{pmatrix} \Delta\boldsymbol{\rho} \\ \Delta\boldsymbol{\lambda} \end{pmatrix} = \begin{pmatrix} -\widetilde{\boldsymbol{\delta}}_\rho \\ -\widetilde{\boldsymbol{\delta}}_\lambda \end{pmatrix} \qquad (8)$$

with

$$\begin{aligned}
\boldsymbol{D}_{\rho,i} &= \Psi_{ii} + \xi_i/(\rho_i - \alpha_i) + \eta_i/(\beta_i - \rho_i), && i = 1,\dots,n\\
\boldsymbol{D}_{\lambda,j} &= s_j/\lambda_j, && j = 1,\dots,m
\end{aligned}$$

and $(\widetilde{\boldsymbol{\delta}}_\rho, \widetilde{\boldsymbol{\delta}}_\lambda)^T$, the appropriately computed right-hand-side vectors, [35]. In (8), $\boldsymbol{\eta}$ and $\boldsymbol{\xi}$ are the Lagrange multipliers for the side constraints, while $\boldsymbol{\Psi}$ is the Hessian matrix, computed as the derivative of the MMA approximation (5) with respect to design variables $\boldsymbol{\rho}$. The square system matrix $\boldsymbol{\mathcal{A}}_{2\times 2}$ of size $(n+m)$ is symmetric and relatively sparse, since the upper left and lower right part are diagonal. Moreover, $\boldsymbol{\mathcal{A}}_{2\times 2}$ is indefinite, i.e. it has eigenvalues with both negative and positive real parts.

A practical alternative for sparse sensitivity matrix $\widetilde{\boldsymbol{S}}$, consists in reducing $\boldsymbol{\mathcal{A}}_{2\times 2}$ to a smaller system of normal equations. One can either write $\Delta\boldsymbol{\lambda}$ in terms of $\Delta\boldsymbol{\rho}$,

$$\Delta\boldsymbol{\lambda} = \boldsymbol{D}_\lambda^{-1}(\widetilde{\boldsymbol{\delta}}_\lambda + \widetilde{\boldsymbol{S}}\Delta\boldsymbol{\rho}),$$

and solve the reduced system of n equations and n unknowns, in terms of the primal variables,

$$\boldsymbol{\mathcal{A}}_{1\times 1,\rho}\Delta\boldsymbol{\rho} = \left(\boldsymbol{D}_\rho + \widetilde{\boldsymbol{S}}^T\boldsymbol{D}_\lambda^{-1}\widetilde{\boldsymbol{S}}\right)\Delta\boldsymbol{\rho} = -\widetilde{\boldsymbol{\delta}}_\rho - \widetilde{\boldsymbol{S}}^T\boldsymbol{D}_\lambda^{-1}\widetilde{\boldsymbol{\delta}}_\lambda, \qquad (9)$$

C

or equivalently, $\Delta\boldsymbol{\rho}$ can be expressed in terms of $\Delta\boldsymbol{\lambda}$ thanks to (8),

$$\Delta\boldsymbol{\rho} = -\boldsymbol{D}_\rho^{-1}(\widetilde{\boldsymbol{S}}^T\Delta\boldsymbol{\lambda} + \widetilde{\boldsymbol{\delta}}_\rho),$$

leading then to a system of m equations and m unknowns in the dual Lagrange variables,

$$\boldsymbol{\mathcal{A}}_{1\times1,\lambda}\Delta\boldsymbol{\lambda} = \left(\boldsymbol{D}_\lambda + \widetilde{\boldsymbol{S}}\boldsymbol{D}_\rho^{-1}\widetilde{\boldsymbol{S}}^T\right)\Delta\boldsymbol{\lambda} = \widetilde{\boldsymbol{\delta}}_{\lambda\rho} - \widetilde{\boldsymbol{S}}\boldsymbol{D}_\rho^{-1}\widetilde{\boldsymbol{\delta}}_\rho \tag{10}$$

to be solved. Both system matrices in (9) and in (10) are positive definite. The solution of system (9) is preferred when the number m of performance functions f_j exceeds the number of design variables n, $m > n$, otherwise the system (10) is preferable.

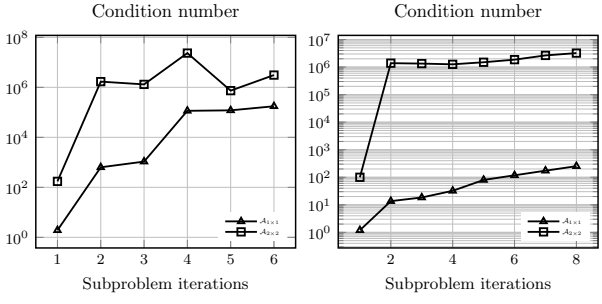

Figure 2: The Newton's system matrix $\boldsymbol{\mathcal{A}}_{1\times1,\rho}$ (equivalently $\boldsymbol{\mathcal{A}}_{1\times1,\lambda}$) of the normal equations remains better conditioned than the unreduced matrix $\boldsymbol{\mathcal{A}}_{2\times2}$ for the optimization problem with stress constraints applied to a L-bracket in both 2D (left) and 3D (right). The normal equations are then better suited for an iterative method.

Newton's method has been derived for the solution of the optimality conditions of the subproblem in the vicinity of a given primal point $\boldsymbol{\rho}^{(k)}$. A full rank system (8) of size $(n+m)$ with a symmetric and indefinite matrix $\boldsymbol{\mathcal{A}}_{2\times2}$ can be solved. Alternatively, the smaller positive definite systems either of size m to obtain the dual variables (10) or a system of size n to obtain the primal variables (9) can also be solved.

An effective method to solve either the full system or the normal equations is based on a direct solver [36], due their robustness. As the computational cost of a direct Cholesky decomposition of a dense system, e.g. of size N, grows as $O(N^3)$, direct solvers are rather preferred for small size problems, particularly in 2D. Moreover, as problems are nowadays formulated in 3D geometries, the use of direct methods impractical.

To this end, iterative Krylov-subspace methods [26] are usually preferred. However, their application to the symmetric indefinite system (8) here, requires some extra care about preconditioning, which is an open research field [37, 38]. We prefer to consider the positive definite system of normal equations (10), or equivalently (9) since they allow for a straightforward application of the preconditioned conjugate gradient method.

The sensitivity matrix (2) of the original constraints naturally appears in both systems and its sparsity pattern affects greatly the density of their respective system matrix. Furthermore,

the smaller systems of normal equations involve the product of the sensitivity matrix $\widetilde{\boldsymbol{S}}$ by its transpose $\widetilde{\boldsymbol{S}}^T$, $\widetilde{\boldsymbol{S}}\widetilde{\boldsymbol{S}}^T$, which requires $O(n^2m)$ operations for a dense $\widetilde{\boldsymbol{S}}$. They are thus intractable for large scale problems with a dense sensitivity matrix, which is the case for problems involving stress constraints, solved by a direct method. However, iterative solvers do not require the construction of the whole system matrix but only its application to a vector, making the solution of the normal equations more attractive.

The inverse of the diagonal scaling matrix, with entries λ_j/s_j, see (8), introduces ill-conditioning into the system. When the method converges to the optimal solution, the slack variables converge to their optimal values resulting in a spread of eigenvalues of the matrix from zero to infinity. Therefore, the condition number continuously increases throughout the Newton's iterations performed in a given subproblem for both $\boldsymbol{\mathcal{A}}_{1\times1,\rho}$ (equivalently $\boldsymbol{\mathcal{A}}_{1\times1,\lambda}$) and $\boldsymbol{\mathcal{A}}_{2\times2}$ but it reaches some constant value for the system matrix of normal equations, see Fig 2. Direct methods to solve (8) do not seem to suffer from this ill-conditioning of the matrix, [27]. However, the iterative Krylov-subspace methods are made intractable unless suitably preconditioned.

4. Partial Cholesky based preconditioned iterative method

We shall, without lack of generality, consider one particular system of normal equations, for instance (9), and denote the system matrix as $\boldsymbol{\mathcal{A}}_{1\times1}$. The treatment of any other Schur reduced system, such as (10), would be similar.

4.1. Cholesky-like factorization of the system matrix

The rows and columns of $\boldsymbol{\mathcal{A}}_{1\times1}$ are first reordered,

$$\boldsymbol{\mathcal{A}} = \boldsymbol{\Pi}^T\boldsymbol{\mathcal{A}}_{1\times1}\boldsymbol{\Pi} = \left(\begin{array}{c|c} \boldsymbol{\mathcal{A}}_{11} & \boldsymbol{\mathcal{A}}_{21}^T \\ \hline \boldsymbol{\mathcal{A}}_{21} & \boldsymbol{\mathcal{A}}_{22} \end{array}\right), \tag{11}$$

with a permutation matrix, $\boldsymbol{\Pi}$, that will be specified latter on, and the resulting symmetric matrix $\boldsymbol{\mathcal{A}}$ is partitioned into a small square block matrix, $\boldsymbol{\mathcal{A}}_{11}$ of size k, a larger square matrix $\boldsymbol{\mathcal{A}}_{22}$ of size $(n-k)$ and the remaining block $\boldsymbol{\mathcal{A}}_{21}$ of size $(n-k)\times k$.

The matrix in (11) is factorized,

$$\boldsymbol{\mathcal{A}} = \boldsymbol{L}\boldsymbol{D}\boldsymbol{L}^T \tag{12}$$

with

$$\boldsymbol{L} = \left(\begin{array}{c|c} \boldsymbol{L}_{11} & \boldsymbol{0} \\ \hline \boldsymbol{L}_{21} & \boldsymbol{I} \end{array}\right) = \left(\begin{array}{cc|ccccc} 1 & & & & & & \\ \times & 1 & & & & & \\ \hline \times & & 1 & & & & \\ \times & \times & & 1 & & & \\ \times & \times & & & 1 & & \\ \times & \times & & & & 1 & \\ \times & \times & & & & & 1 \\ \times & \times & & & & & \end{array}\right)$$

a lower triangular matrix, and

$$\boldsymbol{D} = \left(\begin{array}{c|c} \boldsymbol{D}_1 & \boldsymbol{0} \\ \hline \boldsymbol{0} & \boldsymbol{S}_A \end{array}\right) = \left(\begin{array}{c|cccccc} \times & & & & & & \\ & \times & & & & & \\ \hline & & \times & \times & \times & \times & \times & \times \\ & & \times & \times & \times & \times & \times & \times \\ & & \times & \times & \times & \times & \times & \times \\ & & \times & \times & \times & \times & \times & \times \\ & & \times & \times & \times & \times & \times & \times \\ & & \times & \times & \times & \times & \times & \times \end{array}\right)$$

a block diagonal matrix. The sparsity pattern of the resulting matrices, $\boldsymbol{L}_{11}$, $\boldsymbol{L}_{21}$ and $\boldsymbol{S}_A$ depends on the application, and are particularly dense for the system arising in topology optimization with stress constraints, as shown above where $\times$ denotes a nonzero entry.

In (12), the lower triangular matrix $\boldsymbol{L}_{11}$ and the diagonal matrix $\boldsymbol{D}_1$, both of size $k \times k$, are obtained at a negligible cost since k is small,

$$\boldsymbol{\mathcal{A}}_{11} = \boldsymbol{L}_{11}\boldsymbol{D}_1\boldsymbol{L}_{11}^T, \tag{13}$$

with the Cholesky factorization of $\boldsymbol{\mathcal{A}}_{11}$, while $\boldsymbol{L}_{21}$ is obtained by solving a $n-k$ linear system,

$$\boldsymbol{L}_{11}\boldsymbol{D}_1\boldsymbol{L}_{21}^T = \boldsymbol{\mathcal{A}}_{21}^T, \tag{14}$$

of size k. The Schur complement of $\boldsymbol{\mathcal{A}}_{22}$ in $\boldsymbol{\mathcal{A}}$,

$$\boldsymbol{S}_A = \boldsymbol{\mathcal{A}}_{22} - \boldsymbol{\mathcal{A}}_{21}\boldsymbol{\mathcal{A}}_{11}^{-1}\boldsymbol{\mathcal{A}}_{21}^T,$$

is computed equivalently as,

$$\boldsymbol{S}_A = \boldsymbol{\mathcal{A}}_{22} - \boldsymbol{L}_{21}\boldsymbol{D}_1\boldsymbol{L}_{21}^T. \tag{15}$$

The resulting square and symmetric block matrix (15),

$$\boldsymbol{\mathcal{S}}_A = \left(\begin{array}{c|c} \boldsymbol{\mathcal{S}}_{A,11} & \boldsymbol{\mathcal{S}}_{A,21}^T \\ \hline \boldsymbol{\mathcal{S}}_{A,21} & \boldsymbol{\mathcal{S}}_{A,22} \end{array}\right), \tag{16}$$

of size $(n-k)$, can be partitioned similarly to $\boldsymbol{\mathcal{A}}$ and then factorized,

$$\boldsymbol{\mathcal{S}}_A = \boldsymbol{L}^{(1)}\boldsymbol{D}^{(1)}\boldsymbol{L}^{(1\,T)} \tag{17}$$

with the following matrices

$$\boldsymbol{L}^{(1)} = \left(\begin{array}{c|c} \boldsymbol{L}_{11}^{(1)} & \boldsymbol{0}^{(1)} \\ \hline \boldsymbol{L}_{21}^{(1)} & \boldsymbol{I}^{(1)} \end{array}\right) = \left(\begin{array}{cc|cccc} 1 & & & & & \\ \times & 1 & & & & \\ \hline \times & & 1 & & & \\ \times & \times & & 1 & & \\ \times & \times & & & 1 & \\ \times & \times & & & & 1 \end{array}\right)$$

a lower triangular matrix of size $(n-k) \times k$, and

$$\boldsymbol{D}^{(1)} = \left(\begin{array}{c|c} \boldsymbol{D}_1^{(1)} & \boldsymbol{0} \\ \hline \boldsymbol{0} & \boldsymbol{S}_A^{(1)} \end{array}\right) = \left(\begin{array}{cc|cccc} \times & & & & & \\ & \times & & & & \\ \hline & & \times & \times & \times & \times \\ & & \times & \times & \times & \times \\ & & \times & \times & \times & \times \\ & & \times & \times & \times & \times \end{array}\right)$$

a block diagonal matrix of size $(n-k)\times(n-k)$.

The resulting lower triangular matrix is inserted into $\boldsymbol{L}$,

$$\boldsymbol{L}=\left(\begin{array}{c|cc} \boldsymbol{L}_{11} & \boldsymbol{0} & \boldsymbol{0} \\ \hline & \boldsymbol{L}_{11}^{(1)} & \boldsymbol{0}^{(1)} \\ \boldsymbol{L}_{21} & \boldsymbol{L}_{21}^{(1)} & \boldsymbol{I}^{(1)} \end{array}\right)=\left(\begin{array}{c|cc|c} 1 & & & \\ \times & 1 & & \\ \hline \times & & 1 & \\ \times & \times & \times & 1 \\ \hline \times & \times & \times & & 1 \\ \times & \times & \times & \times & & 1 \\ \times & \times & \times & \times & & & 1 \\ \times & \times & \times & \times & & & & 1 \end{array}\right)$$

while the diagonal matrix, $\boldsymbol{D}^{(1)}$, is inserted into $\boldsymbol{D}$,

$$\boldsymbol{D}=\left(\begin{array}{c|cc} \boldsymbol{D}_1 & \boldsymbol{0} & \boldsymbol{0} \\ \hline \boldsymbol{0} & \boldsymbol{D}_1^{(1)} & \boldsymbol{0}^{(1)} \\ \boldsymbol{0} & \boldsymbol{0}^{(1)} & \boldsymbol{S}_A^{(1)} \end{array}\right)=\left(\begin{array}{c|cc|cccc} \times & & & & & & \\ & \times & & & & & \\ \hline & & \times & & & & \\ & & & \times & & & \\ \hline & & & & \times & \times & \times & \times \\ & & & & \times & \times & \times & \times \\ & & & & \times & \times & \times & \times \\ & & & & \times & \times & \times & \times \end{array}\right).$$

The resulting Schur complement $\boldsymbol{S}_A^{(1)}$ is further partitioned, similarly to (16), and the resulting matrix is factorized. Applying this procedure, N_p times in a row, to a small block of size k much smaller than the size n of the matrix $\boldsymbol{\mathcal{A}}$ allows to obtain the lower triangular $\boldsymbol{L}$ and the block diagonal matrix $\boldsymbol{D}$.

4.2. Limited-memory Cholesky-like preconditioner

A preconditioner,

$$\begin{aligned}\boldsymbol{\mathcal{P}} &= \begin{pmatrix} \boldsymbol{L}_{11} & \boldsymbol{0} \\ \boldsymbol{L}_{21} & \boldsymbol{I} \end{pmatrix}\begin{pmatrix} \boldsymbol{D}_1 & \boldsymbol{0} \\ \boldsymbol{0} & \bar{\boldsymbol{S}}_A \end{pmatrix}\begin{pmatrix} \boldsymbol{L}_{11}^T & \boldsymbol{L}_{21}^T \\ \boldsymbol{0} & \boldsymbol{I} \end{pmatrix} \\ &= \boldsymbol{L}\bar{\boldsymbol{D}}\boldsymbol{L}^T\end{aligned} \tag{18}$$

is derived from (12) by approximating the large block of Schur complement, $\boldsymbol{S}_A$ appearing in the block diagonal matrix (12), by $\bar{\boldsymbol{S}}_A$. Classically, $\boldsymbol{S}_A$ is replaced by its diagonal, $\bar{\boldsymbol{S}}_A = \mathrm{diag}(\boldsymbol{S}_A)$, [31]. This approach requires forming only the diagonal entries of $\boldsymbol{\mathcal{A}}$, and computing the diagonal of $\boldsymbol{L}_{21}\boldsymbol{D}_1\boldsymbol{L}_{21}^T$ which amounts to scaling $\boldsymbol{L}_{21}^T$ by $\boldsymbol{D}_1$ and computing $n-k$ scalar products between vectors of dimension k. Although the diagonal approximation of the Schur complement is advantageous in terms of memory requirements, it has been shown that it is not preferable for a dense Schur complement, [39]. The quality of the resulting preconditioner built with this approach is quickly degraded through the successive linear systems solutions, leading therefore to an increase of iterations required by the iterative solver to reach the desired convergence criterion.

In order to improve the quality of the preconditioner, N_p successive partial Cholesky decompositions are applied to the sequence of Schur complement block matrices of decreasing size as explained in previous section. The Schur complement obtained at the last iteration of the process is then approximated by its diagonal entries, according to Algorithm 1. The method requires

C

the initial blocks $\boldsymbol{\mathcal{A}}_{11}$ and $\boldsymbol{\mathcal{A}}_{21}$ of the initial partition of the matrix $\boldsymbol{\mathcal{A}}$, and avoids therefore the construction of the whole system matrix $\boldsymbol{\mathcal{A}}$.

The method produces the block diagonal matrix, $\boldsymbol{D}$, and the lower triangular matrix, $\boldsymbol{L}$. The LDL^T factorization is applied only to small systems of size $k \times k$ and is thus pretty fast. Furthermore, the Schur complement, $\boldsymbol{S}_A^{(l)}$, is computed for a sequence of decreasing size through the iterations.

However, the unfavorable sparsity pattern of the sensitivity matrix $\widetilde{\boldsymbol{S}}$ makes $\boldsymbol{\mathcal{A}}$ dense, and therefore also the lower triangular matrix $\boldsymbol{L}$, Fig. 7, leading to a dense representation of the inverse of preconditioner (18). The construction of (18) becomes then too expensive for practical applications. Thus, an approximate constraint preconditioner which rather uses a sparse approximation, $\bar{\boldsymbol{S}}$, of the sensitivity matrix instead of the highly dense matrix $\widetilde{\boldsymbol{S}}$ is derived here using physics constructions.

The construction of both preconditioner (18) is breakdown-free and the maximum storage is known a-priori for a dense matrix as it can be controlled by the number k of columns which are factorized.

Algorithm 1: Block-Cholesky preconditioner, BCP(k, N_p)

while *not converged* **do**
- `// Sequential construction of the preconditioner,`
- `// given` $(\boldsymbol{\mathcal{A}}_{11}^{(0)}, \boldsymbol{\mathcal{A}}_{21}^{(0)})$ `of (11),` k `and` N_p
- **for** $l = 0 : N_p - 1$
  - `// Partial factorization of` $(\boldsymbol{\mathcal{A}}_{11}^{(l)}, \boldsymbol{\mathcal{A}}_{21}^{(l)})$
  - Compute, $\boldsymbol{\mathcal{A}}_{11}^{(l)} = \boldsymbol{L}_{11}^{(l)} \boldsymbol{D}_1^{(l)} \boldsymbol{L}_{11}^{(l\,T)}$
    - $\rightarrow$ discard $\boldsymbol{\mathcal{A}}_{11}^{(l)}$
  - Solve, $\boldsymbol{L}_{11}^{(l)} \boldsymbol{D}_1^{(l)} \boldsymbol{L}_{21}^{(l\,T)} = \boldsymbol{\mathcal{A}}_{21}^{(l\,T)}$
    - $\rightarrow$ discard $\boldsymbol{\mathcal{A}}_{21}^{(l)}$
  - `// Assemble in the global matrices`
  - $\boldsymbol{D} \leftarrow \boldsymbol{D}_1^{(l)}$
  - $\boldsymbol{L} \leftarrow (\boldsymbol{L}_{11}^{(l)}, \boldsymbol{L}_{21}^{(l)})$
  - `// Generate the remaining block (Schur)`
  - $\boldsymbol{S}_A^{(l)} = \boldsymbol{\mathcal{A}}_{22}^{(l)} - \boldsymbol{L}_{21}^{(l)} \boldsymbol{D}_1^{(l)} \boldsymbol{L}_{21}^{(l\,T)}$
  - `// Partition` $\boldsymbol{S}_A^{(l)}$ `of size` $(n - l * k)$ `into block matrices`
  - $\boldsymbol{\mathcal{A}}_{11}^{(l+1)} \leftarrow \boldsymbol{S}_{A,11}^{(l)}$, of size $k \times k$
  - $\boldsymbol{\mathcal{A}}_{21}^{(l+1)} \leftarrow \boldsymbol{S}_{A,21}^{(l)}$, of size $(n - l * k) \times k$
  - $\boldsymbol{\mathcal{A}}_{22}^{(l+1)} \leftarrow \boldsymbol{S}_{A,22}^{(l)}$, of size $(n - l * k) \times (n - l * k)$
- **end**
- `// Diagonal approximation of the last block`
- $\boldsymbol{S}_A^{(l+1)} = \mathrm{diag}(\boldsymbol{\mathcal{A}}_{22}^{(l+1)}) - \mathrm{diag}\boldsymbol{L}_{21}^{(l+1)} \boldsymbol{D}_1 \boldsymbol{L}_{21}^{((l+)1\,T)}$
- Let $\boldsymbol{\mathcal{P}}$ take the form (18), with the computed $\boldsymbol{D}$ and $\boldsymbol{L}$.

end

5. Sparse approximation of the preconditioner

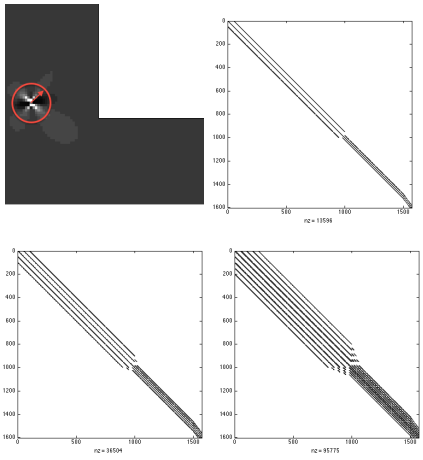

Figure 3: The topology optimization of a L-bracket with stress constraints is considered, (1). The first component of $\sigma_j(\frac{\mathrm{d}\boldsymbol{u}}{\mathrm{d}\rho_i})$ appearing in sensitivity matrix (2) is shown in top left at a given finite element j. The highest values of sensitivity are clustered in the vicinity of the element j, while the sensitivity decreases significantly for the farthest elements. Sensitivity matrix $\boldsymbol{S}_{ji}$ is successively truncated for various local neighborhood (20) radius values, leading hence to sparse approximations, $\bar{\boldsymbol{S}}_{ji}$, of the original sensitivity matrix.

One can further improve the effectiveness of the approach if it would be possible to generate a sparse sensitivity matrix while forming the approximation of the sensitivity matrix. In many design optimization problems with constraints associated to each finite element of a mesh, one observes that the sensitivity at a given finite element j mainly depends on the finite elements located in the closest vicinity of that element, see Fig. 3. This can be motivated as follows. First of all, St Venant principle tells us that modifying the local element density impact stresses only in its vicinity. Secondly, modification of density has the same effect as a rigid body motion far from the FE. Therefore, it leads to no stress modification for the farthest elements from the FE.

A truncated sensitivity matrix for stress constraints,

$$\bar{S}_{ji} = \frac{p-q}{\rho_j}\sigma_{vm,j}(\boldsymbol{u})\ \delta_{i,j} + \frac{1}{\sigma_{vm,j}}\boldsymbol{\sigma}_j^T(\boldsymbol{u})\ \boldsymbol{V}\ \bar{\sigma}_j^T(\frac{\mathrm{d}\boldsymbol{u}}{\mathrm{d}\rho_i}), \tag{19}$$

with

$$\bar{\sigma}_j^T(\frac{\mathrm{d}\boldsymbol{u}}{\mathrm{d}\rho_i}) = \sum_{i\in N_j}\sigma_j^T(\frac{\mathrm{d}\boldsymbol{u}}{\mathrm{d}\rho_i})$$

C

the truncated stress field which depends on the derivative of the displacement field. A typical approximation of the stress field is obtained by keeping only the elements i located into the closest neighborhood N_j of element j. For sake of simplicity, let us consider a circular neighborhood of radius r,

$$N_j = \big\{ i : \mathrm{d}(j,i) \leq r \big\}. \tag{20}$$

In (20), $\mathrm{d}(j,i)$ is the distance between the centroids of element j and i. Practically, the radius r can be easily determined such that the relative L_2-error between the approximated and the exact sensitivity matrices is under a given value, Fig. 3. The resulting truncated sensitivity matrix is obtained by setting to zero the components of the original matrix related to the variables outside the ball. It has therefore a much sparser pattern than the original sensitivity matrix.

Let us consider

$$\bar{\boldsymbol{\mathcal{A}}}_{1\times 1} = \boldsymbol{D}_\rho + \bar{\boldsymbol{S}}^T \boldsymbol{D}_\lambda^{-1} \bar{\boldsymbol{S}}, \tag{21}$$

a sparse approximation of $\boldsymbol{\mathcal{A}}_{1\times 1}$, obtained with the truncated and sparse sensitivity matrix $\bar{\boldsymbol{S}}$. One can hence derive a sparse preconditioner

$$\begin{aligned} \bar{\boldsymbol{\mathcal{P}}} &= \begin{pmatrix} \bar{\boldsymbol{L}}_{11} & \boldsymbol{0} \\ \bar{\boldsymbol{L}}_{21} & \boldsymbol{I} \end{pmatrix} \begin{pmatrix} \bar{\boldsymbol{D}}_1 & \boldsymbol{0} \\ \boldsymbol{0} & \bar{\boldsymbol{S}}_A \end{pmatrix} \begin{pmatrix} \bar{\boldsymbol{L}}_{11}^T & \bar{\boldsymbol{L}}_{21}^T \\ \boldsymbol{0} & \boldsymbol{I} \end{pmatrix} \\ &= \bar{\boldsymbol{L}} \bar{\boldsymbol{D}} \bar{\boldsymbol{L}}^T. \end{aligned} \tag{22}$$

In (22), $\bar{\boldsymbol{L}}_{11}$ and $\bar{\boldsymbol{D}}_1$ are obtained at a negligible cost by applying a Cholesky factorization to the small square matrix $\bar{\boldsymbol{\mathcal{A}}}_{11}$ of size k, while $\bar{\boldsymbol{L}}_{21}$ requires the solution of $n-k$ sparse linear systems of size k for a sequence of N_p block Cholesky factorizations, see Algorithm 1. The sparsity pattern of the approximated lower triangular matrix $\bar{\boldsymbol{L}}$ is illustrated in Fig. (7). For practical problems in which a truncated sensitivity matrix $\bar{\boldsymbol{G}}$ does not exist, $\bar{\boldsymbol{L}}_{11}$ and $\bar{\boldsymbol{D}}_1$ can be obtained through an incomplete Cholesky factorization to $\boldsymbol{\mathcal{A}}_{11}$. The construction of the sparse preconditioner (22) is breakdown-free and the maximum storage is significantly lowered compared to the dense matrix case.

6. Spectral-based permutations of the system matrix

Let us drive now a spectral analysis of the preconditioned matrix $\boldsymbol{\mathcal{P}}^{-1}\boldsymbol{\mathcal{A}}$, in order to derive an heuristic method for the construction of the permutation matrix $\boldsymbol{\Pi}$ appearing in (11). One writes,

$$\boldsymbol{\mathcal{P}}(\boldsymbol{\mathcal{P}}^{-1}\boldsymbol{\mathcal{A}}) = \boldsymbol{\mathcal{A}},$$

which is equivalent to a block diagonal matrix,

$$\boldsymbol{L}^T(\boldsymbol{\mathcal{P}}^{-1}\boldsymbol{\mathcal{A}})\boldsymbol{L}^{-T} = \begin{pmatrix} \boldsymbol{I} & \boldsymbol{0} \\ \boldsymbol{0} & \bar{\boldsymbol{S}}_A^{-1}\boldsymbol{S}_A \end{pmatrix} \tag{23}$$

obtained by using successively (12) and (18). In (23), the preconditioned matrix, $\boldsymbol{\mathcal{P}}^{-1}\boldsymbol{\mathcal{A}}$, is similar to a block diagonal matrix which has k eigenvalues equal to one, while the remainder are equal to the eigenvalues of $\bar{\boldsymbol{S}}_A^{-1}\boldsymbol{S}_A$. Let γ be an eigenvalue of $\bar{\boldsymbol{S}}_A^{-1}\boldsymbol{S}_A$, and $\boldsymbol{v}$ the corresponding eigenvector,

$$(\bar{\boldsymbol{S}}_A^{-1}\boldsymbol{S}_A)\boldsymbol{v} = \gamma\boldsymbol{v}$$

The eigenvalue γ is also given by

$$\gamma = \frac{\boldsymbol{v}^T\boldsymbol{S}_A\boldsymbol{v}}{\boldsymbol{v}^T\bar{\boldsymbol{S}}_A\boldsymbol{v}}.$$

If $\gamma_m(.)$ and $\gamma_M(.)$ stand respectively for the minimum and the maximum eigenvalue of the eigenvalue γ, one has

$$\frac{\gamma_m(\boldsymbol{S}_A)}{\gamma_M(\bar{\boldsymbol{S}}_{\boldsymbol{\mathcal{A}}})} \leq \gamma \leq \frac{\gamma_M(\boldsymbol{S}_A)}{\gamma_m(\bar{\boldsymbol{S}}_A)}$$

which can be further transformed as

$$\frac{\gamma_m(\boldsymbol{\mathcal{A}})}{\gamma_M(\bar{\boldsymbol{S}}_{\boldsymbol{\mathcal{A}}})} \leq \gamma \leq \frac{\gamma_M(\boldsymbol{\mathcal{A}}_{22})}{\gamma_m(\bar{\boldsymbol{S}}_A)} \tag{24}$$

by using the properties of the Schur complement, see for instance [40]. Furthermore, as $\boldsymbol{\mathcal{P}}^{-1}\boldsymbol{\mathcal{A}}$ is (semi) positive definite, the trace of $\boldsymbol{\mathcal{P}}^{-1}\boldsymbol{\mathcal{A}}$ is,

$$\mathrm{tr}(\boldsymbol{\mathcal{P}}^{-1}\boldsymbol{\mathcal{A}}) = \sum_{i=1}^{n} \gamma_i(\boldsymbol{\mathcal{P}}^{-1}\boldsymbol{\mathcal{A}}), \tag{25}$$

with $\gamma_i(\boldsymbol{\mathcal{P}}^{-1}\boldsymbol{\mathcal{A}})$, the i^{th} eigenvalue of $\boldsymbol{\mathcal{P}}^{-1}\boldsymbol{\mathcal{A}}$. Therefore,

$$\begin{aligned} \gamma_M(\boldsymbol{\mathcal{P}}^{-1}\boldsymbol{\mathcal{A}}) &\leq \mathrm{tr}(\boldsymbol{\mathcal{I}}) + \mathrm{tr}(\bar{\boldsymbol{S}}_A^{-1}\boldsymbol{S}_A) \\ &\leq k + \mathrm{tr}(\bar{\boldsymbol{S}}_A^{-1}\boldsymbol{\mathcal{A}}_{22}) \end{aligned} \tag{26}$$

by using (23). It appears respectively from (24) and (26), that the lower and upper bounds of the eigenvalues of $\boldsymbol{\mathcal{P}}^{-1}\boldsymbol{\mathcal{A}}$ are given by the minimum eigenvalue of $\boldsymbol{\mathcal{A}}$, $\gamma_m(\boldsymbol{\mathcal{A}})$ and the trace of $\boldsymbol{\mathcal{A}}_{22}$, $\mathrm{tr}(\boldsymbol{\mathcal{A}}_{22})$. Reordering the rows and columns of $\boldsymbol{\mathcal{A}}$ in such a way that the k largest diagonal entries of $\boldsymbol{\mathcal{A}}$ are put in the first block, $\boldsymbol{\mathcal{A}}_{11}$ seems a good heuristic, which helps to greatly reduce $\mathrm{tr}(\boldsymbol{\mathcal{A}}_{22})$. Furthermore, $\gamma_m(\boldsymbol{\mathcal{P}}^{-1}\boldsymbol{\mathcal{A}})$ can be increased (shifted away from zero) by regularizing the matrix $\boldsymbol{\mathcal{A}}$, as $\boldsymbol{\mathcal{A}} := \boldsymbol{\mathcal{A}} + \sigma\boldsymbol{I}$, for some small shift σ.

7. Numerical examples

In this section we illustrate the numerical behavior of both the partial Cholesky-like preconditioner (18), as well as the sparse preconditioner (22). We analyze their performance in solving MMA subproblems of the topology optimization problem with local stress constraints (1). The properties of the algorithm are illustrated in solving three topology optimization benchmarks: a L-bracket, a two-bar truss and the MBB beam submitted to stress constraints. In a second set of experiments we applied both preconditioners to solve the stress constrained optimization problem of a cantilever beam as well as an MBB beam. In the following, we consider the linear system of normal equations (10) which arise in the IP iterative method and we set the tolerance of the solver as $|\boldsymbol{\mathcal{A}}\Delta w - \delta|_2 \leq 10^{-7}\,|\delta|_2$, with a null initial guess. For all numerical applications, the reference solution performance will be based on a direct LU factorization of the linearized KKT systems which arise for MMA subproblem. We have used a MacBookPro laptop computer with a 2.3 GHz (four cores) processor and 8 GB of RAM. We have implemented all the iterative solvers in Matlab version 2015b.

7.1. Experiments with the design of a L-bracket

The geometry of the L-bracket test bench is provided in Fig. 1. The material data are normalized: the Young modulus, E, is set to $1(N/m^2)$, Poisson's ratio, ν, is set to 0.3, and the material density is set to one. The problem statement (1) is the following: minimize the structural volume subjected to local stress constraints in each finite element. The Von-Mises

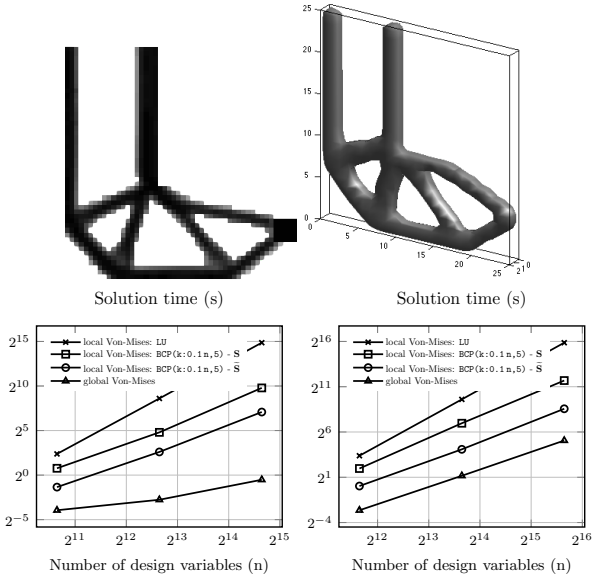

Figure 4: Top: The optimized topology of a L-bracket is obtained by solving the stress constraints problem, (1), in both 2D and 3D geometrical configurations. The normal system of equations of the IP method is solved equivalently with a conjugate gradient method preconditioned with the block-Cholesky preconditioner, see Algorithm 1. We consider 10% of the system columns by setting k to $0.1\,n$ and $N_p = 5$ successive block decompositions. Both the dense preconditioner (18) (based on the sensitivity matrix $\boldsymbol{S}$, and noted *BCP(k:0.1n,5) - $\boldsymbol{S}$)*, as well as the sparse preconditioner (22) (based on the truncated and sparse sensitivity matrix $\bar{S}$, in which $r = 2r_f$, and noted *BCP(k:0.1n,5) - $\bar{S}$)*, have been tested and lead to the same numerical results. Bottom: The CPU-time spent in the solution of the linear system in a 2D case, left as well as in a 3D case, right, grows as n^2. For this particular problem, we can expect in average a reduction of time by a factor of 256, i.e. a reduction by two order of magnitudes.

stresses are evaluated in the Q4 finite element centroids. The stress limit is arbitrarily set to $1(N/m^2)$.

We investigate the solution performance for a number of design variables n equal to the number of restrictions m, ranging from 2^{11} to 2^{15}. The MMA subproblem (3) is built using the sensitivity matrix (2). In order to make use of the sparse preconditioner (22), we obtain the physical truncation of sensitivity (19), by neglecting the elements located outside the circular neighborhood (20) of radius r. It is set as two times larger than the density filter radius r_f. The increase of r in this particular example doesn't change the optimized topology.

The optimized topologies are obtained by setting the parameter k (number of KKT matrix columns) of both preconditioners to 10% of n, see Fig. 4. The execution time includes also the time of building the preconditioner. We also compared the behavior of PCG with that of direct LU solver. The CPU-time spent in the solution of the linear system in a 2D case, as well as in a 3D case, grows as n^2. Both preconditioned iterative solvers are better than the LU based direct solver which grows as n^3. However, the preconditioner based on the sparse truncated sensitivity matrix allows to get a CPU time closer to the one involved in an equivalent global design criterion, such as the p-norm of the Von-Mises, see [8]. In all the geometrical configurations the material distribution is similar for all obtained results in this paper, and in the 2D case in a very good agreement with results of the reference [11].

The main computational cost for both preconditioners comes from the building of the diagonal of the system matrix and its k first columns. The parameter k is hence chosen so as to decrease that time but it should be large enough to preserve the good quality of the preconditioner. It should be noted that these operations can be significantly simplified if the system matrix can be accessed by rows.

In the following, the influence of the k parameter is investigated on the preconditioning of a KKT system matrix. First, statistics of the dense preconditioner (18) runs are reported in Fig. 5. Along the subproblem iterations, the eigenvalue bounds are stable and the conditioning number of the preconditioned matrix is much lower than the one of the real one. The low condition number drastically reduces the PCG effort. The condition number of the preconditioned KKT matrix can be finely tuned by the number k of columns used in the partial Cholesky factorization. As mentioned in (24), an increase of k allows to reduce the gap between the lower and the upper bounds of eigenvalues. It follows a considerable reduction of the number of iterations performed by the iterative solver, PCG, to reach the prescribed tolerance.

We study, on the other hand, the use of truncated and sparse sensitivity matrix (19). In addition, we investigate the influence the neighborhood radius r on the conditioning of the preconditioned KKT matrix by means of sparse truncated preconditioner (22), see Fig. 6. In this case, the number of columns k used in the partial Cholesky factorization of $\boldsymbol{\mathcal{A}}_{1\times 1}$ has a little influence in the maximum eigenvalue of $\boldsymbol{\mathcal{P}}^{-1}\boldsymbol{\mathcal{A}}$. However, the eigenvalue bounds of the sparse preconditioner (22) greatly depend on the radius r of the circular neighborhood (20) used to make the sensitivity matrix of the problem sparse. However, an increase of the neighborhood radius r, has a greater effect as the truncated sensitivity matrix $\bar{\boldsymbol{S}}$ becomes closer to $\tilde{\boldsymbol{S}}$.

The KKT system arising for the L-bracket is shown in Fig. 7 for a number of block set to one. As r is increased, the triangular matrix $\tilde{\boldsymbol{L}}$ converges to $\boldsymbol{L}$, hence the sparse preconditioner behaves similarly to the dense preconditioner. However, we noticed that the PCG iterations become more costly.

For this particular problem, we can expect in average a reduction of time by a factor of 256, i.e. a reduction by two order of magnitudes.

C

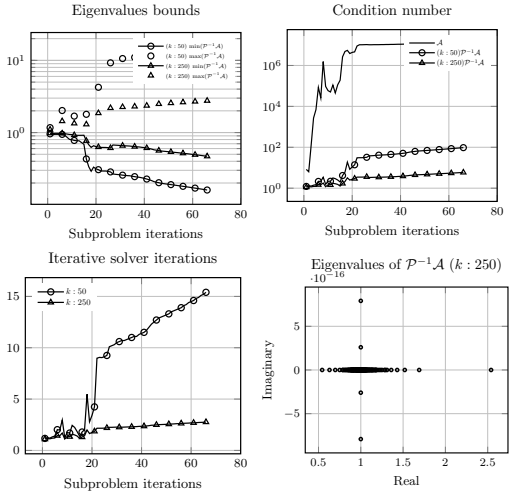

Figure 5: A sequence of linear systems is solved within a given MMA subproblem arising from the topology optimization of a L-bracket submitted to stress constraints. The system matrix has been preconditioned by (18) with k set to 50 and 250. As already mentioned, an increase of the parameter k (number of columns of $\boldsymbol{\mathcal{A}}$ used in the Cholesky factorization) allows to reduce the maximum eigenvalue of $\boldsymbol{\mathcal{P}}^{-1}\boldsymbol{\mathcal{A}}$, and helps for a better clustering of the eigenvalues around one, leading hence to a further decrease of the condition number of $\boldsymbol{\mathcal{P}}^{-1}\boldsymbol{\mathcal{A}}$. The iterative solver, PCG, performs then fewer iterations.

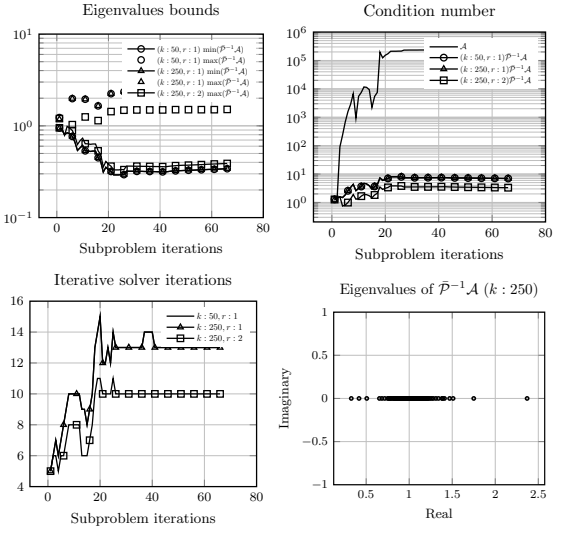

Figure 6: The sparse preconditioner (22) is used in the solution of a sequence of linear systems which arise within a given MMA subproblem of problem (1) applied to the design of a L-bracket. The number of columns k used in the partial Cholesky factorization of $\bar{\boldsymbol{A}}_{1\times 1}$ has a little influence in the maximum eigenvalue of $\boldsymbol{\mathcal{P}}^{-1}\boldsymbol{\mathcal{A}}$. However, an increase of the neighborhood radius r, has a greater effect as the truncated sensitivity matrix $\bar{\boldsymbol{S}}$ becomes closer to $\boldsymbol{S}$. The iterative solver, PCG, converges therefore to the desired tolerance in fewer iterations.

C

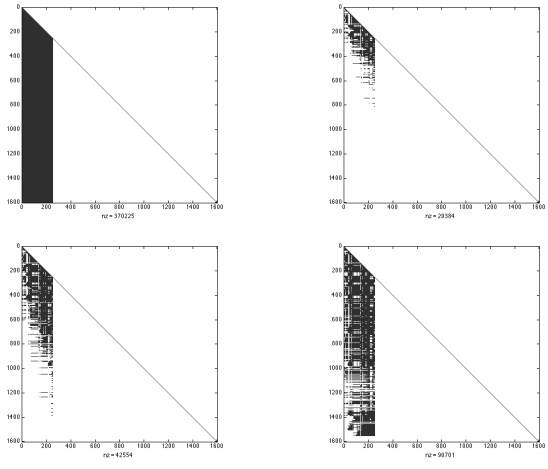

Figure 7: A given MMA subproblem arising in the topology optimization of a L-bracket with stress constraints is considered. The preconditioner (18), top left, has a fully dense lower triangular part $\boldsymbol{L}$, fixed by the dense sensitivity matrix $\bar{\boldsymbol{S}}$, while there is some freedom in the control of the density of the lower triangular matrix, $\bar{\boldsymbol{L}}$, of the sparse preconditioner (22) through the radius r of the neighborhood (20). As r is increased, the truncated sensitivity matrix, $\tilde{\boldsymbol{S}}$, becomes denser and hence the resulting preconditioner too.

7.2. Experiments with the design of a two-bar truss and MBB beam problems

In the final experiments we consider sequences of the normal equations (10) arising in the solution of MMA subproblems of two other classical topology optimization benchmarks which we solve with stress constraints. For each subproblem and for both preconditioning strategies, we provide the optimized geometries as well as the time spent in the resolution of the normal equations, including the time spent in the construction of the preconditioner, see Fig. 8. The iterative solver is preconditioned by the sparse preconditioner (22) based on the truncated and sparse sensitivity matrix. The same results are obtained by making use of the limited memory Cholesky preconditioner (18). Both preconditioned iterative solvers are better than the LU based direct solver. However, the preconditioner based on the sparse approximation of the sensitivity matrix, obtained by setting the radius of the circular neighborhood two times larger than the density filter radius, enables a CPU time closer to the one involved in an equivalent global stress criterion, such as the p-norm of the Von-Mises, according to [8]. In these favorable cases, one can save two order of magnitudes with the preconditioned system and even four order of magnitudes for the sparse preconditioner.

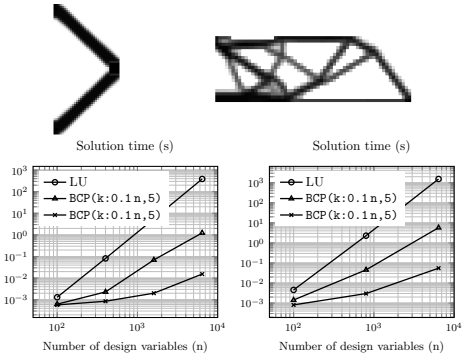

Figure 8: Top: The topology optimization problem submitted to stress constraints, (1), is considered for a two-bar truss as well as an MBB beam. The state-of-the-art topologies are recovered by solving the linearized KKT system, (10), of the MMA approximation (1), by means of a conjugate gradient solver preconditionned with (22). Similar results are obtained with the preconditioner (18). Bottom: The CPU-time spent in the solution of the linear system of the cantilever beam, left, as well as the MBB beam, right, is four order of magnitudes less than the one spent in the direct LU based solver.

C

8. Concluding remarks

When solving topology optimization problems using MMA approximation and primal-dual algorithms, one has to solve large scale linear systems of equations. Prohibitive computational time is observed because of the dense structure of the sensitivity matrix of the problem. First of all, we noticed that the positive definite linear systems of normal equations that arise throughout the iterations of primal-dual interior point solvers have a favorable spectral structure. We derived an efficient preconditioner for the system using a Cholesky like factorization of the Schur complement of the system. Then, we also explored a physical based approximation strategy to produce sparse approximations of the truncated sensitivity matrices of the restrictions with respect to local material densities. Thanks to the local nature of stress, one can ignore the components of sensitivity with respect to variables located outside of a local neighborhood. The combination of both algebraic and physical approximation accelerations technique showed up large improvements of computational effort spent in solving stress constrained topology optimization problems that are well known to be difficult to solve.

Our numerical experiments showed that we can reach a solution CPU time for each subproblem that is close to the effort involved in the FEM solution of the compliance type problem. Typically, one can expect a CPU time only of the same order of magnitude of the FEM analysis, which is about two order of magnitudes for the full matrix preconditioned and up to four order of magnitudes for specific problems and truncated sensitivity matrix.

In future work, we expect to extend the present results to problems with other local constraints, like slope constraints. It is also interesting to have a look at other physical engineering problems involving local constraints such as the design of electromagnetic systems where current densities are involved, or composite laminates optimization subjected to ply failure criteria.

Acknowledgments

This work was supported in part by the Walloon Region of Belgium under grant RW-1217703 (WBGreen FEDO) and the Belgian Science Policy under grant IAP P7/02. The authors would like to warmly thank Prof. Krister Svanberg for the fruitful discussions with the first author during his research stay at KTH and for providing his MATLAB code that was the starting point of this research.

References

[1] M. P. Bendsøe, N. Kikuchi, Generating optimal topologies in structural design using a homogenization method, Computer methods in applied mechanics and engineering 71 (2) (1988) 197–224.

[2] M. P. Bendsoe, Optimization of structural topology, shape, and material, Vol. 2, Springer, 1995.

[3] G. Rozvany, M. Bendsoe, U. Kirsch, Layout optimization of structures, Applied Mechanics Reviews 48 (2) (1995) 41–119.

[4] M. P. Bendsoe, O. Sigmund, Topology optimization: theory, methods, and applications, Springer Science & Business Media, 2003.

[5] H. A. Eschenauer, N. Olhoff, Topology optimization of continuum structures: a review, Applied Mechanics Reviews 54 (4) (2001) 331–390.

[6] G. I. Rozvany, A critical review of established methods of structural topology optimization, Structural and Multidisciplinary Optimization 37 (3) (2009) 217–237.

[7] P. Duysinx, M. P. Bendsøe, Topology optimization of continuum structures with local stress constraints, International journal for numerical methods in engineering 43 (8) (1998) 1453–1478.

[8] P. Duysinx, O. Sigmund, New developments in handling stress constraints in optimal material distribution, Proc of the 7th AIAA/USAF/NASAISSMO Symp on Multidisciplinary Analysis and Optimization 1 (1998) 1501–1509.

[9] K. Svanberg, M. Werme, Sequential integer programming methods for stress constrained topology optimization, Structural and Multidisciplinary Optimization 34 (4) (2007) 277–299.

[10] J. Petersson, O. Sigmund, Slope constrained topology optimization, International Journal for Numerical Methods in Engineering 41 (8) (1998) 1417–1434.

[11] E. Holmberg, B. Torstenfelt, A. Klarbring, Stress constrained topology optimization, Structural and Multidisciplinary Optimization 48 (1) (2013) 33–47.

[12] C. Le, J. Norato, T. Bruns, C. Ha, D. Tortorelli, Stress-based topology optimization for continua, Structural and Multidisciplinary Optimization 41 (4) (2010) 605–620.

[13] J. París, F. Navarrina, I. Colominas, M. Casteleiro, Block aggregation of stress constraints in topology optimization of structures, Advances in Engineering Software 41 (3) (2010) 433–441.

[14] M. Bruggi, P. Duysinx, Topology optimization for minimum weight with compliance and stress constraints, Structural and Multidisciplinary Optimization 46 (3) (2012) 369–384.

[15] M. Bruggi, P. Duysinx, A stress–based approach to the optimal design of structures with unilateral behavior of material or supports, Structural and Multidisciplinary Optimization 48 (2) (2013) 311–326.

[16] L. Schmidt, H. Miura, Approximation concepts for efficient structural synthesis, NASA Contractor Report 2552.

[17] C. Fleury, G. Sander, Dual methods for optimizing finite element flexural systems, Computer Methods in Applied Mechanics and Engineering 37 (3) (1983) 249–275.

[18] C. Fleury, L. A. Schmit Jr, Dual methods and approximation concepts in structural synthesis, NASA CR-3226.

[19] K. Svanberg, The method of moving asymptotes-a new method for structural optimization, International journal for numerical methods in engineering 24 (2) (1987) 359–373.

[20] C. Fleury, Conlin: an efficient dual optimizer based on convex approximation concepts, Structural Optimization 1 (2) (1989) 81–89.

[21] M. Wright, The interior-point revolution in optimization: history, recent developments, and lasting consequences, Bulletin of the American mathematical society 42 (1) (2005) 39–56.

[22] A. V. Fiacco, G. P. McCormick, Nonlinear programming: sequential unconstrained minimization techniques, Vol. 4, Siam, 1990.

C

[23] B. Maar, V. Schulz, Interior point multigrid methods for topology optimization, Structural and Multidisciplinary Optimization 19 (3) (2000) 214–224.

[24] C. Fleury, Structural optimization methods for large scale problems: status and limitations, in: ASME Paper No. DETC2007-34326, 2007.

[25] D. G. Luenberger, Introduction to linear and nonlinear programming, Vol. 28, Addison-Wesley Reading, MA, 1973.

[26] Y. Saad, Iterative methods for sparse linear systems, Siam, 2003.

[27] M. H. Wright, Ill-conditioning and computational error in interior methods for nonlinear programming, SIAM Journal on Optimization 9 (1) (1998) 84–111.

[28] M. Benzi, E. Haber, L. Taralli, Multilevel algorithms for large-scale interior point methods, SIAM Journal on Scientific Computing 31 (6) (2009) 4152–4175.

[29] L. Bergamaschi, J. Gondzio, M. Venturin, G. Zilli, Inexact constraint preconditioners for linear systems arising in interior point methods, Computational Optimization and Applications 36 (2) (2007) 137–147.

[30] A. Forsgren, P. E. Gill, J. D. Griffin, Iterative solution of augmented systems arising in interior methods, SIAM Journal on Optimization 18 (2) (2007) 666–690.

[31] J. Gondzio, Matrix-free interior point method, Computational Optimization and Applications 51 (2) (2012) 457–480.

[32] M. Ajiz, A. Jennings, A robust incomplete choleski-conjugate gradient algorithm, International Journal for Numerical Methods in Engineering 20 (5) (1984) 949–966.

[33] J. Cosgrove, J. Diaz, A. Griewank, Approximate inverse preconditionings for sparse linear systems, International journal of computer mathematics 44 (1-4) (1992) 91–110.

[34] K. Svanberg, A class of globally convergent optimization methods based on conservative convex separable approximations, SIAM Journal on Optimization (2002) 555–573.

[35] K. Svanberg, Mma and gcmma - two methods for nonlinear optimization, technical note.

[36] T. A. Davis, Direct methods for sparse linear systems, Vol. 2, Siam, 2006.

[37] R. Fletcher, Conjugate gradient methods for indefinite systems, Numerical analysis (1976) 73–89.

[38] M. F. Murphy, G. H. Golub, A. J. Wathen, A note on preconditioning for indefinite linear systems, SIAM Journal on Scientific Computing 21 (6) (2000) 1969–1972.

[39] A. Van der Sluis, Condition numbers and equilibration of matrices, Numerische Mathematik 14 (1) (1969) 14–23.

[40] F. Zhang, The Schur complement and its applications, Vol. 4, Numerical methods and algorithms, Springer, 2005.

Appendix

D

Paper IV: Combination of Shape and Topology Optimization based on the Lie Derivative

Combination of Shape and Topology Optimization based on the Lie Derivative

Erin Kuci[a,b], François Henrotte[b,c], Pierre Duysinx[a], Christophe Geuzaine[b]

[a] *University of Liège, Department of Aerospace and Mechanical Engineering, Belgium*
[b] *University of Liège, Department of Electrical Engineering and Computer Science, Belgium*
[c] *Université catholique de Louvain, EPL-iMMC-MEMA, Belgium*

Abstract

This paper presents a framework for the simultaneous application of shape and topology optimization in industrial design problems. Whereas the design variables of a shape optimization are the geometrical parameters of the CAD description, the design variables upon which density-based topology optimization acts represent the presence or absence of material at each point of the region where it is applied. These topology optimization design variables, which are called *densities*, are by essence substantial quantities. This means that they are attached to matter while, on the other hand, shape optimization implies ongoing changes of the model geometry. An appropriate combination of the two representations is therefore necessary to ensure a consistent design space as the joint shape-topology optimization process unfolds. The optimization problems dealt with in this paper are furthermore constrained to verify the governing partial differential equations (PDE) of a physical model, possibly nonlinear and discretized by means of, e.g., the finite element method (FEM). Theoretical formulae, based on the Lie derivative, to express the sensitivity of the performance functions of the optimization problem are derived and validated to be used in gradient-based algorithms. The method is applied to the torque ripple minimization in an interior permanent magnet synchronous machine (PMSM), with a limiting constraint on the weight of the optimal design.

Keywords: Lie derivative, Shape Optimization, Topology Optimization, Sensitivity Analysis, Simultaneous Shape and Topology, PMSM

Contents

Email address: Erin.Kuci@ulg.ac.be (Erin Kuci)

D

1. Introduction

Industrial design issues in structural engineering have been handled over the years by applying shape optimization or topology optimization separately, see for instance [1, 2, 3]. Shape optimization finds out the optimal layout within the design space determined by the geometrical parameters of the CAD description of the model. Density based topology optimization, on the other hand, optimally removes material in a structure, holding its strength between prescribed limits. Whereas the former seeks for an optimal layout within an *a priori* known and fixed design space, the latter is characterized by its ability to find optimal layouts with sometimes unusual contours and unexpected holes, but in general significantly lighter (in weight). There is therefore nowadays a desire to combine the two optimization methods in order to reach better performances.

Only little work about joint shape-topology optimization has been reported so far in the literature. In the context of packaging, for instance, the position [4] and shape [5] of the packaged items are determined by a shape optimization process while, at the same time, the protective material usage is minimized by means of a density-based topology optimization, [6, 7], so as to, e.g., minimize the overall volume of the package. An alternative approach with a fixed mesh is also possible. A Level Set representation of the component boundaries is used, instead of a CAD representation [8], and the model is solved with an extended finite element method (XFEM) [5]. However, the use of a Level Set representation of the geometry makes it difficult to take into account geometries with sharp angles (see for instance [9] or [10]). It limits hence the range of systems that can be optimized.

A combination of the respective design variables representations of shape and topology optimization is demonstrated in this paper. The solution of the joint optimization problem is then found by a sequential convex programming approach, [11, 12], called Method of the Moving Asymptotes (MMA) in which local approximations of the performance functions are built as convex and separable approximations (called subproblems). The MMA is a gradient based method. A substantial gain in computation time is obtained when sensitivities, i.e., the derivatives of the performance functions with respect to the design variables, are obtained analytically (prior to discretization) by differentiation under the integral sign instead of evaluating a finite difference, which requires one additional solution of the physical problem for each design variable. Analytical sensitivities have been used in the past for analysis based on XFEM, e.g. [5], but, as far as FEM-based analyses are concerned, a semi-analytic approach is used in general and it is reported for linear elasticity problems only. Still, we have shown in previous work that sensitivities in linear elastic and in electromagnetic problems can be derived in a unified fashion, in 2D or 3D with the velocity method [13], by means of an explicit Lie derivation of the FEM terms [14]. Building on the same methodology, analytical expressions are derived in this paper for the sensitivies of the topological density parameters. The proposed approach has been validated by comparison with the results published in [4] in case of classical structural optimization benchmarks, see Fig. 1.

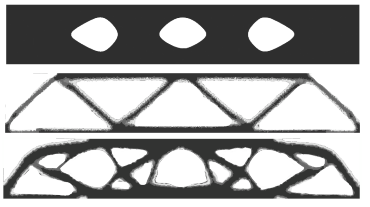

Figure 1: A successive shape optimization, top, of the holes represented by splines, and a density based topology optimization, middle, are performed separately to minimize the deflection of a MBB beam. In the bottom, the shape of the holes are determined by a shape optimization, while the support is simultaneously lighten by means of a topology optimization.

The paper is organized as follows. The general optimization problem is posed in Section 2 and the parameterization of the design space is discussed in Section 3. Section 4 deals with the theoretical definition of the sensitivities associated with the density variables and provide analytic formulae to evaluate them practically. In Sections 5, the joint shape-topology optimization is applied to the torque ripple minimization in an interior permanent magnet machine, with a limiting constraint on the weight of the optimal design.

2. Optimization in mixed shape and topology design spaces

Let us consider a bounded domain Ω undergoing both shape and topology modifications. The shape modifications are controlled by a set of geometrical design variables, noted $\boldsymbol{\tau}$, of the CAD model description. Topology optimization acts, on the other hand, on design variables which we call densities, noted $\boldsymbol{\rho}$. They represent the presence or not of a specific material at each point of model region where it is applied. Topology optimization offers a great flexibility in the design since it allows for an improvement of the material usage while shape optimization, on the other hand, allows for a fine tuning of the geometrical parameters.

A family of mappings,

$$p_{\boldsymbol{\delta\tau}} : \Omega(\boldsymbol{\tau}, \boldsymbol{\rho}) \subset E^3 \mapsto \Omega(\boldsymbol{\tau} + \boldsymbol{\delta\tau}, \boldsymbol{\rho}) \subset E^3, \tag{1}$$

describes the geometrical modification of Ω in the Euclidean space E^3, with no tearing nor overlapping, and it is parameterized by the set of geometrical design variables $\boldsymbol{\tau}$, see [15]. A variation $\boldsymbol{\delta\tau}$ of the shape variable brings the interfaces and the points of Ω from their current position to their modified position. A flow with a velocity field noted $\mathbf{v}$ is determined on E^3 by varying $\boldsymbol{\delta\tau}$ in the family of mappings (1) in a neighborhood of zero, see [14]. The parameter $\boldsymbol{\delta\tau}$ plays therefore the role of a pseudo time variable. The value of the density, on the other hand, at a given point in the model is obtained by evaluating that field at the coordinates of that point. However, the variation $\boldsymbol{\delta\rho}$ of the density field $\boldsymbol{\rho}$ does not involve any movement of the physical interfaces of Ω.

A physical problem is defined over Ω by a system of nonlinear PDEs expressed in terms of a state variable $\boldsymbol{z}$, the set $\boldsymbol{\tau}$ of shape design variables which bring modifications to Ω and the set $\boldsymbol{\rho}$ of density design variables which represent the material distribution over Ω. A weak formulation

of this problem is obtained by, e.g., a Galerkin linearization approach, and can be written in a generic form

$$r(\boldsymbol{\tau}, \boldsymbol{\rho}, \boldsymbol{z}^\star, \tilde{\boldsymbol{z}}) = 0, \ \forall \tilde{\boldsymbol{z}} \in Z_z^0, \tag{2}$$

with Z_z^0 an appropriate function space and $\boldsymbol{z}^\star$ the solution of the problem, and the functional $r(\boldsymbol{\tau}, \boldsymbol{\rho}, \boldsymbol{z}, \tilde{\boldsymbol{z}})$ called residual.

The design problem aims at determining simultaneously the geometrical design variables, $\boldsymbol{\tau}$, and the densities, $\boldsymbol{\rho}$, that minimize a cost function $f_0(\boldsymbol{\tau}, \boldsymbol{\rho}, \boldsymbol{z})$, subjected to m inequalities $f_j(\boldsymbol{\tau}, \boldsymbol{\rho}, \boldsymbol{z}) \leq 0$, $j = 1, \ldots, m$, ensuring the manufacturability or the feasibility of the design. The design space is also limited by side constraints either for the shape design variables, $\tau_i^{min} \leq \tau_i \leq \tau_i^{max}$, $i = 1, \ldots, n_\tau$, or the density design variables, $\rho_i^{min} \leq \rho_i \leq \rho_i^{max}$, $i = 1, \ldots, n_\rho$. The shape design variables are independent from the density design variables, but they are both involved in the performance functions. Hence, the optimization problem reads

$$\begin{aligned} \min_{\boldsymbol{\tau}, \boldsymbol{\rho}} \quad & f_0(\boldsymbol{\tau}, \boldsymbol{\rho}, \boldsymbol{z}^\star) \\ s.t. \quad & f_j(\boldsymbol{\tau}, \boldsymbol{\rho}, \boldsymbol{z}^\star) \leq 0, \ j = 1, \ldots, m \\ & \tau_i^{min} \leq \tau_i \leq \tau_i^{max}, \ i = 1, \ldots, n_\tau \\ & \rho_k^{min} \leq \rho_k \leq \rho_k^{max}, \ k = 1, \ldots, n_\rho \\ & r(\boldsymbol{\tau}, \boldsymbol{\rho}, \boldsymbol{z}^\star, \tilde{\boldsymbol{z}}) = 0, \ \forall \tilde{\boldsymbol{z}} \in Z_z^0. \end{aligned} \tag{3}$$

In this article, a sequential convex programming algorithm, e.g. MMA [16], is used, coupled with a finite element analysis code [17, 18] and makes use of the sensitivity matrix,

$$S_{ji} = \frac{\mathrm{d}f_j}{\mathrm{d}\tau_i}(\boldsymbol{\tau}, \boldsymbol{\rho}, \boldsymbol{z}^\star), \tag{4}$$

of the derivatives of the performance functions with respect to the shape design variables, and also

$$Q_{jk} = \frac{\mathrm{d}f_j}{\mathrm{d}\rho_k}(\boldsymbol{\tau}, \boldsymbol{\rho}, \boldsymbol{z}^\star), \tag{5}$$

the matrix of the derivatives of the performance functions with respect to the density design variables of problem (3), in order to reduce the number of function evaluations and hence, limit the required number of resolutions of the finite element physical problem (2).

3. Shape and topology design spaces

State-of-the-art methods of density-based topology optimization represent the material densities by a field defined on a fixed grid, identical to the FEM grid, [19], while shape optimization methods completely remesh the structure so as to preserve the quality of the FEM solution throughout the geometrical changes of the CAD model, see for instance [20].

In our approach, the densities are represented by a field defined on a fixed domain, noted $\Omega_{\boldsymbol{\rho}}$, not involved in the geometrical changes induced by the shape optimization, but covering in space all configurations allowed by it. The value of density at a point in the model is then simply the value of that field at the coordinates of the point. The modified CAD obtained by the variations of the shape design variables, are then discretized spatially by conformal meshes in order to carry out FEM analysis based on the material properties interpolated from the density field.

The shape design variables, $\boldsymbol{\tau}$, govern the CAD model description of the structure and their variation implies ongoing geometrical changes of the model, see Fig. 2. Each point $\boldsymbol{A}_{\boldsymbol{\tau}}$, resp.

$\boldsymbol{B}_{\boldsymbol{\tau}}$, is brought to a point $\boldsymbol{A}_{\boldsymbol{\tau}+\boldsymbol{\delta\tau}}$, resp. $\boldsymbol{B}_{\boldsymbol{\tau}+\boldsymbol{\delta\tau}}$, as the shape design variables are perturbed by $\boldsymbol{\delta\tau}$ and generates hence a velocity field, noted $\mathbf{v}$. The densities, noted $\boldsymbol{\rho}$, on the other hand, is represented by a discrete field defined on the fixed grid covering all configurations allowed by the variation of the geometrical design variable. The value of the density at a given point in the model, e.g. $\boldsymbol{A}_{\boldsymbol{\tau}}$ or $\boldsymbol{B}_{\boldsymbol{\tau}}$, is then obtained by evaluating that field at the coordinates, $\boldsymbol{x}_1, \boldsymbol{x}_2, \boldsymbol{x}_3$, of that point.

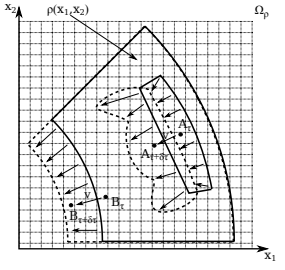

Figure 2: A 2D CAD model of a representative interior permanent magnet synchronous machine (PMSM) rotor is considered. The shape modifications are reflected by means of a velocity field, noted $\mathbf{v}$.

4. Sensitivity Analysis

We shall, for the sake of simplicity, consider one particular performance function, written explicitly in the form of an integral [1]

$$f(\tau, \rho, \boldsymbol{z}^\star) = \int_{\Omega(\tau)} F(\tau, \rho, \boldsymbol{z}^\star)\ \mathrm{d}\Omega, \tag{6}$$

one single shape design variable, noted τ, and one single density design variable, noted ρ, which amounts to dealing with one single entry of respectively the sensitivity matrix (4) and the sensitivity matrix (5). The treatment of any other entry would be identical.

Theoretical formulae to express the derivative of f with respect to a shape design variable, τ, at a continuous level, prior to discretization, have been demonstrated in detail using the Lie derivative, in both the direct and the adjoint approaches, see [14], in the context of the family of mappings (1), as introduced in [13].

Following the hybrid formalism introduced in [14], essentially based on vector analysis notations, analytical formulae of the derivative of f with respect to a density design variable, ρ, is provided here. In this framework, the derivative of f,

$$\frac{\mathrm{d}f}{\mathrm{d}\rho}(\tau, \boldsymbol{z}^\star) = \int_{\Omega(\tau)} \Big(D_\rho F(\tau, \rho, \boldsymbol{z}^\star) + \big\{ \mathrm{D}_{\boldsymbol{z}} F(\tau, \rho, \boldsymbol{z}^\star) \big\} \big(\frac{\mathrm{d}\boldsymbol{z}^\star}{\mathrm{d}\rho} \big) \Big)\ \mathrm{d}\Omega, \tag{7}$$

[1] If the performance function is a pointwise value, the expression of $F(\tau, \rho, \boldsymbol{z}^\star)$ will then involve a Dirac function.

has got two terms. The first term is the partial derivative of the functional,

$$D_\rho F(\tau,\rho,\boldsymbol{z}^\star) = \frac{\mathrm{d}F}{\mathrm{d}\rho}(\tau,\rho,\boldsymbol{z}^\star)\Big|_{\frac{\mathrm{d}\boldsymbol{z}}{\mathrm{d}\rho}=0} \tag{8}$$

defined as the derivative holding the field argument $\boldsymbol{z}$ constant, while the second term involves the Fréchet derivative of the functional $F(\tau,\rho,\boldsymbol{z})$ with respect to its field argument $\boldsymbol{z}$, defined by

$$\lim_{|\delta\boldsymbol{z}|\to 0}\frac{1}{|\delta\boldsymbol{z}|}\Big|F(\tau,\rho,\boldsymbol{z}+\delta\boldsymbol{z}) - F(\tau,\rho,\boldsymbol{z}) - \big\{\mathrm{D}_{\boldsymbol{z}}F(\tau,\rho,\boldsymbol{z})\big\}\big(\delta\boldsymbol{z}\big)\Big| = 0, \tag{9}$$

where the limit is taken over all sequences of non-zero $\delta\boldsymbol{z}$ that converge to zero. The Fréchet derivative is a linear operator applied to the argument in between parenthesis outside the curly braces, $\mathrm{d}\boldsymbol{z}/\mathrm{d}\rho$, and evaluated in arguments between parenthesis inside the curly braces. A simple total derivative is involved in (38) instead of the Lie derivative of the equivalent equation (11) of [14] obtained for a variable τ that modifies the geometry and therefore generates a non-null velocity field $\mathbf{v}$ of the flow of the mappings (1).

In a direct approach, a linear problem,

$$\int_{\Omega(\tau)}\Big(D_\rho R(\tau,\rho,\boldsymbol{z}^\star,\tilde{\boldsymbol{z}}) + \big\{\mathrm{D}_{\boldsymbol{z}}R(\tau,\rho,\boldsymbol{z}^\star,\tilde{\boldsymbol{z}})\big\}\big(\frac{\mathrm{d}\boldsymbol{z}^\star}{\mathrm{d}\rho}\big)\Big)\,\mathrm{d}\Omega = 0,\ \forall\tilde{\boldsymbol{z}}\in Z_z^0, \tag{10}$$

is solved for $\mathrm{d}\boldsymbol{z}^\star/\mathrm{d}\rho$, following the procedure to obtain (19) in [14], where the Lie derivative has been replaced, here, advantageously by a simple total derivative.

The adjoint approach can be applied as an alternative to the previous method that solves explicitly for $\mathrm{d}\boldsymbol{z}^\star/\mathrm{d}\rho$. An augmented Lagrangian function is defined,

$$\begin{aligned}\bar{f}(\tau,\rho,\boldsymbol{z},\boldsymbol{\lambda}) &= f(\tau,\rho,\boldsymbol{z}) - r(\tau,\rho,\boldsymbol{z},\boldsymbol{\lambda})\\ &= \int_{\Omega(\tau)}\Big(F(\tau,\rho,\boldsymbol{z}^\star) - R(\tau,\rho,\boldsymbol{z}^\star,\boldsymbol{\lambda})\Big)\,\mathrm{d}\Omega,\end{aligned} \tag{11}$$

with $\boldsymbol{\lambda}$ a Lagrange multiplier. As (2) implies that the residual $r(\tau,\rho,\boldsymbol{z}^\star,\lambda)$ is zero at equilibrium, one has

$$\bar{f}(\tau,\rho,\boldsymbol{z}^\star,\boldsymbol{\lambda}) = f(\tau,\rho,\boldsymbol{z}^\star), \tag{12}$$

and the sensitivity is expressed in terms of $\bar{f}$ by

$$\frac{\mathrm{d}f}{\mathrm{d}\rho}(\tau,\rho,\boldsymbol{z}^\star) = \frac{\mathrm{d}\bar{f}}{\mathrm{d}\rho}(\tau,\rho,\boldsymbol{z}^\star,\boldsymbol{\lambda}). \tag{13}$$

The so-called adjoint problem,

$$\int_{\Omega(\tau)}\Big(\big\{\mathrm{D}_{\boldsymbol{z}}F(\tau,\rho,\boldsymbol{z}^\star)\big\}\big(\frac{\mathrm{d}\boldsymbol{z}^\star}{\mathrm{d}\rho}\big) - \big\{\mathrm{D}_{\boldsymbol{z}}R(\tau,\rho,\boldsymbol{z}^\star,\boldsymbol{\lambda}^\star)\big\}\big(\frac{\mathrm{d}\boldsymbol{z}^\star}{\mathrm{d}\rho}\big)\Big)\,\mathrm{d}\Omega = 0, \tag{14}$$

is obtained here for $\lambda^\star$, again by following the procedure used to obtain (25) in [14], and the sensitivity is then given by

$$\frac{\mathrm{d}\bar{f}}{\mathrm{d}\rho}(\tau,\rho,\boldsymbol{z}^\star,\boldsymbol{\lambda}^\star) = \int_{\Omega(\tau)}\Big(D_\tau F(\tau,\rho,\boldsymbol{z}^\star) - D_\tau R(\tau,\rho,\boldsymbol{z}^\star,\boldsymbol{\lambda})\Big)\,\mathrm{d}\Omega, \tag{15}$$

in terms of the solutions of the nonlinear problem (2) and of the adjoint problem (14).

The material law $\boldsymbol{H}(\boldsymbol{B})$ can be written as,

$$\boldsymbol{H}(\boldsymbol{B}) = \eta(\rho)\boldsymbol{H}^1(\boldsymbol{B}), \quad \text{in } \Omega_\rho, \tag{16}$$

with $\boldsymbol{H}^1(\boldsymbol{B})$, the material law evaluated for $\rho = \rho^{max}$, i.e. the density of the fully solid structure.

For sake of comparison, the derivative of a material law, $\boldsymbol{H}(\boldsymbol{B})$, is treated as in [14]. First, the material law must be regarded as a relationship between the components of the fields

$$H_i(B_k) = \nu_{ij} B_j, \tag{17}$$

with ν_{ij} the components of the nonlinear reluctivity tensor of the material. Taking the derivative yields

$$\begin{aligned}\frac{\mathrm{d}H_i}{\mathrm{d}\rho}(B_k) &= \nu_{ij}\,\frac{\mathrm{d}B_j}{\mathrm{d}\rho} + \frac{\partial \nu_{ij}}{\partial B_k} B_j\,\frac{\mathrm{d}B_k}{\mathrm{d}\rho} + D_\tau H_i(B_k)\\ &= \nu^\partial_{ik}\,\frac{\mathrm{d}B_k}{\mathrm{d}\rho} + D_\tau H_i(B_k),\end{aligned}$$

with

$$\nu^\partial(B_k) = \nu^\partial_{ik}\,\boldsymbol{e}_i\boldsymbol{e}_k^T = \big(\nu_{ik} + \frac{\partial \nu_{ij}}{\partial B_k} B_j\big)\boldsymbol{e}_i\boldsymbol{e}_k^T \tag{18}$$

the components of the tangent reluctivity tensor of the material.

The partial derivative $D_\tau H_i(B_k)$ represents a variation of the magnetic field components H_i under a change of ρ, that would not be due to a variation of the field components B_k. This term accounts thus for an explicit dependency of the material law in the design variable ρ, independently of the field argument dependency, and reads,

$$D_\rho \boldsymbol{H}(\boldsymbol{B}) = \frac{\mathrm{d}\boldsymbol{H}}{\mathrm{d}\rho}(\boldsymbol{B})\Big|_{\frac{\mathrm{d}\boldsymbol{B}}{\mathrm{d}\rho}=0} = \frac{\mathrm{d}\eta}{\mathrm{d}\rho}\,\boldsymbol{H}^1(\boldsymbol{B}). \tag{19}$$

We can now write successively

$$\begin{aligned}\frac{\mathrm{d}H_i}{\mathrm{d}\rho}(B_k)\;\boldsymbol{e}_i &= \nu^\partial_{ik}\;\mathrm{d}B_k/\mathrm{d}\rho\;\boldsymbol{e}_i + D_\tau H_i(B_k)\;\boldsymbol{e}_i\\ &= \nu^\partial_{ij}\;\mathrm{d}B_k/\mathrm{d}\rho\;\boldsymbol{e}_i\boldsymbol{e}_j^T\,\boldsymbol{e}_k + D_\tau H_i(B_k)\;\boldsymbol{e}_i\\ &= \nu^\partial_{ij}\;\boldsymbol{e}_i\boldsymbol{e}_j^T\;\mathrm{d}B_k/\mathrm{d}\rho\;\boldsymbol{e}_k + D_\tau H_i(B_k)\;\boldsymbol{e}_i\\ &= \{\nu^\partial(B_k)\}(\mathrm{d}B_k/\mathrm{d}\rho\;\boldsymbol{e}_k) + D_\tau H_i(B_k)\;\boldsymbol{e}_i\end{aligned}$$

where $\boldsymbol{e}_j^T\boldsymbol{e}_k = \delta_{jk}$ has been used. At the last line, the tangent reluctivity tensor has been written as an operator acting on the vector (actually a 2-form) $\mathrm{d}B_k/\mathrm{d}\rho\;\boldsymbol{e}_k$.

The vectors $\mathrm{d}H_i/\mathrm{d}\rho(B_k)\;\boldsymbol{e}_i$ and $\mathrm{d}B_k/\mathrm{d}\rho\;\boldsymbol{e}_k$ can now be expressed in terms of $\mathrm{d}\boldsymbol{H}(\boldsymbol{B})/\mathrm{d}\rho$ and $\mathrm{d}\boldsymbol{B}/\mathrm{d}\rho$ to obtain

$$\frac{\mathrm{d}}{\mathrm{d}\rho}\boldsymbol{H}(\boldsymbol{B}) = \{\nu^\partial(\boldsymbol{B})\}\big(\frac{\mathrm{d}\boldsymbol{B}}{\mathrm{d}\rho}\big) + D_\rho \boldsymbol{H}(\boldsymbol{B}). \tag{20}$$

Similarly, one has for inverse material law $\boldsymbol{B}(\boldsymbol{H})$

$$\frac{\mathrm{d}\boldsymbol{B}(\boldsymbol{H})}{\mathrm{d}\rho} = \{\mu^\partial(H_k)\}\big(\frac{\mathrm{d}\boldsymbol{H}}{\mathrm{d}\rho}\boldsymbol{H}\big) + D_\rho \boldsymbol{B}(\boldsymbol{H}), \tag{21}$$

with $\mu^\partial = (\nu^\partial)^{-1}$.

5. Application to the design of a PMSM

5.1. Magnetostatics modeling

A 3-phase interior permanent magnet synchronous machine (PMSM) fed by a sinusoidal current is considered, see Fig 3. We describe the geometry of the PMSM by a two dimensional CAD model. The PMSM is excited by the current density $\boldsymbol{J}$ in a region $\Omega_S = \Omega_A \cup \Omega_B \cup \Omega_C \subset \Omega$ and by permanent magnets with a magnetization $\boldsymbol{M}$ on a region $\Omega_M \subset \Omega$. In a two-dimensional setting, the magnetic vector potential $\boldsymbol{A} = A_z \boldsymbol{e}_z$ formulation of Magnetostatics models the magnetic behavior of the electrical machine and reads,

$$\mathbf{curl}\, \boldsymbol{H}(\boldsymbol{B}) = \boldsymbol{J} + \mathbf{curl}\, \boldsymbol{M} \qquad \text{in } \Omega \tag{22}$$

$$\boldsymbol{H}(\boldsymbol{B}) = \nu \boldsymbol{B} \qquad \text{in } \Omega. \tag{23}$$

In (23), the reluctivity characteristic ν is a scalar, and it can be a function of $\boldsymbol{B} = \mathbf{curl}\, \boldsymbol{A}$ (nonlinear material), which can be written by a SIMP law, in the region Ω_ρ, set as the rotor iron parts, which undergoes topology optimization,

$$\nu = \nu_0 + \rho^p(\nu_1(\boldsymbol{B}) - \nu_0), \quad \text{in } \Omega_\rho \tag{24}$$

with ν_1 being the reluctivity of iron and ν_0 the reluctivity of air.

A homogenous Dirichlet boundary condition

$$\mathbf{A}|_{\Gamma_{3_r}} = \mathbf{A}|_{\Gamma_{3_s}} = 0 \tag{25}$$

is applied, which supposes that there is no magnetic flux density outside the domain. In addition, considering the electromagnetic symmetries and anti-periodic boundary conditions,

$$\begin{aligned} \mathbf{A}|_{\Gamma_{1_r}} &= -\mathbf{A}|_{\Gamma_{2_r}}, \\ \mathbf{A}|_{\Gamma_{1_s}} &= -\mathbf{A}|_{\Gamma_{2_s}}, \end{aligned} \tag{26}$$

the domain used for the study and the optimization consists of $1/8$ of the original structure.

Considering a standard three-phase winding, Ω_A, Ω_B and Ω_C, distributed along the stator slots, $\Delta\theta$ is the angle describing the angular position of the rotor

$$p_A = \Delta\theta \cdot n_p$$

and assuming an electrical displacement equal to $2\pi/3$ radians between each phase, the current density reads

$$\boldsymbol{J} = I_s \frac{n_w}{S_c} \cos(p_A)\, \boldsymbol{e}_z, \qquad \text{in Phase } \Omega_A \tag{27}$$

$$\boldsymbol{J} = I_s \frac{n_w}{S_c} \cos(p_A - \frac{2\pi}{3})\, \boldsymbol{e}_z, \qquad \text{in Phase } \Omega_B \tag{28}$$

$$\boldsymbol{J} = I_s \frac{n_w}{S_c} \cos(p_A - \frac{4\pi}{3})\, \boldsymbol{e}_z, \qquad \text{in Phase } \Omega_C$$

with n_w, the number of wires per slot in the stator, S_c, the surface of the coil, and I_s the maximum current. Each phase is therefore supplied by current-controlled voltage source inverter, which is however not modeled here for the sake of simplicity. The phase coils of such a winding are fed by sine wave currents synchronous with the corresponding flux linkages due to the PM flux.

Moreover, the spatial discretization of the rotor and the stator remain unchanged as the rotor changes positions, and are connected by a single layer of elements in the moving band which is remeshed for each rotor position [21].

The weak formulation of the problem reads [22]: find $\boldsymbol{A}^\star$ in an appropriate function space Z_A verifying (25) and (26) at a given rotor position θ_R, such that

$$r(\tau, \rho, \boldsymbol{A}^\star, \bar{\boldsymbol{A}}) \equiv \int_\Omega \Big(\boldsymbol{H}(\boldsymbol{B}^\star) \cdot \bar{\boldsymbol{B}} - \boldsymbol{J} \cdot \bar{\boldsymbol{A}} - \boldsymbol{M} \cdot \bar{\boldsymbol{B}} \Big) \, \mathrm{d}\Omega = 0, \quad \forall \bar{\boldsymbol{A}} \in Z_A, \tag{29}$$

with $\boldsymbol{B}^\star = \mathbf{curl}\, \boldsymbol{A}^\star$ and $\bar{\boldsymbol{B}} = \mathbf{curl}\, \bar{\boldsymbol{A}}$.

A method based on Maxwell's stress tensor is used for the computation of torque. Choosing a circular shell of axial length L_a and surface S_a in the airgap of the machine as a closed integration surface that surrounds the rotor, the torque at a given rotor position $\theta_R = \theta_l$ reads,

$$T_l = \int_{\Omega_{mb}} \nu_0 \; t_g \; B_r \; B_\theta \; \mathrm{d}\Omega, \tag{30}$$

with

$$t_g = 2\pi \frac{L_a}{S_a} \boldsymbol{r} \cdot \boldsymbol{r} \tag{31}$$

being a geometrical coefficient where $\boldsymbol{r}$ is radial vector, $B_r = \boldsymbol{B} \cdot \boldsymbol{e}_r$ and $B_\theta = \boldsymbol{B} \cdot \boldsymbol{e}_\theta$ are the scalar product of $\boldsymbol{B}$ with respectively the radial basis vector $\boldsymbol{e}_r$ and tangential basis vector $\boldsymbol{e}_\theta$.

5.2. Optimization problem

Interior permanent magnets synchronous machines exhibit magnetic saturations which occur in iron parts and hence suffer from a high level of torque ripple which should be reduced as much as possible, while keeping the average torque above or equal to the nominal torque of the machine. Let us perform a combined shape and topology optimization to determine simultaneously (1) the distance of the PMs from the air gap, the angle between the PMs, both set as shape design variables, and also (2) the iron fraction field which represents the density distribution in the rest of the rotor. We want to smoothen the torque with respect to the movement of the rotor, minimizing hence the torque ripple, while preserving an average torque to match the nominal torque of the machine. In addition, we considered a resource constraint defined as a given volume fraction of the available domain. The combined shape and topology optimization problem reads,

$$\begin{aligned}
\min_{\boldsymbol{\tau}, \boldsymbol{\rho}} \quad & f_0(\boldsymbol{\tau}, \boldsymbol{\rho}, \boldsymbol{A}^\star) \equiv \sum_{l=1}^{N_p} \big(T_l - T_{nom} \big)^2 \\
s.t. \quad & f_1(\boldsymbol{\tau}, \boldsymbol{\rho}, \boldsymbol{A}^\star) \equiv \frac{1}{N_p} \sum_{l=1}^{N_p} T_l - T_{nom} \leq 0, \\
& f_2(\boldsymbol{\tau}, \boldsymbol{\rho}, \boldsymbol{A}^\star) \equiv \int_{\Omega_\rho} \rho \; \mathrm{d}\Omega - \alpha \int_{\Omega_\rho} \mathrm{d}\Omega \leq 0, \\
& \tau_i^{min} \leq \tau_i \leq \tau_i^{max}, \; i = 1, \ldots, n_\tau \\
& \rho_k^{min} \leq \rho_k \leq \rho_k^{max}, \; k = 1, \ldots, n_\rho \\
& r(\boldsymbol{\tau}, \boldsymbol{\rho}, \boldsymbol{A}^\star, \bar{\boldsymbol{A}}) = 0, \; \forall \bar{\boldsymbol{z}} \in Z_A^0.
\end{aligned} \tag{32}$$

The design space is limited by physical or technological side constraints either for the shape design variables, $\tau_i^{min} \leq \tau_i \leq \tau_i^{max}$, $i = 1, \ldots, n_\tau$, or the density design variables, $\rho_i^{min} \leq \rho_i \leq$

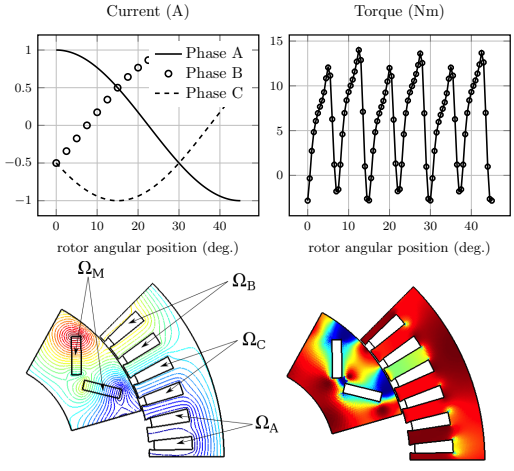

Figure 3: A 3-phase interior permanent magnet (IPM) machine fed by a sinusoidal current, top left, and modeled by a nonlinear magnetostatic problem in terms of the vector potential $\boldsymbol{A}$ is considered. The vector potential, isovalues shown in bottom left, obtained by solving the nonlinear magnetostatic problem at a given rotor position is used to evaluate the magnetic permeability map, bottom right, of the machine. A magnetic saturation (blue) occurs in many regions of the iron parts where the induction flux is high.

ρ_i^{max}, $i = 1, \ldots, n_\rho$, which are independent from the shape design variables, but involved in the same performance functions.

The evaluation of the performance functions f_0 and f_j, $j = 1, 2$ for a given geometry configuration, $\boldsymbol{\tau}$, and a given material distribution, $\boldsymbol{\rho}$, requires the knowledge of $\boldsymbol{A}^\star$ for that particular value of $\boldsymbol{\tau}$ and $\boldsymbol{\rho}$, which implies solving anew the nonlinear physical problem (29) at N_p rotor positions and evaluate the torque T_l at each position θ_l, by making use of (30). The repetition of these evaluations is time-consuming for large scale applications.

5.3. Problem sensitivity analysis

The variation of a shape design variable, such as τ, brings a flow of continuous shape modification of the geometrical model, with a velocity field noted $\mathbf{v}$, and was taken into account using the Lie derivative, [14].

In that context, the derivative of the residual (29) at equilibrium with respect to a shape design variable τ requires the Lie derivative to describe the differentiation of the integral quantity

over a deforming domain, and is obtained by applying the chain rule of derivatives,

$$\begin{aligned}\frac{\mathrm{d}}{\mathrm{d}\tau}r(\tau,\boldsymbol{A}^\star,\bar{\boldsymbol{A}}) &= \int_\Omega \Big(L_{\mathbf{v}}\boldsymbol{H}(\boldsymbol{B}^\star)\cdot\bar{\boldsymbol{B}} + \boldsymbol{H}(\boldsymbol{B}^\star)\cdot L_{\mathbf{v}}\bar{\boldsymbol{B}} \\ &\quad - L_{\mathbf{v}}\boldsymbol{J}\cdot\bar{\boldsymbol{A}} - \boldsymbol{J}\cdot L_{\mathbf{v}}\bar{\boldsymbol{A}} - L_{\mathbf{v}}\boldsymbol{M}\cdot\bar{\boldsymbol{B}} - \boldsymbol{M}\cdot L_{\mathbf{v}}\bar{\boldsymbol{B}}\Big)\,\mathrm{d}\Omega \\ &= \int_\Omega \Big(L_{\mathbf{v}}\boldsymbol{H}(\boldsymbol{B}^\star)\cdot\bar{\boldsymbol{B}} - L_{\mathbf{v}}\boldsymbol{J}\cdot\bar{\boldsymbol{A}} - L_{\mathbf{v}}\boldsymbol{M}\cdot\bar{\boldsymbol{B}}\Big)\,\mathrm{d}\Omega = 0,\end{aligned} \tag{33}$$

since the fact that $\boldsymbol{B}^\star$ is the solution of (29) implies

$$\int_\Omega \Big(H(\boldsymbol{B}^\star)\cdot L_{\mathbf{v}}\bar{\boldsymbol{B}} - \boldsymbol{J}\cdot L_{\mathbf{v}}\bar{\boldsymbol{A}} - \boldsymbol{M}\cdot L_{\mathbf{v}}\bar{\boldsymbol{B}}\Big)\,\mathrm{d}\Omega = 0,$$

since $L_{\mathbf{v}}\bar{\boldsymbol{A}} \in Z_A^0$.

The magnetization $\boldsymbol{M}$ is a 1-form. Similarly to the current density, its Lie derivative depends on how the magnetization is imposed in the model. If the magnetization M flowing in a conducting region Ω_M of the model is fixed, one has

$$\frac{\mathrm{d}M}{\mathrm{d}\tau} = 0 = \int_{\Omega_M} L_{\mathbf{v}}\boldsymbol{M}\,\mathrm{d}\Omega, \tag{34}$$

and the term $L_{\mathbf{v}}\boldsymbol{M}$ then simply vanishes. If on the other hand the magnetization density is constant, which is the case in our application example, one has $L_{\mathbf{v}}M_i = 0$ and by Eq. (38) of [14]

$$L_{\mathbf{v}}\boldsymbol{M} = (\nabla\mathbf{v})\boldsymbol{M}. \tag{35}$$

Substituting Eqs. (53) and (55) from [14] and also (35) into (33) yields the linear system to solve for $L_{\mathbf{v}}\boldsymbol{A}^\star$,

$$\begin{aligned}&\int_\Omega \nu^\partial\, L_{\mathbf{v}}\boldsymbol{B}^\star\cdot\bar{\boldsymbol{B}}\,\mathrm{d}\Omega + \Big[\int_\Omega \Big(\nu^\partial\big((\nabla\mathbf{v})^{\mathbf{T}}\boldsymbol{B}^\star - \boldsymbol{B}^\star\,\mathrm{div}\,\mathbf{v}\big)\cdot\bar{\boldsymbol{B}} \\ &\quad + (\nabla\mathbf{v})\,\nu\boldsymbol{B}^\star\cdot\bar{\boldsymbol{B}} - (\boldsymbol{J}\,\mathrm{div}\,\mathbf{v} - (\nabla\mathbf{v})^{\mathbf{T}}\boldsymbol{J})\cdot\bar{\boldsymbol{A}} - (\nabla\mathbf{v})\boldsymbol{M}\cdot\bar{\boldsymbol{B}}\Big)\,\mathrm{d}\boldsymbol{\Omega}\Big] = \mathbf{0},\ \forall\bar{\boldsymbol{A}}\in\mathbf{Z_A^0}.\end{aligned} \tag{36}$$

The first term in (36) involves the tangent stiffness matrix at a given rotor position, which is already known from the computation of $\boldsymbol{A}^\star$, and the bracketed terms make up the partial derivative term $\int_\Omega D_\tau R\,\mathrm{d}\Omega$ of Eq. (19) of [14].

A variation of the material distribution, ρ, on the other hand, does not involve any explicit interface modification, and hence has a zero velocity field, which greatly simplifies the analytical expression of sensitivity, by making use of only classical total derivative instead of the Lie derivative. The direct expression of sensitivity (36) reads, now,

$$\int_\Omega \nu^\partial \frac{\mathrm{d}\boldsymbol{B}^\star}{\mathrm{d}\rho}\cdot\bar{\boldsymbol{B}}\,\mathrm{d}\Omega + \Big[\int_\Omega D_\rho H(\boldsymbol{B}^\star)\cdot\bar{\boldsymbol{B}}\,\mathrm{d}\Omega\Big] = 0,\ \forall\bar{\boldsymbol{A}}\in Z_A^0, \tag{37}$$

where there is no dependency of $\boldsymbol{J}$ and $\boldsymbol{M}$ in ρ. In (37), the first term involves the partial derivative of $\boldsymbol{H}(\boldsymbol{B})$,

$$\begin{aligned}D_\rho\boldsymbol{H}(\boldsymbol{B}^\star) &= \frac{\mathrm{d}\boldsymbol{H}}{\mathrm{d}\rho}(\boldsymbol{B}^\star)\Big|_{\frac{\mathrm{d}\boldsymbol{B}}{\mathrm{d}\rho}=0} \\ &= p\ \rho^{(p-1)}(\nu^1(\boldsymbol{B}) - \nu_0)\boldsymbol{B}\end{aligned} \tag{38}$$

defined as the derivative holding the field argument $\boldsymbol{B}$ constant obtained by differentiating (24).

5.4. Numerical example

In this article, a sequential convex programming algorithm, MMA [16], is used, coupled with a finite element analysis code [17, 18] and makes use of the sensitivity matrix derived so far. The results of the optimization problem are summarized in Fig. 4. The entire analysis domain and design domain are discretized using 37,521 nodes and 64,640 triangular elements. The densities are used to interpolate the magnetic reluctivity through a classical SIMP (24) with a penalization parameter p fixed to 3. The optimization process results, after roughly 250 iterations, in PMs with a slightly increased angular openings compared to the original design, indicating that the topology optimization allows, in this particular case, major improvements of the electrical rotating machine. The torque ripple is reduced by 97% while the average torque is set to the nominal torque of the machine.

A post-processing stage is needed to obtain a manufacturable design, see for instance [23] or more recently [24]. Computer vision technologies to represent the boundary of the void-solid finite element topology optimization result have first been performed in [25]. A density contour approach has also been used in [26], or [27] as well as a geometric reconstruction approach, see for instance [28].

Here we performed a spline-based interpolation of the density isovalues. This then leads to a CAD model which is used for latter design stages as well as e.g. for additive manufacturing purposes, see Fig. 5. However, a drawback inherent to such procedures, is that post-processed results are no longer optimal and may also not comply with the given design criteria, thus slightly deteriorating the topology optimization solutions. In this particular case, the torque ripple is increased by 10% from the one computed with the density field.

6. Conclusion and perspectives

We have developed a unified tool for handling simultaneously the complex interactions between the material distribution model of topology optimization and the geometrical modifications which occur throughout a shape optimization. Following the general framework of sensitivity analysis derived so far, shape sensitivity is computed efficiently. We can obtain simultaneously the sensitivity with respect to shape and density design variables. The theoretical results gathered in the thesis have been implemented within ONELAB and have been successfully applied to electro-mechanical optimization of the shape and topology of energy conversion systems which are of a great importance in industry. The design of an electrical synchronous rotating machine with interior permanent magnets, modeled by means of a two-dimensional CAD model coupled to a nonlinear magnetostatic formulation, and aiming to minimize the torque ripple has been successfully obtained in our framework.

Acknowledgments

This work was supported in part by the Walloon Region of Belgium under grant RW-1217703 (WBGreen FEDO) and the Belgian Science Policy under grant IAP P7/02.

References

[1] G. Rozvany, Aims, scope, methods, history and unified terminology of computer-aided topology optimization in structural mechanics, Structural and Multidisciplinary optimization 21 (2) (2001) 90–108.

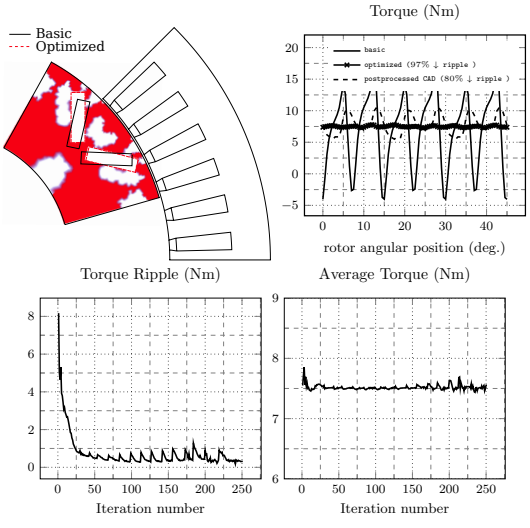

Figure 4: A range of $N_p = 16$ rotor angular positions which covers an angular torque period, from 0 to 16 degrees has been considered and the geometrical configuration of the PMs as well as the iron distribution in the rotor, with a volume fraction of 70%, have been determined simultaneously with an combined shape and topology optimization.

[2] H. A. Eschenauer, N. Olhoff, Topology optimization of continuum structures: a review, Applied Mechanics Reviews 54 (4) (2001) 331–390.

[3] O. Sigmund, K. Maute, Topology optimization approaches, Structural and Multidisciplinary Optimization 48 (6) (2013) 1031–1055.

[4] J. Zhu, W. Zhang, P. Beckers, Integrated layout design of multi-component system, International journal for numerical methods in engineering 78 (6) (2009) 631–651.

[5] J. Zhang, W. Zhang, J. Zhu, L. Xia, Integrated layout design of multi-component systems using xfem and analytical sensitivity analysis, Computer Methods in Applied Mechanics and Engineering 245 (2012) 75–89.

[6] Z. Qian, G. Ananthasuresh, Optimal embedding of rigid objects in the topology design of structures, Mechanics Based Design of Structures and Machines 32 (2) (2004) 165–193.

[7] W. Zhang, L. Xia, J. Zhu, Q. Zhang, Some recent advances in the integrated layout design of multicomponent systems, Journal of Mechanical Design 133 (10) (2011) 104503.

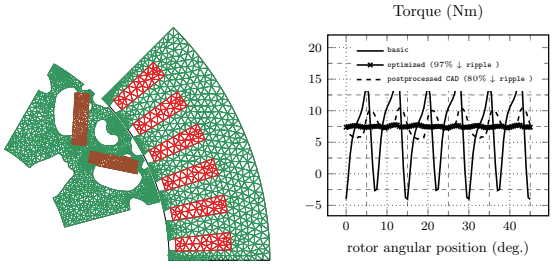

Figure 5: A smooth CAD model of the optimized rotor is obtained manually from the finite element representation of Fig. 4 by making use of spline curves. The geometrical model can hence be used in later design stages.

[8] S. Osher, J. A. Sethian, Fronts propagating with curvature-dependent speed: algorithms based on hamilton-jacobi formulations, Journal of computational physics 79 (1) (1988) 12–49.

[9] H. A. Kalameh, O. Pierard, C. Friebel, E. Béchet, Semi-implicit representation of sharp features with level sets, Finite Elements in Analysis and Design 117 (2016) 31–45.

[10] F. Duboeuf, E. Béchet, Embedded solids of any dimension in the x-fem. part ibuilding a dedicated p1 function space, Finite Elements in Analysis and Design 130 (2017) 80–101.

[11] C. Fleury, L. A. Schmit Jr, Dual methods and approximation concepts in structural synthesis, NASA (1980) CR–3226.

[12] K. Svanberg, The method of moving asymptotes- a new method for structural optimization, International journal for numerical methods in engineering 24 (2) (1987) 359–373.

[13] J. Sokolowski, J.-P. Zolesio, Introduction to shape optimization, in: Introduction to Shape Optimization, Springer, 1992, pp. 5–12.

[14] E. Kuci, F. Henrotte, P. Duysinx, C. Geuzaine, Design sensitivity analysis for shape optimization based on the Lie derivative, Computer Methods in Applied Mechanics and Engineering 317 (2017) 702 – 722.

[15] J. Sokolowski, J.-P. Zolesio, Introduction to shape optimization 16 (1992) 5–12. doi:10.1007/978-3-642-58106-9_1.
URL http://dx.doi.org/10.1007/978-3-642-58106-9_1

[16] K. Svanberg, A class of globally convergent optimization methods based on conservative convex separable approximations, SIAM Journal on Optimization (2002) 555–573.

[17] C. Geuzaine, J.-F. Remacle, Gmsh: A 3-D finite element mesh generator with built-in pre- and post-processing facilities, International Journal for Numerical Methods in Engineering 79 (11) (2009) 1309–1331.

[18] P. Dular, C. Geuzaine, A. Genon, W. Legros, An evolutive software environment for teaching finite element methods in electromagnetism, IEEE Transactions on Magnetics 35 (3) (1999) 1682–1685.

[19] M. P. Bendsøe, N. Kikuchi, Generating optimal topologies in structural design using a homogenization method, Computer methods in applied mechanics and engineering 71 (2) (1988) 197–224.

[20] W.-H. Zhang, P. Beckers, C. Fleury, A unified parametric design approach to structural shape optimization, International Journal for Numerical Methods in Engineering 38 (13) (1995) 2283–2292.

[21] N. Sadowski, Y. Lefevre, M. Lajoie-Mazenc, J. Cros, Finite element torque calculation in electrical machines while considering the movement, Magnetics, IEEE Transactions on 28 (2) (1992) 1410–1413. doi:10.1109/20.123957.

[22] A. Bossavit, Computational electromagnetism: variational formulations, complementarity, edge elements, Academic Press, 1998.

[23] M.-H. Hsu, Y.-L. Hsu, Interpreting three-dimensional structural topology optimization results, Computers & structures 83 (4-5) (2005) 327–337.

[24] T. Zegard, G. H. Paulino, Bridging topology optimization and additive manufacturing, Structural and Multidisciplinary Optimization 53 (1) (2016) 175–192.

[25] M. P. Bendsøe, H. C. Rodrigues, Integrated topology and boundary shape optimization of 2-d solids, Computer Methods in Applied Mechanics and Engineering 87 (1) (1991) 15–34.

[26] A. Kumar, D. Gossard, Synthesis of optimal shape and topology of structures, Journal of Mechanical Design 118 (1) (1996) 68–74.

[27] Y.-L. Hsu, M.-S. Hsu, C.-T. Chen, Interpreting results from topology optimization using density contours, Computers & Structures 79 (10) (2001) 1049–1058.

[28] P.-S. Tang, K.-H. Chang, Integration of topology and shape optimization for design of structural components, Structural and Multidisciplinary Optimization 22 (1) (2001) 65–82.

SHAPE AND TOPOLOGY OPTIMIZATION FOR ELECTRO-MECHANICAL ENERGY CONVERTERS

Erin Kuci

The sustained growth of the industrial sector requires high-efficiency electro-mechanical energy converters, in particular electrical rotating machines, at the lowest possible cost. The use of modern power electronics converters at all levels of electrical power applications, involves, on the other hand, switching components with very low switching times and always increasing current levels. Passive components in these devices (busbars, inductors, transformers) must be designed to be compact without compromising their performance (e.g. power losses, electromagnetic interference/compatibility). Automated design optimization methods, in particular shape and topology optimization, used so far mostly in the field of structural engineering, offer a major step evolution in the design of such electro-mechanical and electric energy converters.The objective of this thesis is to provide engineers and practitioners of the field with appropriate methods which allow to carry out such design tasks by numerical optimization in an efficient way, and to extend the design capabilities to electro-mechanical converters.

This thesis exploits a computer aided design representation of industrial systems and the finite element method to solve the partial differential equations (PDEs) that govern their behavior under certain physical conditions. This thesis addresses three main subjects. First, the sensitivity analysis of electromagnetic PDEs solution is revisited in view of being used with gradient-based methods. Classical scalar formulations are extended to a general rigorous framework, and expressed analytically prior to discretization, to treat the vector case. Secondly, an iterative solver is designed so as to solve efficiently the large-scale linear systems arising from the design problem. Third, the design improvement capabilities are extended by developing an integrated and unified formalism for simultaneous shape and topology optimization of a system.